



University of Kentucky
UKnowledge

University of Kentucky Doctoral Dissertations

Graduate School

2010

Real-time 3-D Reconstruction by Means of Structured Light Illumination

Kai Liu

University of Kentucky, kai.liu@uky.edu

[Right click to open a feedback form in a new tab to let us know how this document benefits you.](#)

Recommended Citation

Liu, Kai, "Real-time 3-D Reconstruction by Means of Structured Light Illumination" (2010). *University of Kentucky Doctoral Dissertations*. 81.

https://uknowledge.uky.edu/gradschool_diss/81

This Dissertation is brought to you for free and open access by the Graduate School at UKnowledge. It has been accepted for inclusion in University of Kentucky Doctoral Dissertations by an authorized administrator of UKnowledge. For more information, please contact UKnowledge@lsv.uky.edu.

ABSTRACT OF DISSERTATION

Kai Liu

The Graduate School
University of Kentucky
2010

Real-time 3-D Reconstruction by Means of Structured Light Illumination

ABSTRACT OF DISSERTATION

A dissertation submitted in partial fulfillment of the requirements for the degree of Doctor of Philosophy in the College of Engineering at the University of Kentucky

By
Kai Liu
Lexington, Kentucky

Director: Dr. Daniel L. Lau, Associate Professor of Electrical and Computer Engineering
Lexington, Kentucky 2010

Copyright© Kai Liu 2010

ABSTRACT OF DISSERTATION

Real-time 3-D Reconstruction by Means of Structured Light Illumination

Structured light illumination (SLI) is the process of projecting a series of light striped patterns such that, when viewed at an angle, a digital camera can reconstruct a 3-D model of a target object's surface. But by relying on a series of time multiplexed patterns, SLI is not typically associated with video applications. For this purpose of acquiring 3-D video, a common SLI technique is to drive the projector/camera pair at very high frame rates such that any object's motion is small over the pattern set. But at these high frame rates, the speed at which the incoming video can be processed becomes an issue. So much so that many video-based SLI systems record camera frames to memory and then apply off-line processing. In order to overcome this processing bottleneck and produce 3-D point clouds in real-time, we present a lookup-table (LUT) based solution that in our experiments, using a 640 by 480 video stream, can generate intermediate phase data at 1063.8 frames per second and full 3-D coordinate point clouds at 228.3 frames per second. These achievements are 25 and 10 times faster than previously reported studies. At the same time, a novel dual-frequency pattern is developed which combines a high-frequency sinusoid component with a unit-frequency sinusoid component, where the high-frequency component is used to generate robust phase information and the unit-frequency component is used to reduce phase unwrapping ambiguities. Finally, we developed a gamma model for SLI, which can correct the non-linear distortion caused by the optical devices. For three-step phase measuring profilometry (PMP), analysis of the root mean squared error of the corrected phase showed a $60\times$ reduction in phase error when the gamma calibration is performed versus $33\times$ reduction without calibration.

KEYWORDS: Real-time 3-D Reconstruction, Structured Light Illumination, Phase Measuring Profilometry, Gamma Correction, Phase Channel Multiplexing Pattern.

Author's signature: _____ Kai Liu

Date: _____ July 26, 2010

Real-time 3-D Reconstruction by Means of Structured Light Illumination

By
Kai Liu

Director of Dissertation: Daniel L. Lau

Director of Graduate Studies: Stephen D. Gedney

Date: July 26, 2010

DISSERTATION

Kai Liu

The Graduate School
University of Kentucky
2010

Real-time 3-D Reconstruction by Means of Structured Light Illumination

DISSERTATION

A dissertation submitted in partial
fulfillment of the requirements for
the degree of Doctor of Philosophy
in the College of Engineering at the
University of Kentucky

By
Kai Liu
Lexington, Kentucky

Director: Dr. Daniel L. Lau, Associate Professor of Electrical and Computer
Engineering
Lexington, Kentucky 2010

Copyright© Kai Liu 2010

Dedicated to my family.

ACKNOWLEDGMENTS

I would like to thank all those people who have helped me for this dissertation.

First, I must thank my advisor, Dr. Daniel L. Lau for giving me an opportunity to work on this project and lead me into this area. Also Dr. Lau taught me so much from the whole idea to the technique details. It is his persistence for perfection and interest in little details that have supplemented my own quest for knowledge. I must also extend my great thanks to Dr. Laurence G. Hassebrook for his constant encouragement and support during all the time. Whenever I meet problems, Dr. Lau and Dr. Hassebrook always help and inspire me.

Second, thank Dr. Qi Hao and Yongchang Wang who have worked together with me through all the problems. Discussions with them regarding the work, were always interesting and intellectual.

Finally, this work would not have been possible without the support and love of my parents and my older sister. They were the ones who always encouraged and motivated me to go ahead. I also thank all my friends for always putting a smile on my face during tough times and support me.

TABLE OF CONTENTS

Acknowledgments	iii
Table of Contents	iv
List of Figures	v
List of Tables	xi
Chapter 1 Introduction	1
1.1 Structured light illumination	3
1.2 Pattern Robustness	20
1.3 Contributions of this Dissertation	48
1.4 Summation	55
Chapter 2 Real-time 3-D Reconstruction	57
2.1 LUT-based processing	57
2.2 Experiments	68
Chapter 3 Phase Channel Multiplexing Pattern Strategy	75
3.1 Parameters and noise analysis for PMP	76
3.2 Phase channel multiplexing pattern strategy	86
3.3 Experiments	103
Chapter 4 Gamma Model and Its Analysis for Phase Measuring Profilometry	114
4.1 Gamma model for PMP	114
4.2 Phase correction with gamma calibration	126
4.3 Phase correction without gamma calibration	129
4.4 Phase correction with phase matching	132
4.5 Experiment	133
Chapter 5 Conclusion	144
5.1 Real-Time SLI	145
5.2 Pattern Robustness	147
5.3 Broader Impact	150
Bibliography	154
VITA	171

LIST OF FIGURES

1.1	A taxonomy of 3-D shape acquisition.	2
1.2	Schematic diagram of structured light illumination.	3
1.3	The cover of LIFE magazine published in 1954 showing an application of SLI.	4
1.4	2-D picture of a gravestone (from http://www.engr.uky.edu/~lgh/soft/softscannerdesigns_RemoteScanner.htm).	5
1.5	3-D reconstruction of a gravestone (from http://www.engr.uky.edu/~lgh/soft/softscannerdesigns_RemoteScanner.htm).	5
1.6	PMP system diagram.	6
1.7	Projected PMP patterns with $N = 4$, $f = 1$, $A^p = 127.5$ and $B^p = 127.5$ (top), and the corresponding captured patterned images (bottom).	7
1.8	Visualization of A^c	8
1.9	Visualizations of B^c (left) and binarized B^c using intensity of 5 as a threshold (right).	9
1.10	Visualizations of the phase with shadow noise (left) and the phase without shadow noise (right).	10
1.11	3-D Reconstruction of the toy object: (left) front view and (right) side view.	10
1.12	A taxonomy on one-shot SLI pattern scheme.	13
1.13	Adaptive one-shot SLI pattern scheme presented by Koninckx et al. [1]: (left) few coding lines with lower coding density, and (right) more coding lines with higher coding density.	14
1.14	Frequency multiplexing one-shot SLI pattern scheme: FTP presented by Takeda et al. (left) and CP presented by Guan et al. (right)	14
1.15	Frequency multiplexing one-shot SLI pattern scheme presented by Yue et al.	15
1.16	Color channels multiplexing one-shot SLI pattern scheme: presented by Wust et al. (left) and Huang et al. (right); projected 2-D color pattern (top) and the cross-section of RGB channels (bottom).	16
1.17	Color channels multiplexing one-shot SLI pattern scheme presented by Mandava et al.	16
1.18	RGB schematic diagram of the scheme presented by Mandava et al. (top-left) red channel, (top-middle) green Channel, (top-right) blue channel, (bottom-left) cross-section of red channel, (bottom-middle) cross-section of green channel, (bottom-right) cross-section of blue channel,	17
1.19	Sawtooth one-shot SLI pattern presented by Chen et al..	17
1.20	Non-formal one-shot SLI pattern presented by Chen et al. [2] (left) and De Bruijn Sequences one-shot SLI pattern presented by Zhang et al. [3] (right).	19
1.21	M-array one-shot SLI pattern presented by Albitar et al. [4].	19
1.22	A real-time 3-D measurement system developed by Zhang et al. [5] in 2006.	21

1.23	A real-time 3-D measurement system developed by Zhang et al. [6] in 2007.	21
1.24	Vector representation of the phase error proposed by Rathjen [7]. The abscissa is the denominator part and the ordinate is the numerator part of the phase-shift algorithm respectively.	23
1.25	PDF of the phase error, proposed by Rathjen [7], for several values of SNR: uncorrelated case (left) and correlated case (right).	23
1.26	The phase error distribution (left) and modulation error distribution (right) in MRI proposed by Gudbjartsson and Patz [8].	24
1.27	The variance of phase error versus the number of patterns (left) and the fringe modulation (right) proposed by Li et al. [9].	25
1.28	Visualizations of wrapped phase (top-left) and unwrapped phase (top-right) of a foam board, and curve plots of the cross-section of the wrapped phase image (bottom-left) and the unwrapped phase image (bottom-right).	26
1.29	Taxonomy of phase unwrapping.	27
1.30	Schematic illustration of the phase fringe counting for spatial phase unwrapping proposed by Nakadate [10].	28
1.31	Graphical representation, checking for all 2×2 sample path inconsistencies, of the spatial phase unwrapping method proposed by Ghiglia et al. [11].	29
1.32	Graphical representation of the spatial phase unwrapping method proposed by Huntley [12]: basic requirement (left) and a cut example (right).	29
1.33	Work flow of the flood fill algorithm proposed by Bone.	30
1.34	An example of circular field segmented into regions for the algorithm proposed by Gierloff.	31
1.35	Labeled with weight, a minimum spanning tree of a planar graph (from http://en.wikipedia.org/wiki/Minimum_spanning_tree)	32
1.36	Minimization of L^0 (left) and L^1 algorithms proposed by Chen and Zebker [13].	33
1.37	Bayesian algorithms proposed by Leitao and Figueiredo [14].	34
1.38	Parametric algorithms proposed by Friedlander and Francos [15].	35
1.39	Gray code temporal phase unwrapping algorithms proposed by Surrrel [16].	36
1.40	Multi-step temporal phase unwrapping [16].	37
1.41	Multiplexed spectra in the spatial frequency domain of the algorithm proposed by Takeda et al. [17].	38
1.42	Composite multi-frequency sinusoidal fringe pattern proposed by Kim et al. [18].	38
1.43	Ideal and distorted ($\gamma = 2.2$) sine wave (left), and the magnitude of the distorted sine wave in the frequency domain (right).	39
1.44	The visualization of magnitude of harmonics: (left) first order, (middle) second order, and (right) third order.	40
1.45	The visualization of phase of harmonics: (left) first order, (middle) second order, and (right) third order.	40
1.46	pre-compensating non-linearity proposed by Huang et al. [19].	41

1.47	Eliminating gamma effects by defocusing projector proposed by Baker et al. [20].	42
1.48	Eliminating gamma effects proposed by Huang et al. [21].	42
1.49	Eliminating gamma effects proposed by Hu et al. [22].	43
1.50	Eliminating gamma effects proposed by Hu et al. [23].	44
1.51	Eliminating gamma effects proposed by Baker et al. [24].	45
1.52	Eliminating gamma effects proposed by Zhang et al. [25].	46
1.53	Eliminating gamma effects proposed by Zhang et al. [26].	47
1.54	Eliminating gamma effects proposed by Guo et al. [27].	48
1.55	Eliminating gamma effects proposed by Pan et al. [28].	48
1.56	A real-time 3-D measurement system developed by Liu et al. [29] in 2010.	51
2.1	Visualizations of MLUT (left) and PLUT (right) for $N = 3$ (top), $N = 4$ (middle) and $N = 6$ (bottom) respectively.	60
2.2	Experimental setup.	68
2.3	Sample video clips.	72
2.4	Sample point clouds, using PMP with $N = 4$, live show of various hand poses.	72
2.5	Our latest real-time 3-D system.	73
3.1	With $w_n \sim N(0, 2.0)$ and $N_1 = N_2 = 3$, the averaged σ_w^2 over 10 measurements is 2.0026.	80
3.2	With $w_n \sim N(0, 2.0)$, $N = 3$, and $\alpha_p = 255$, the variances of $\Delta\alpha$ versus α varying from 0 to 1 by a step of 0.05, in log scale.	83
3.3	With $w_n \sim N(0, 2.0)$, $N = 3$, and $\alpha_p = 255$, the variances of $\Delta\phi$ versus α varying from 0 to 1 by a step of 0.05, in log scale.	84
3.4	Proposed 3-pattern PCMP with $f_h = 3$, $\alpha_p = 200$, $\beta_p = 55$, $c_1 = 0.5$, $c_2 = 0.5$, and $R(y^p) = 2y^p - 1$ (top) and the cross-section of each pattern (bottom).	89
3.5	Normalized variance of the error of reference signal versus the coefficient c_1 for $N = 3$, in log scale.	92
3.6	Proposed 4-pattern PCMP with $f_h = 6$, $\alpha_p = 200$, $\beta_p = 55$, $c_1 = 0.6$, $c_2 = 0.4$, and $R(y^p) = \cos(\pi y^p)$ (top) and the cross-section of each pattern (bottom).	94
3.7	Normalized variance of the error of reference signal versus the coefficient c_1 for $N = 4$	96
3.8	With $w_n \sim N(0, 2.0)$ and $N = 4$, the averaged σ_w^2 over 10 measurements is 1.9983.	97
3.9	Proposed 5-pattern PCMP for with $f_h = 12$, $\alpha_p = 200$, $\beta_p = 55$, $c_1 = 0.7$, and $c_2 = 0.3$ (top) and the cross-section of each pattern (bottom).	99
3.10	With $\sigma_w^2 = 1.6$, $\sigma_{\Delta\alpha_1}^2$, $\sigma_{\Delta\alpha_2}^2$ and $\sigma_{\Delta\alpha}^2$ versus c_1 , in log scale.	100
3.11	For $\sigma_w^2 = 1.6$, the estimated σ_w^2 with c_1 using 5-pattern PCMP.	102
3.12	The histogram of computed β for the pixels with $\alpha \geq 0.5$	104
3.13	Histogram of a measured ΔA^c (left) and all measured σ_w^2 using any 2 groups of 3-pattern PMP among 10 groups (right).	105

3.14	Measured σ_w^2 using B_{cos}^c over 10 group of 4-pattern PMP (left) and a cross-section of B_{cos}^c	105
3.15	Histogram of a measured ΔB_{cos}^c (left) and all measured σ_w^2 using any 2 groups of 4-pattern PMP among 10 groups (right).	106
3.16	Scanned with 3-pattern PCMP, the visualization of unwrapped ϕ_h (left) and the cross-section at 120th column of ϕ_h , ϕ_u , and unwrapped ϕ_h (right) of the board.	106
3.17	Scanned with 3-pattern PCMP and 3-pattern unit-frequency PMP, the cross-section at 320th column of phase error of the board.	107
3.18	Scanned with 3-pattern PMP (left) and PCMP (right), the front view (top) and side view (bottom) of 3-D reconstructed angel.	108
3.19	Scanned with 4-pattern PCMP, the visualization of unwrapped ϕ_h (left) and the cross-section at 120th column of ϕ_h , ϕ_u , and unwrapped ϕ_h (right) of the board.	109
3.20	Scanned with 4-pattern PCMP and 4-pattern unit-frequency PMP, the cross-section at 320th column of phase error of the board.	109
3.21	Side views of the 3-D reconstructed angel using 4-pattern unit-frequency PMP (top-1) and 4-pattern PCMP with $c_1 = 0.5$ and $f_h = 4$ (top-2), $c_1 = 0.5$ and $f_h = 6$ (top-3), $c_1 = 0.5$ and $f_h = 8$ (top-4), $c_1 = 0.6$ and $f_h = 4$ (top-5), $c_1 = 0.6$ and $f_h = 6$ (bottom-1), $c_1 = 0.6$ and $f_h = 8$ (bottom-2), $c_1 = 0.7$ and $f_h = 4$ (bottom-3), $c_1 = 0.7$ and $f_h = 6$ (bottom-4), and $c_1 = 0.7$ and $f_h = 8$ (bottom-5).	111
3.22	Scanned with 5-pattern PCMP, the visualization of unwrapped ϕ_h (left) and the cross-section at 120th column of ϕ_h , ϕ_u , and unwrapped ϕ_h (right) of the board.	111
3.23	Scanned with 5-pattern PCMP and 5-pattern unit-frequency PMP, the cross-section at 320th column of phase error of the board.	112
3.24	Side views of the 3-D reconstructed angel using 5-pattern unit-frequency PMP (top-1) and 5-pattern PCMP with $c_1 = 0.5$ and $f_h = 6$ (top-2), $c_1 = 0.5$ and $f_h = 8$ (top-3), $c_1 = 0.5$ and $f_h = 12$ (top-4), $c_1 = 0.6$ and $f_h = 6$ (top-5), $c_1 = 0.6$ and $f_h = 8$ (bottom-1), $c_1 = 0.6$ and $f_h = 12$ (bottom-2), $c_1 = 0.8$ and $f_h = 6$ (bottom-3), $c_1 = 0.8$ and $f_h = 8$ (bottom-4), and $c_1 = 0.8$ and $f_h = 12$ (bottom-5).	113
4.1	Coefficients B_k	117
4.2	Ratios of $\frac{B_{k+1}}{B_k}$	118
4.3	$ B_k $ in log scale.	119
4.4	The absolute phase Error for different N.	123
4.5	The RMS of phase error for different N in log scale.	124
4.6	RMS of Phase Error for different N in log scale.	124
4.7	Gamma computation versus the number of patterns, N , showing (left) the computed gamma and (right) the RMS of error in log scale.	128
4.8	The (left) distorted and corrected phase for $\gamma = 3.18$ and the (right) corresponding distorted and corrected phase error using $N = 3$ constrained phase optimization without gamma calibration.	130

4.9	The (left) distorted and corrected phase for $\gamma = 6.36$ and the (right) corresponding distorted and corrected phase error using $N = 4$ constrained phase optimization without gamma calibration.	131
4.10	The (left) distorted and corrected phase for $\gamma = 10.36$ and the (right) corresponding distorted and corrected phase error using $N = 5$ constrained phase optimization without gamma calibration.	132
4.11	Gamma correction with phase matching.	133
4.12	Photos of the scanned objects used in our experiment showing (left) a white board with uniform texture and (right) a plastic fish with varying texture.	134
4.13	The ground truth of 3-D reconstructions of the textureless foam board (left) and the textured plastic fish (right) viewed from the front (top) and from above (bottom).	134
4.14	The (left) best-fit curve for a pixel with a measured gamma value of 2.153 and (right) the histogram of the calibrated gamma in the entire image where the mean is 2.2123 with variance 2.67×10^{-4}	135
4.15	The error of distorted phase and corrected phase (with gamma calibration) for $\gamma = 2.21$ of the 512th row of the board.	136
4.16	The 3-D reconstructions of the textureless foam board viewed from the front and from above for the (left) uncorrected phase and (right) corrected phase with gamma calibration.	137
4.17	The 3-D reconstructions of the textured plastic fish viewed from the front and from above for the (left) uncorrected phase and (right) corrected phase with gamma calibration.	137
4.18	Employing a second constraint for $N=3$, the error of gamma distorted phase and corrected phase for $\gamma = 2.21$ of the 512th row of the board. . .	138
4.19	The 3-D reconstructions of the textureless foam board viewed from the front and from above for the (left) uncorrected phase and (right) corrected phase with $N = 3$ constrained gamma and phase optimization.	139
4.20	The 3-D reconstructions of the textured plastic fish viewed from the front and from above for the (left) uncorrected phase and (right) corrected phase with $N = 3$ constrained gamma and phase optimization.	139
4.21	Employing a second constraint for $N=4$, the error of gamma distorted phase and corrected phase for $\gamma = 4.42$ of the 512th row of the board. . .	140
4.22	The 3-D reconstructions of the textureless foam board viewed from the front and from above for the (left) uncorrected phase and (right) corrected phase with $N = 4$ constrained gamma and phase optimization.	141
4.23	The 3-D reconstructions of the textured plastic fish viewed from the front and from above for the (left) uncorrected phase and (right) corrected phase with $N = 4$ constrained gamma and phase optimization.	141
4.24	Employing a second constraint for $N=5$, the error of gamma distorted phase and corrected phase for $\gamma = 7.73$ of the 512th row of the board. . .	142
4.25	The 3-D reconstructions of the textureless foam board viewed from the front and from above for the (left) uncorrected phase and (right) corrected phase with $N = 5$ constrained gamma and phase optimization.	142

4.26 The 3-D reconstructions of the textured plastic fish viewed from the front and from above for the (left) uncorrected phase and (right) corrected phase with $N = 5$ constrained gamma and phase optimization. 143

LIST OF TABLES

2.1	Comparison of three kinds of 3-D reconstruction LUTs	67
2.2	Processing time and rate, in milliseconds and frames per second (in parentheses), respectively, for various stages of PMP processing by means of the equations and LUT described in this paper.	69
3.1	Percentage of pixels successfully phase unwrapped for $N = 3$ with different f_h and α_p	93
3.2	Percentage of pixels successfully phase unwrapped for $N = 4$ with different f_h and c_1	96
3.3	Percentage of pixels successfully phase unwrapped for $N = 5$ with different f_h and c_1	103
3.4	Percentage of pixels successfully unwrapped for 4-pattern PCMP with different f_h and c_1	110
3.5	For successfully unwrapped pixels, the ratio of the variance of 4-pattern PCMP over the variance of 4-pattern unit-frequency PMP (experimental measurement/theoretical prediction).	110
3.6	Percentage of pixels successfully phase unwrapped for 5-pattern PCMP with different f_h and c_1	112
3.7	For the successfully unwrapped pixels, the ratio of the variance of 5-pattern PCMP over the variance of 5-pattern unit-frequency PMP (experimental measurement/theoretical prediction).	113
4.1	RMS of phase error (the RMS of phase error is 0.3033 before correction)	129

Chapter 1 Introduction

Three dimensional (3-D) shape measurement is an very important topic covering nearly all areas in science and industry including product inspection, 3-D modeling for stereo movie/TV, security surveillance, medical imaging, human-computer-interfacing (HCI), and so forth. With this broad array of applications, numerous methods of 3-D shape measurement have been developed as has been summarized by Curless and Seitz [30] who made the taxonomy on 3-D shape acquisition techniques shown in Figure 1.1.

The first of Curless and Seitz's classifications is between contact and non-contact techniques where, although contact approaches have advantages in directly measuring rigid targets, they suffer from the distortion of soft objects such as a human finger and are invasive. Within the array of non-contact methods, transmissive approaches need the help of special and expensive hardware. By means of a non-optical signal source such as a microwave or sonar transmitter, those methods are suitable for measuring large scale scenes remotely. Within the array of non-contact optical methods, passive algorithms (with the exception of stereo vision) employ only one information source, which is not reasonable in determinant mathematics, so currently they are only in the stage of research. Stereo-vision solves the theoretical issue of not having enough views in order to reconstruct 3-D non-ambiguously but, as a passive approach, ambiguities still arise depending on the scene. Of the non-contact optical active techniques, triangulation-based methods are an easily understandable technology.

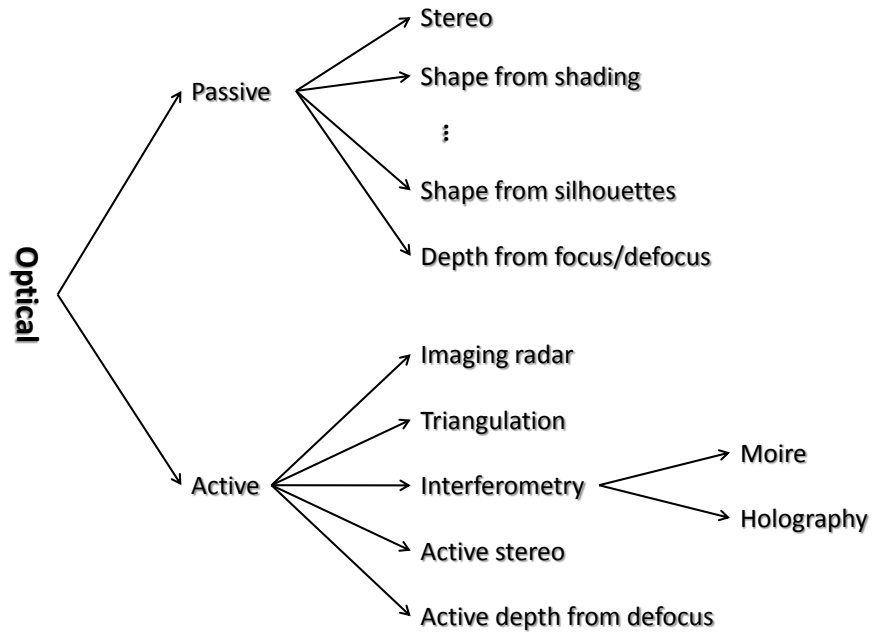
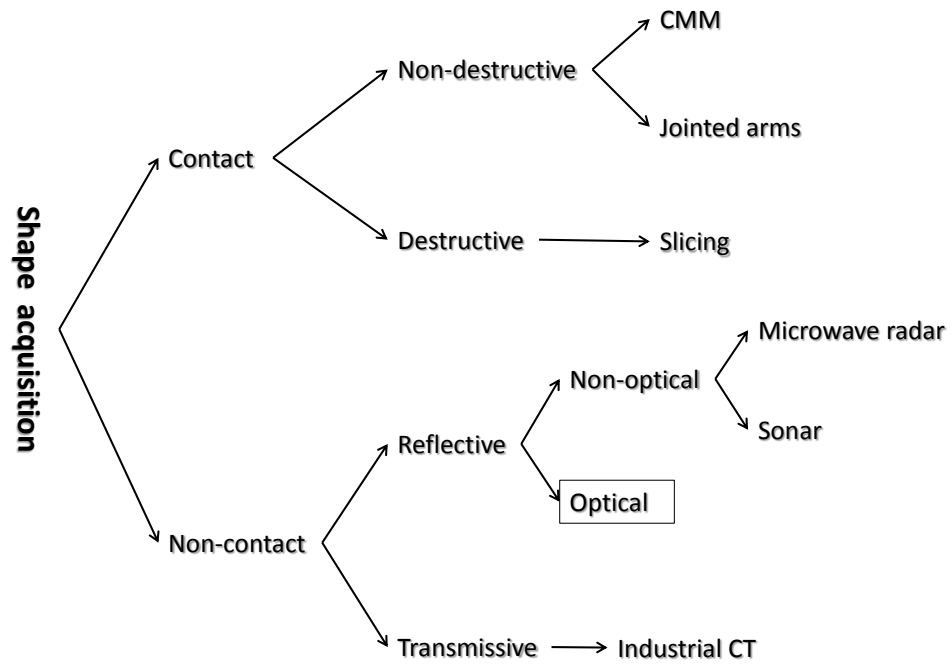


Figure 1.1: A taxonomy of 3-D shape acquisition.

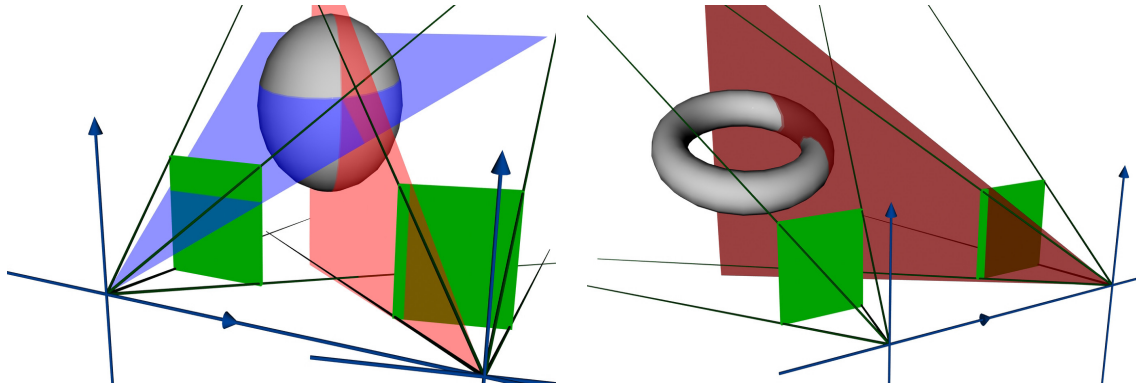


Figure 1.2: Schematic diagram of structured light illumination.

1.1 Structured light illumination

According to the Curless and Seitz taxonomy, structured light illumination (SLI) [31, 32, 33, 34] falls within this category of non-contact, reflective, optical, active, and triangulation-based. SLI is well-known for its simple implementation, low cost, high speed and high accuracy [35,36,37,38,39,40], and has been studied for decades [41,42]. For example, the cover from the Dec. 1954 issue of LIFE magazine, as illustrated in Fig. 1.3, shows SLI was being used to measure the size and shape of a pilot's head for the purpose of making custom fitting helmets. Figure 1.4 shows a 2-D image of a gravestone and Fig. 1.5 shows the 3-D reconstruction of that gravestone. Dr. Hassebrook, the leader of that research project, said "It should be noted that our team thought that the date was 1818 until we performed the scan. The thin front line of the four along with the angle of the primary groove differentiate the '4' from the '1'" (http://www.engr.uky.edu/~lgh/soft /softscannerdesigns_RemoteScanner.htm).

In practice, the simplest SLI system is composed of one camera, one projector, and a processing unit (computer). Controlled by the computer, a series of well-designed



Figure 1.3: The cover of LIFE magazine published in 1954 showing an application of SLI.

patterns are projected onto a target object while the camera captures the corresponding images, which contain information of the projected patterns, that are sent back to the computer. The computer then performs some kind of decoding algorithm to extract coordinate information from the scanned object connecting camera and projector coordinates such that the 3-D shape of the object can be measured by the triangulation. Figure 1.2 shows the triangulation relationship among the camera, the projector and the scanned object.

With regards to accuracy, the most important issue is how to design the projected patterns, i.e., how to design coding strategy and its corresponding decoding algorithm. The coding and decoding algorithms will decide the final quality of reconstructed 3-D data of the scanned object. As so far, there is no perfect pattern scheme satisfying



Figure 1.4: 2-D picture of a gravestone (from http://www.engr.uky.edu/~lgh/soft/softscannerdesigns_RemoteScanner.htm).

all situations, and so many SLI pattern strategies have been proposed in the past and are still being studied today. Numerous classifications have been proposed for the many pattern coding strategies according to the features of the patterns [35]. Typically, the projected patterns are a set of well-designed 2-D images, while there also exist two forms of patterns, i.e., dot pattern and line pattern, which are often employed when the light source is a laser [43, 44].

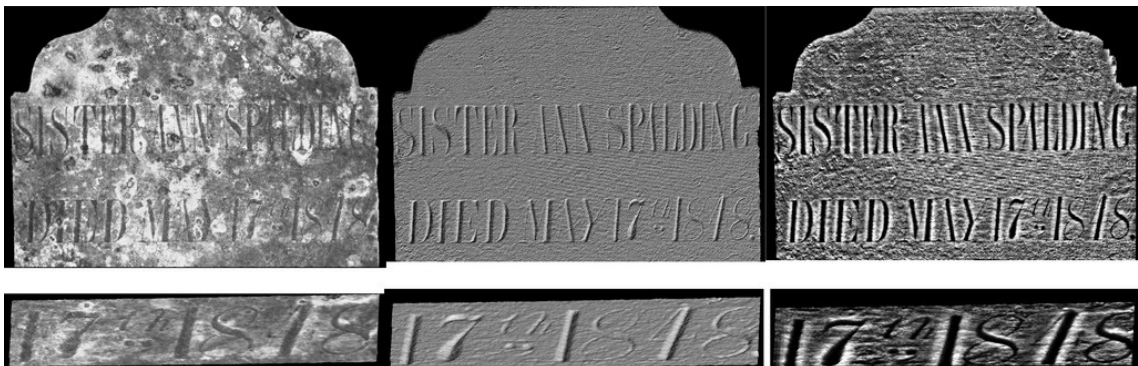


Figure 1.5: 3-D reconstruction of a gravestone (from http://www.engr.uky.edu/~lgh/soft/softscannerdesigns_RemoteScanner.htm).

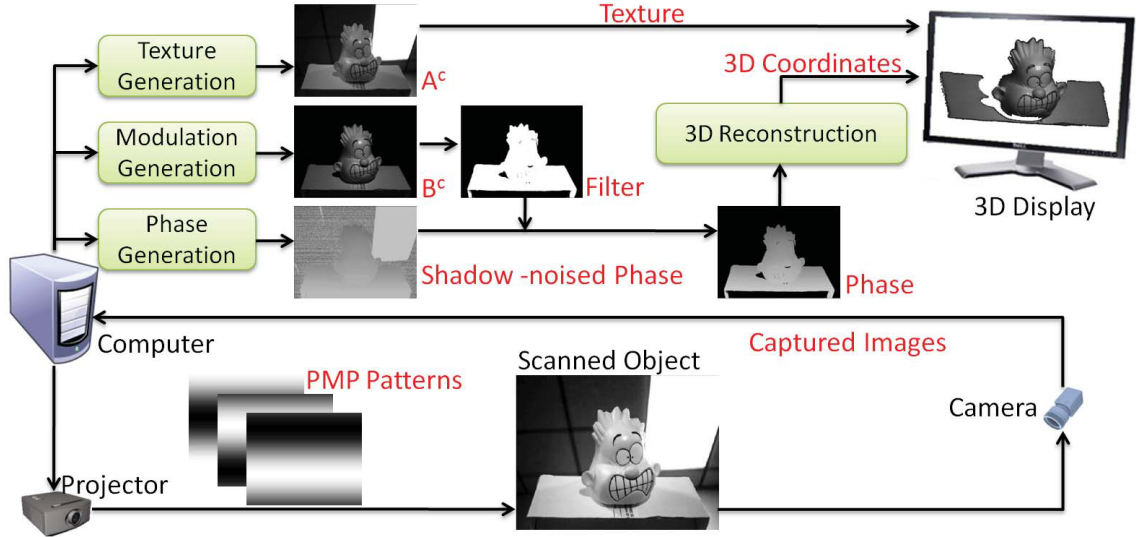


Figure 1.6: PMP system diagram.

If a digital light processing (DLP) or digital micromirror device (DMD) projector is involved as light source, 2-D image pattern strategies are always preferred for fast scanning. Salvi et al. reviewed these pattern schemes in 2004 [35]. Although many novel schemes have been designed since 2004, typically any 2-D pattern strategy must fall into one of two kinds of classifications of 2-D pattern schemes, i.e., one-shot and multi-shot schemes. One-shot patterns are robust to motion but suffer from inaccuracy and high-cost computation [32]. Multi-shot pattern strategies, on the other hand, are good at scanning a static objects and achieve very high accuracy.

Of the many SLI multi-shot pattern schemes, phase measuring profilometry (PMP) is famous for its robust and depth accuracy [45, 46, 47, 48]. Figure 1.6 shows a basic process of PMP scanning. In practice, either vertical or horizontal sinusoid patterns are projected onto a target object so that the vertical or horizontal correspondence information, between the camera and the projector, can be directly derived from the

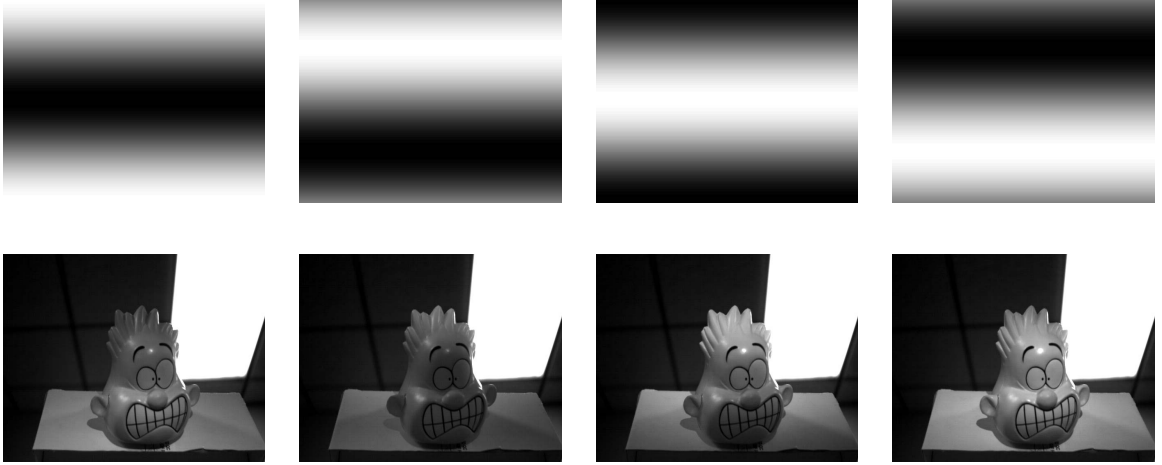


Figure 1.7: Projected PMP patterns with $N = 4$, $f = 1$, $A^p = 127.5$ and $B^p = 127.5$ (top), and the corresponding captured patterned images (bottom).

computed phase data. The PMP patterns are described as:

$$I_n^p(x^p, y^p) = A^p(x^p, y^p) + B^p(x^p, y^p) \cos\left(2\pi f y^p - \frac{2\pi n}{N}\right), \quad (1.1)$$

where (x^p, y^p) is the coordinates of a pixel in the projector, I_n^p is the intensity of that pixel, A^p and B^p are some constants, f is the frequency of the sine wave, n represents the phase-shift index, and N is the total number of phase shift. Figure 1.7 (top) shows a group of sine wave patterns with $N = 4$, $f = 1$, $A^p = 127.5$ and $B^p = 127.5$ for 8-bits color depth projector are projected.

For reconstruction, a camera captures each image where the sine wave pattern is distorted by the scanned surface topology, resulting in the patterned images expressed as:

$$I_n^c(x^c, y^c) = A^c(x^c, y^c) + B^c(x^c, y^c) \cos\left[\phi(x^c, y^c) - \frac{2\pi n}{N}\right], \quad (1.2)$$

where (x^c, y^c) is the coordinates of a pixel in the camera while $I_n^c(x^c, y^c)$ is the intensity of that pixel. Figure 1.7 (bottom) shows a group of captured patterned images corresponding to the patterns in Fig. 1.7 (top). To simplify the notation, the coor-



Figure 1.8: Visualization of A^c .

indexes both in the camera and projector will be removed from our equation henceforth.

The term A^c is the averaged pixel intensity across the pattern set, which can be derived according to:

$$A^c = \frac{1}{N} \sum_{n=0}^{N-1} I_n^c \quad (1.3)$$

such that the image A^c is equal to an intensity or texture photograph of the scene and a visualization of A^c is shown in Fig. 1.8. Correspondingly, the term B^c is the intensity modulation of a given pixel and is derived from I_n^c as:

$$B^c = \left(S_N^2 + C_N^2 \right)^{0.5}, \quad (1.4)$$

where

$$S_N = \frac{2}{N} \sum_{n=0}^{N-1} \left[I_n^c \sin \left(\frac{2\pi n}{N} \right) \right] \quad (1.5)$$

and

$$C_N = \frac{2}{N} \sum_{n=0}^{N-1} \left[I_n^c \cos \left(\frac{2\pi n}{N} \right) \right]. \quad (1.6)$$

The term B^c can be thought of as the amplitude of the sinusoid reflecting off of a point on the target surface.

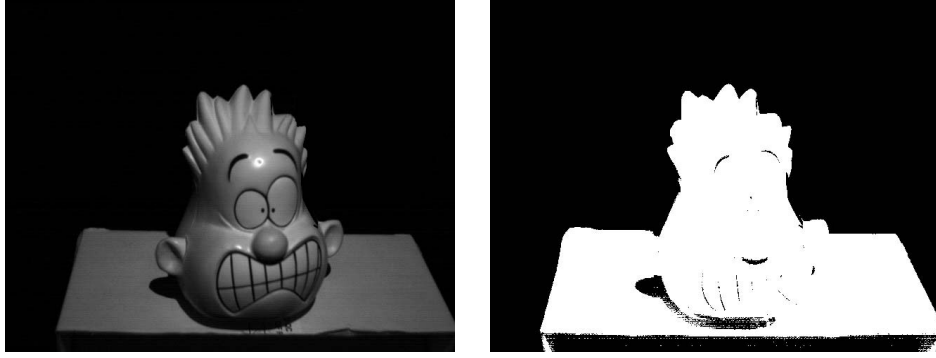


Figure 1.9: Visualizations of B^c (left) and binarized B^c using intensity of 5 as a threshold (right).

If I_n^c is constant or less affected by the projected sinusoid patterns, B^c will be close to zero. Thus B^c is employed as a shadow noise detector/filter [49] such that the shadow-noised regions, with small B^c values, are discarded from further processing. Figure 1.7 (bottom) shows, an example scene with a background that includes a fluorescent ceiling light, which over saturates the camera's pixel and, thereby, erases any signal from the SLI projector. In Fig. 1.8, A^c looks like a standard video frame absent any indication of the projected pattern sequence I_n^p . In contrast, B^c , shown in Fig. 1.9 (left), looks very similar to A^c except that it only shows texture in those areas of the scene that significantly reflect the projected sequence I_n^p . Given the significance of B^c as an indicator of the projected signal strength, the binarized image in Fig. 1.9 (right) shows only those pixels greater in magnitude to a user defined threshold. It is these pixels that will ultimately be used to reconstruct our 3-D surface with ignored pixels being considered too noisy as to relay a reliable depth information.

Of the reliable pixels with sufficiently large B^c , ϕ represents the phase value of

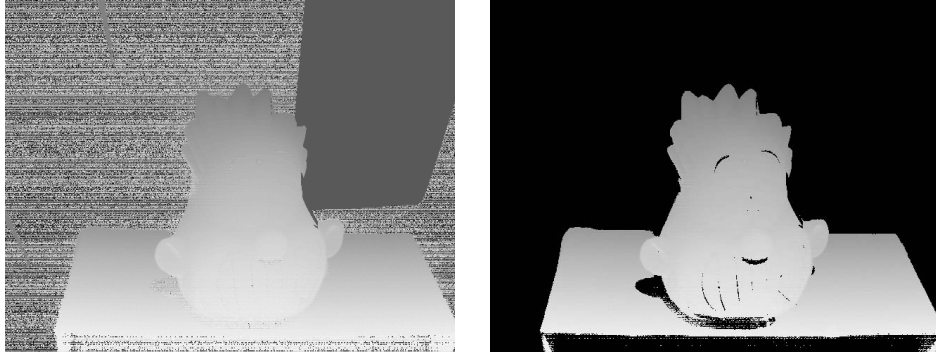


Figure 1.10: Visualizations of the phase with shadow noise (left) and the phase without shadow noise (right).

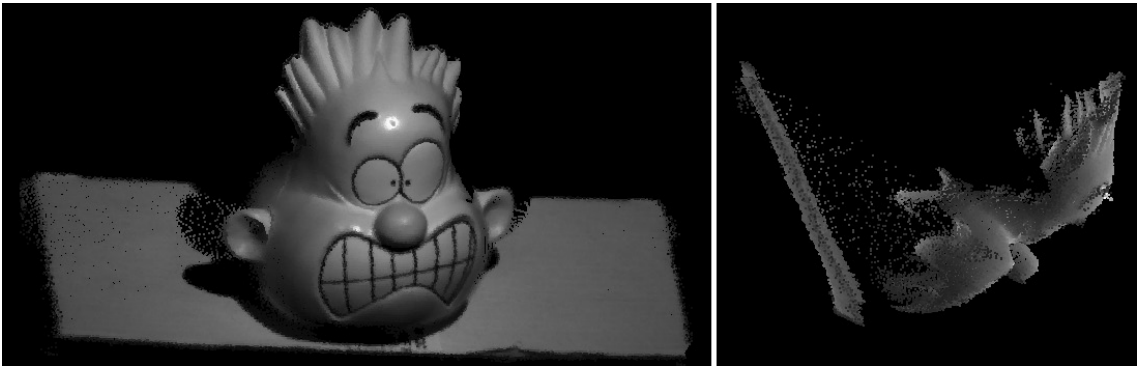


Figure 1.11: 3-D Reconstruction of the toy object: (left) front view and (right) side view.

the captured sinusoid pattern derived as:

$$\phi = \arctan\left(\frac{S_N}{C_N}\right). \quad (1.7)$$

In Fig. 1.10 (right), we show the resulting phase image corresponding to the scene from sine wave patterns. For reference, Fig. 1.10 (left) also shows the phase values for all pixels, including those considered unreliable according to B^c .

Having derived the phase image ϕ , we likewise have derived a unique correspondence value y^p for every camera pixel (x^c, y^c) through the linear equation

$$\phi = 2\pi f y^p. \quad (1.8)$$

The 3-D world coordinates of the scanned object can, therefore, be derived through triangulation with the projector [9] where, under the assumption that the camera and projector are accurately modeled using the pinhole lens model such that their perspective matrices, M^c and M^p , are calibrated [50, 51] and given by:

$$M^c = \begin{pmatrix} m_{11}^c & m_{12}^c & m_{13}^c & m_{14}^c \\ m_{21}^c & m_{22}^c & m_{23}^c & m_{24}^c \\ m_{31}^c & m_{32}^c & m_{33}^c & m_{34}^c \end{pmatrix} \quad (1.9)$$

and

$$M^p = \begin{pmatrix} m_{11}^p & m_{12}^p & m_{13}^p & m_{14}^p \\ m_{21}^p & m_{22}^p & m_{23}^p & m_{24}^p \\ m_{31}^p & m_{32}^p & m_{33}^p & m_{34}^p \end{pmatrix}. \quad (1.10)$$

The map from 3-D world coordinates X^w , Y^w , and Z^w to 2-D camera coordinates x^c and y^c are [50]

$$x^c = \frac{m_{11}^c X^w + m_{12}^c Y^w + m_{13}^c Z^w + m_{14}^c}{m_{31}^c X^w + m_{32}^c Y^w + m_{33}^c Z^w + m_{34}^c} \quad (1.11)$$

and

$$y^c = \frac{m_{21}^c X^w + m_{22}^c Y^w + m_{23}^c Z^w + m_{24}^c}{m_{31}^c X^w + m_{32}^c Y^w + m_{33}^c Z^w + m_{34}^c}. \quad (1.12)$$

In the same way, the map from 3-D world coordinates X^w , Y^w , and Z^w to 2-D projector coordinates x^p and y^p are

$$x^p = \frac{m_{11}^p X^w + m_{12}^p Y^w + m_{13}^p Z^w + m_{14}^p}{m_{31}^p X^w + m_{32}^p Y^w + m_{33}^p Z^w + m_{34}^p} \quad (1.13)$$

and

$$y^p = \frac{m_{21}^p X^w + m_{22}^p Y^w + m_{23}^p Z^w + m_{24}^p}{m_{31}^p X^w + m_{32}^p Y^w + m_{33}^p Z^w + m_{34}^p}. \quad (1.14)$$

There are four equations, i.e., Eqs. 1.11, 1.12, 1.13, and 1.14, relating to the 3-D coordinates, so three of the four equations are enough to solve X^w , Y^w , and Z^w . In

this study, we choose Eqs. 1.11, 1.12, and 1.14, and the 3-D world coordinates X^w , Y^w , and Z^w are derived as

$$\begin{pmatrix} X^w \\ Y^w \\ Z^w \end{pmatrix} = \begin{pmatrix} m_{11}^c - m_{31}^c x^c, & m_{12}^c - m_{32}^c x^c, & m_{13}^c - m_{33}^c x^c \\ m_{21}^c - m_{31}^c y^c, & m_{22}^c - m_{32}^c y^c, & m_{23}^c - m_{33}^c y^c \\ m_{21}^p - m_{31}^p y^p, & m_{22}^p - m_{32}^p y^p, & m_{23}^p - m_{33}^p y^p \end{pmatrix}^{-1} \begin{pmatrix} m_{14}^c - m_{34}^c x^c \\ m_{24}^c - m_{34}^c y^c \\ m_{24}^p - m_{34}^p y^p \end{pmatrix}. \quad (1.15)$$

Figure 1.11 shows the 3-D reconstruction of the toy object with front view (left) and side view (right). It is this matrix inversion as well as the actangent computation in Eq. (1.7) that will prove to be the bottleneck preventing real-time surface reconstruction, as will be discussed later.

Single Pattern SLI

As an active range-sensing method, SLI is computationally simple and achieves high precision [9], but it does so requiring a time-consuming scan procedure involving a series of time-multiplexed patterns. To achieve real-time operation, researchers have relied on one-shot methods while others have proposed employing a high-speed camera and projector pair. As stated previously, one-shot SLI techniques are attractive for their insensitiveness to object motion [32]. There are many one-shot SLI pattern schemes and they are classified into several categories illustrated in Fig. 1.12. Pagès et al. also made an overview on one-shot pattern strategy in [52] in 2005.

Typically, the SLI patterns are pre-designed and fixed during the scanning period, but in order to achieve real time, Konickx et al. [1] proposed a dynamic single-pattern strategy designed to be “self-adaptive” with the varying of the scenes or circumstances. Their basic pattern is illustrated in Figure 1.13 where a weighted

combination of different coding cues was employed to solve the correspondence issue robustly according to pattern color, geometry, and tracking. For the pipeline of “project structured light”, “video capture”, “segmentation and pattern identification”, and “integrate and visualize”, the averaged frame rate was 14.5 frame per second (fps) over 10,000 points/frame using a single desktop computer equipped with a Pentium 4 CPU at 2.26 GHz.

Within the array of static one-shot SLI coding strategies, frequency multiplexing methods have gained particular attention because they combine multiple time-multiplexed and phase-shifted gray-scale patterns into a single pattern by applying traditional modulating techniques with the captured patterned image demodulated to

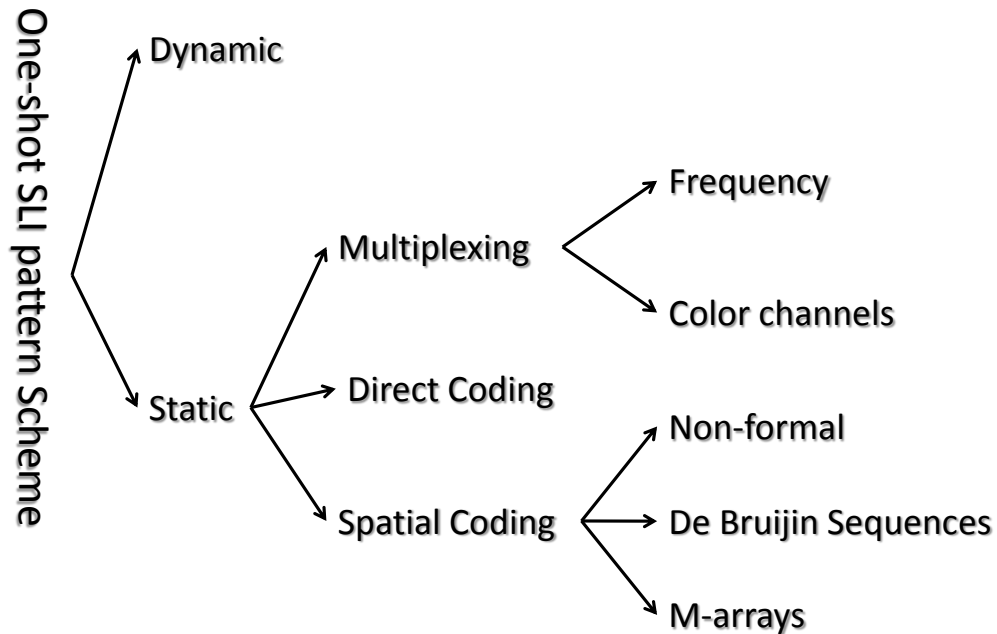


Figure 1.12: A taxonomy on one-shot SLI pattern scheme.

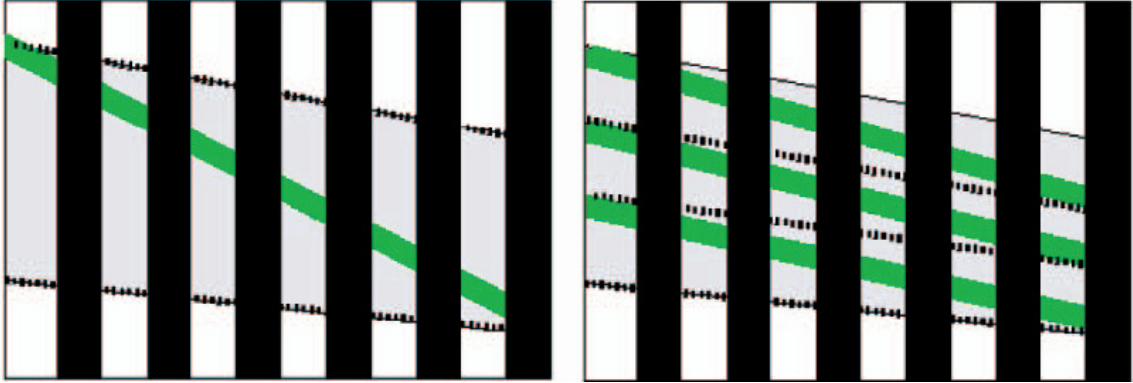


Figure 1.13: Adaptive one-shot SLI pattern scheme presented by Koninckx et al. [1]: (left) few coding lines with lower coding density, and (right) more coding lines with higher coding density.

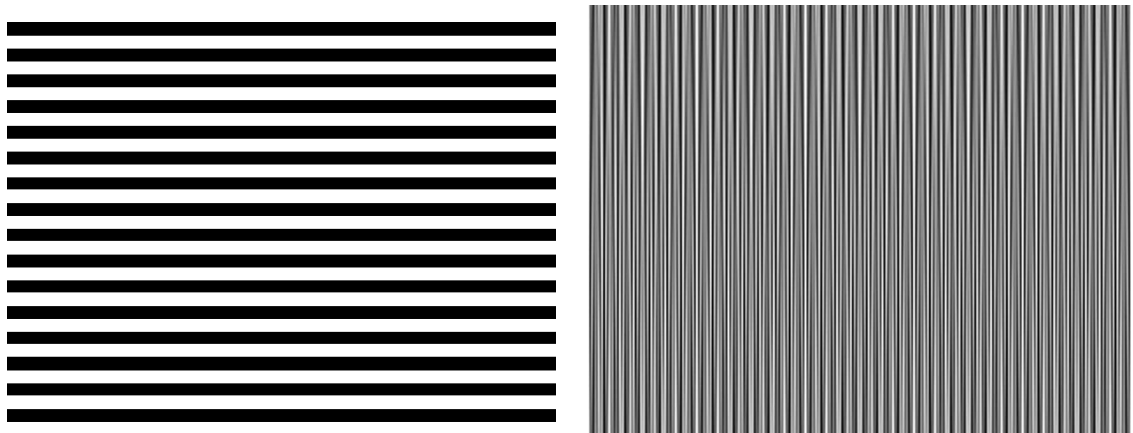


Figure 1.14: Frequency multiplexing one-shot SLI pattern scheme: FTP presented by Takeda et al. (left) and CP presented by Guan et al. (right)

produce several regular multi-shot SLI patterned images. The most famous of these is called Fourier transform profilometry (FTP) [53, 17, 54, 55] presented by Takeda et al. in 1983 and shown in Fig. 1.14 (left). Guan et al. proposed another frequency multiplexing pattern named composite pattern (CP) [32, 56, 42] in 2003 which is shown in Fig. 1.14 (right). Yue et al. [57] proposed a one-shot scheme based on both FTP and CP as illustrated in Fig. 1.15. Frequency multiplexing methods, like these, can achieve a high-quality 3-D reconstruction in theory or simulation. However, in

practice, suffering from band width or color depth of both the projector and camera and the issue of quantization, it is difficult for frequency multiplexing methods to perform as good as simulation. Another problem for frequency multiplexing methods is that the computational cost is very high during the procedure of demodulation, so typically this methods can only capture patterned images in real time and perform post-processing to generate phase maps and reconstruct 3-D point clouds.

Another category of one-shot pattern multiplexing takes advantage of available color channels, i.e., red, green, and blue, of a color projector (or light source) and a color camera [58, 59, 60, 61, 62]. Once a patterned color image is captured, three gray-scale images can be extracted from the RGB channels of the color image, and then some kind of three-step phase-shift decoding algorithm can be performed to generate phase data. This technique sounds better than frequency multiplexing but, in practice, is easily affected by the surface color of scanned object [5], which affects the color channels in non-uniform ways. Figure 1.16 shows the pattern schemes



Figure 1.15: Frequency multiplexing one-shot SLI pattern scheme presented by Yue et al.

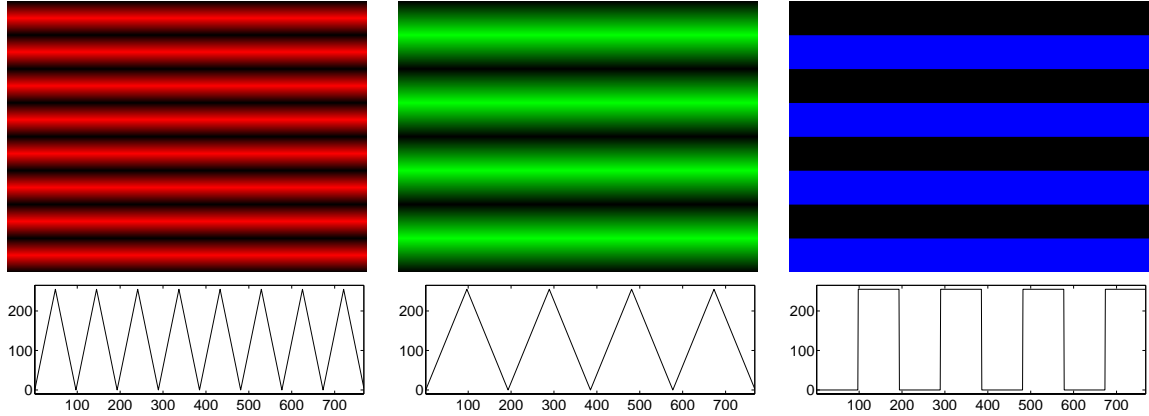


Figure 1.18: RGB schematic diagram of the scheme presented by Mandava et al. (top-left) red channel, (top-middle) green Channel, (top-right) blue channel, (bottom-left) cross-section of red channel, (bottom-middle) cross-section of green channel, (bottom-right) cross-section of blue channel,

et al. [62]. In an effort to reduce the effects of surface color, Su [63] combined color channel multiplexing with FTP, but the bottleneck issue remained unsolved with regards to phase generation and 3-D reconstruction in real time.

Direct coding one-shot pattern strategies are based on the varying intensity of the scanned object under a projected pattern. Obviously this kind of strategy suffers from the textured surface of the object. For instance, Chen et al. proposed a sawtooth



Figure 1.19: Sawtooth one-shot SLI pattern presented by Chen et al..

one-frame pattern [64] shown in Fig. 1.19. The phase was extracted through a linear translation and the scanned object was required with uniform texture.

When a one-shot SLI pattern strategy is based on spatial neighborhood coding, pre-defined codewords can identify a particular point of the pattern by extracting the neighborhood points around it [35]. Such neighborhood coding patterns, typically, can be classified into three types: non-formal codification [65, 66, 2], De Bruijn Sequences [67, 3, 52], and M-arrays [68, 69, 4]. According to Salvi et al., non-formal codification means researchers generate the neighborhoods information intuitively without involving any mathematical coding theory; De Bruijn sequences indicate the neighborhoods are generated by means of pseudorandom sequences whose sort can be derived through searching Eulerian circuits or Hamiltonian circuits over different kinds of De Bruijn graphs [70]; and M-arrays extends the pseudorandom theory from 1-D to 2-D by folding a pseudorandom sequence. Figure 1.20 (left) shows the non-formal one-shot SLI scheme presented by Chen et al. [2]. Figure 1.20 (right) shows the De Bruijn sequences one-shot SLI scheme presented by Zhang et al. [3]. Figure 1.21 shows the M-array one-shot SLI scheme presented by Albitar et al. [4].

Fast Multi-Pattern SLI

Although one-shot SLI pattern strategies can solve the problem of motion, they achieve poor resolution compared to multi-shot SLI methods [35] and suffer from higher computational cost [32]. For this reason, various authors have attempted to achieve the same high resolution typically associated with SLI where resilience to motion is achieved by driving the camera/projector pair at such high frame rates as to

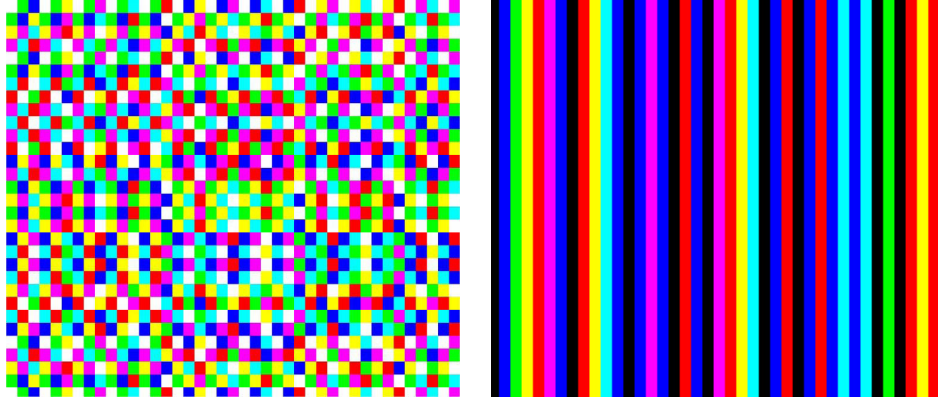


Figure 1.20: Non-formal one-shot SLI pattern presented by Chen et al. [2] (left) and De Bruijn Sequences one-shot SLI pattern presented by Zhang et al. [3] (right).

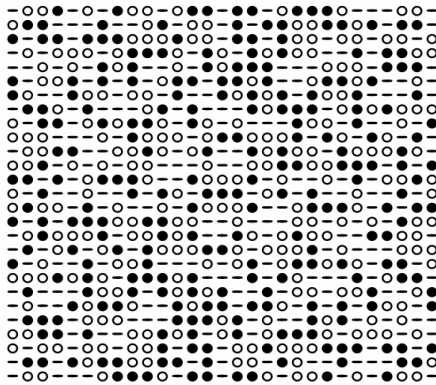


Figure 1.21: M-array one-shot SLI pattern presented by Albitar et al. [4].

minimize object motion. A study of particular importance has been led by Zhang and Huang et al. [5,6] where Zhang et al. employed a novel, fast, three-step, phase-shifting algorithm for phase generation instead of the traditional time-consuming arctangent function [71].

For 3-D reconstruction of point clouds, a phase-to-height conversion algorithm was involved by assuming that surface height was proportional to the difference between the phase maps of the object and a reference plane [72]. Figure 1.22 shows the real-time 3-D measurement system developed by Zhang et al. [5] in 2006. The resolution

of the camera used in their real-time system was 532×500 . Processing data with a Pentium 4, 2.8-GHz CPU workstation, the speed of data acquisition was 120 fps; the speed of phase generation was 163.93 fps, which was 3.4 times faster than the traditional arctangent function; and the speed of 3-D reconstruction was 80 fps.

In [6], Zhang et al. modified the three-step phase-shifting algorithm, which is called two plus one (2+1) and was originally proposed by Wizinowich et al. [73], to attempt to further reduce the effects of motion. Figure 1.23 shows the real-time 3-D measurement system developed by Zhang et al. [6] in 2007. The resolution of the camera used in that system was 640×480 with a frame rate of 180 fps. They claimed that the speed of phase generation was 2 times faster than the arctangent function, however, they could not reconstruct 3-D point clouds in real time because the absolute 3-D coordinates [9, 51] were involved instead of the phase-to-height representation. And finally, they had to record the patterned images on hard disk and then post-process the recorded data. The trouble for Zhang et al. on the absolute 3-D coordinates was that they employed a matrix inverse operation to compute 3-D coordinates, and even with the assistance of GPU [74], the frame rate of 3-D reconstruction was only sped up from 6 fps to 25.56 fps, which was still very slow compared with the speed of data acquisition.

1.2 Pattern Robustness

With regards to reconstruction quality, fast SLI schemes which attempt to minimize the number of component SLI patterns, in order to minimize the affects of motion, do so at the cost of becoming increasingly sensitive to sensor noise and pattern dis-

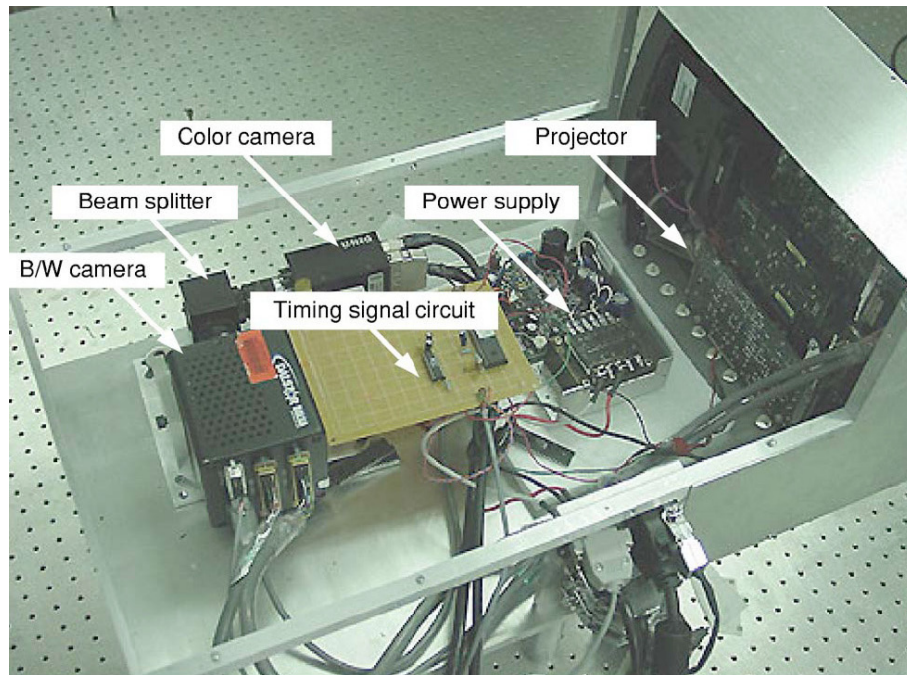


Figure 1.22: A real-time 3-D measurement system developed by Zhang et al. [5] in 2006.

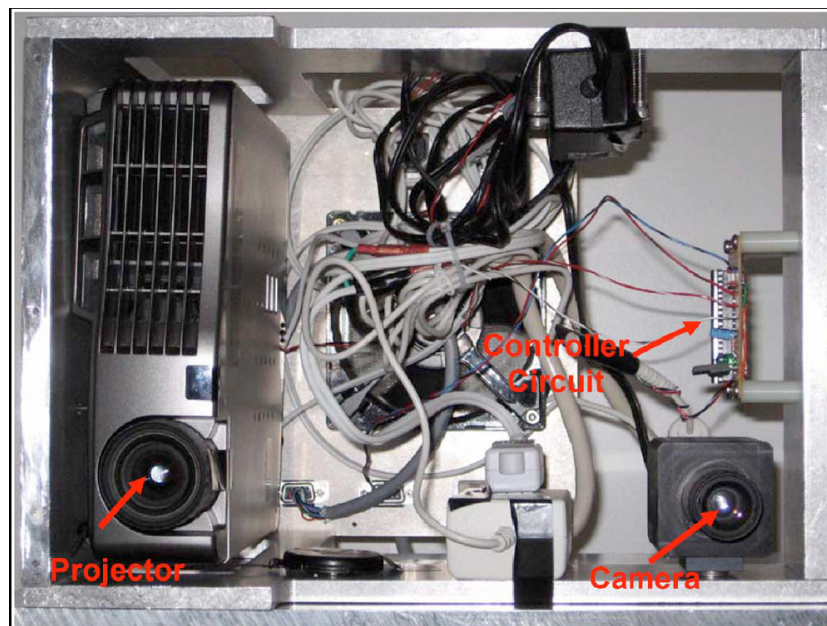


Figure 1.23: A real-time 3-D measurement system developed by Zhang et al. [6] in 2007.

tortion. We group any undesired, uncertain, and/or additive signal appearing in the captured images into sensor noise, which is typically from thermal (Gaussian) and shot (Poissonian) noise. Both of which are unavoidable in electrical circuits [75]. Distortion is typically constituted as Gamma distortion caused by the non-linear response of the optical device, and it is a kind of certain and systematic error that can be compensated for in the pattern demodulation.

Additive Noise

Looking specifically at the problem of sensor noise, many studies have been performed on understanding and/or reducing its effects on the resulting phase reconstruction [9, 7, 76, 77, 78]. Surrrel investigated the additive noise effect in digital phase detection [79] where characteristic polynomials [80] were employed to help defining a loss factor. The loss factor described how the global Signal-to-Noise-Ratio (SNR) would influence phase quality in a given phase-shifting based algorithm. After analyzed nineteen phase-shift algorithms with the proposed loss factor, Surrrel found that the variance of the phase error depended mainly on the global SNR and some algorithms introduced a modulation, whose amplitude depended on a single parameter, of the variance at twice the signal frequency.

Rathjen studied statistical properties of phase-shift algorithms for the case of additive Gaussian intensity noise [7]. Based on a vector representation and a bivariate Gaussian distribution, the investigation of the random phase error was extended to a more general description. With the new description, which was not restricted to large SNR ratios, of phase error, new statistical properties, as well as the corresponding

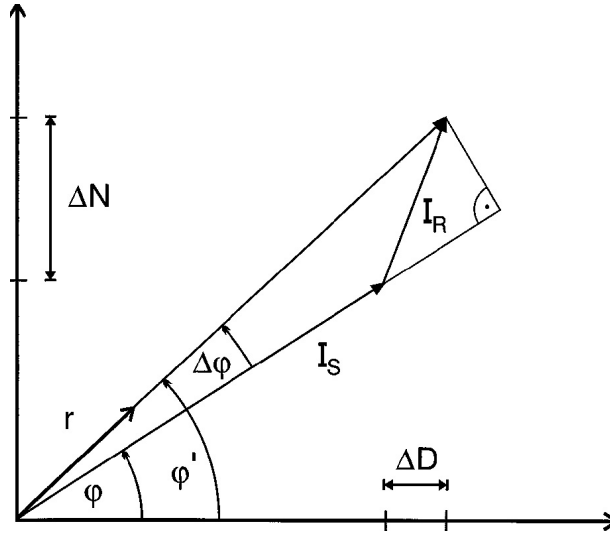


Figure 1.24: Vector representation of the phase error proposed by Rathjen [7]. The abscissa is the denominator part and the ordinate is the numerator part of the phase-shift algorithm respectively.

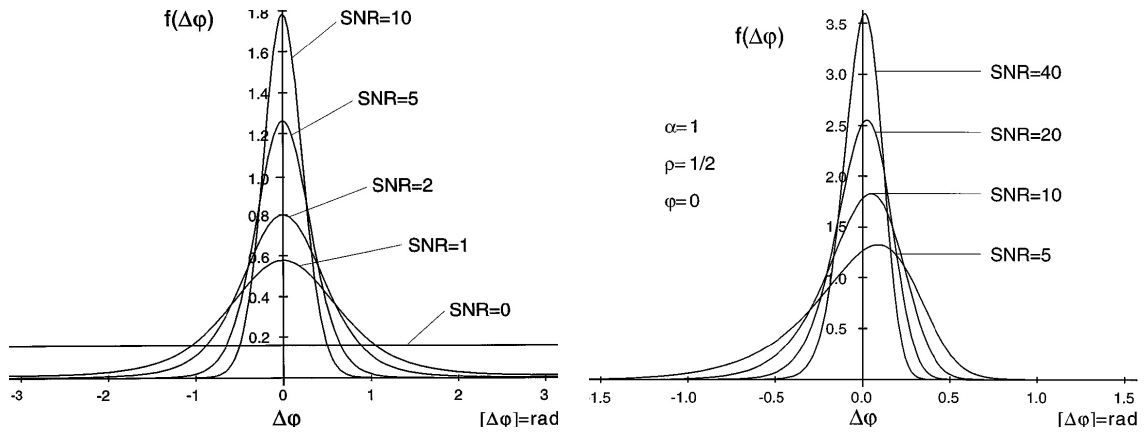


Figure 1.25: PDF of the phase error, proposed by Rathjen [7], for several values of SNR: uncorrelated case (left) and correlated case (right).

probability density functions (PDF) of phase error, could be derived according to different cases such as correlated or uncorrelated noise terms. Figure 1.24 shows the vector representation of the phase error, and the abscissa is the denominator part and the ordinate is the numerator part of the phase-shift algorithm respectively. Figure 1.25 shows the PDF of the phase error for several values of SNR: uncorrelated case (left) and correlated case (right).

If we model the noise in PMP scanning as additive and Gaussian, the absolute errors of phase and modulation are found they can be described by the PDFs used in magnetic resonance imaging (MRI). Gudbjartsson and Patz built such error models for phase and modulation distribution in MRI [8], as shown in Fig. 1.26 (left) and (right) respectively.

Li et al. proposed an additive white-noise model for PMP and they then applied the model to optimize a two-frequency PMP algorithm [9]. In Li et al.'s work, the variance of phase error was described as

$$\sigma_{\phi}^2 = \frac{2\sigma^2}{NB^2}, \quad (1.16)$$

where σ_{ϕ}^2 is the variance of phase error, σ^2 is the variance of the additive noise, N is the number of PMP patterns, and B is the fringe modulation. So Eq. (1.16) indicates the variance of phase error, σ_{ϕ}^2 , will be decreased if the number of patterns, N , and/or the fringe modulation, B , are/is increased. Figure 1.27 shows The variance of phase error

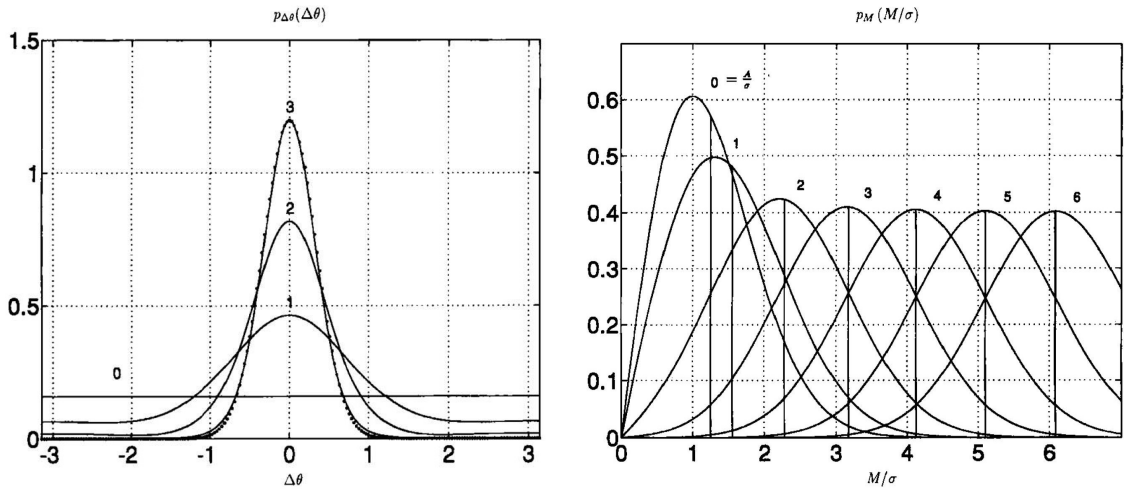


Figure 1.26: The phase error distribution (left) and modulation error distribution (right) in MRI proposed by Gudbjartsson and Patz [8].

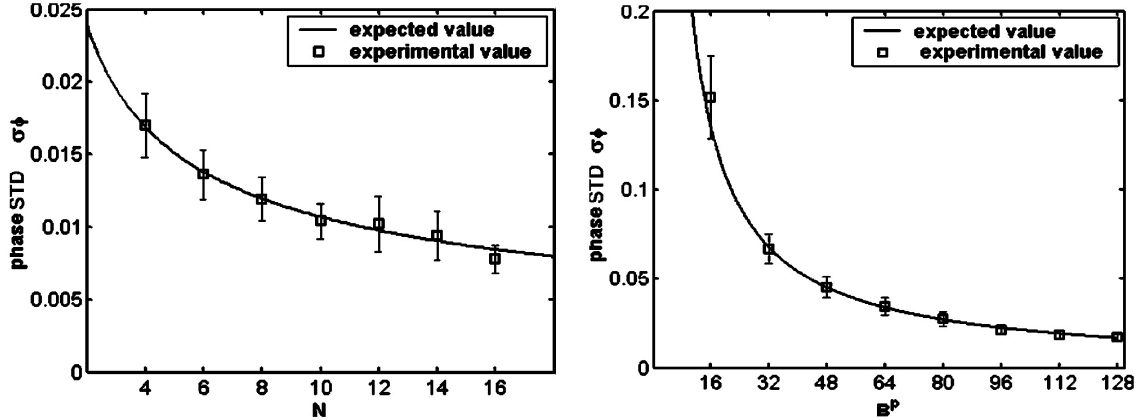


Figure 1.27: The variance of phase error versus the number of patterns (left) and the fringe modulation (right) proposed by Li et al. [9].

versus the number of patterns (left) and the fringe modulation (right) respectively. If high-frequency PMP patterns were involved, phase unwrapping needed to be taken. Once phase unwrapping was performed successfully, the variance of phase error would be reduced furthermore.

According to Li et al.'s noise model, typically there are three factors suppressing noise in scanning. The first factor is the number of patterns where more patterns lead to reduced noise. But for a real-time system, more patterns also means more processing. The second factor is the Signal-to-Noise-Ratio (SNR) between the light strength of the projected patterns versus the variance of sensor noise, where higher SNRs leads to lesser noise in the 3-D reconstructions. But for a fixed system, the projected signal strength is limited by the light source of the projector while sensor noise is inherent to the selected camera. The last factor is the frequency of projected pattern with higher pattern frequency leading to reduced noise in the 3-D reconstruction, but it also introduces ambiguities in the reconstruction process that needs to be dealt with by means of phase unwrapping [81].

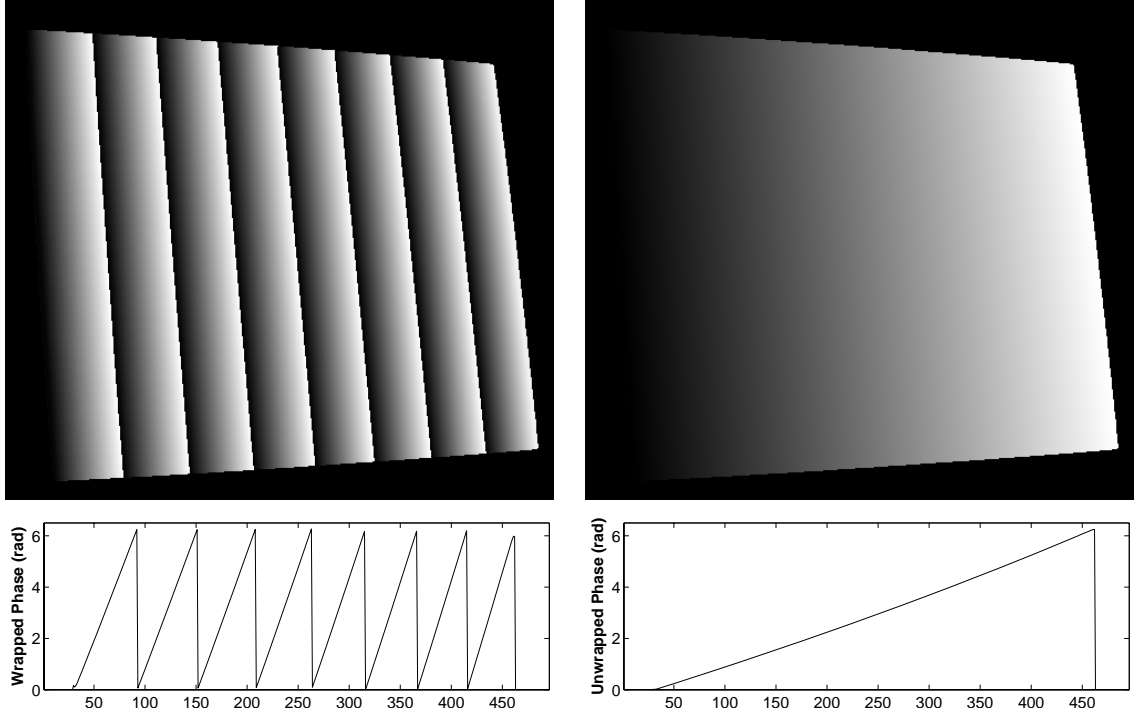


Figure 1.28: Visualizations of wrapped phase (top-left) and unwrapped phase (top-right) of a foam board, and curve plots of the cross-section of the wrapped phase image (bottom-left) and the unwrapped phase image (bottom-right).

Phase unwrapping is widely used in most interferometry-based methods [82], such as interferometric synthetic aperture radar and sonar (InSAR/InSAS) [83, 84], MRI [85], and optical interferometry [86]. As described by Surrrel [16], phase unwrapping means the 2π -jumps present in the data obtained after the phase detection process should be removed and the adequate multiple of 2π where necessary should be added. The mathematical description of phase unwrapping is [87]

$$\phi = \psi + 2k\pi, \quad (1.17)$$

where ϕ is the unwrapped phase, ψ is the wrapped phase, and k is an integer counting the number of 2π multiples. Figure 1.28 shows visualizations of wrapped phase (top-left) and unwrapped phase (top-right) of a foam board, and curve plots of the cross-

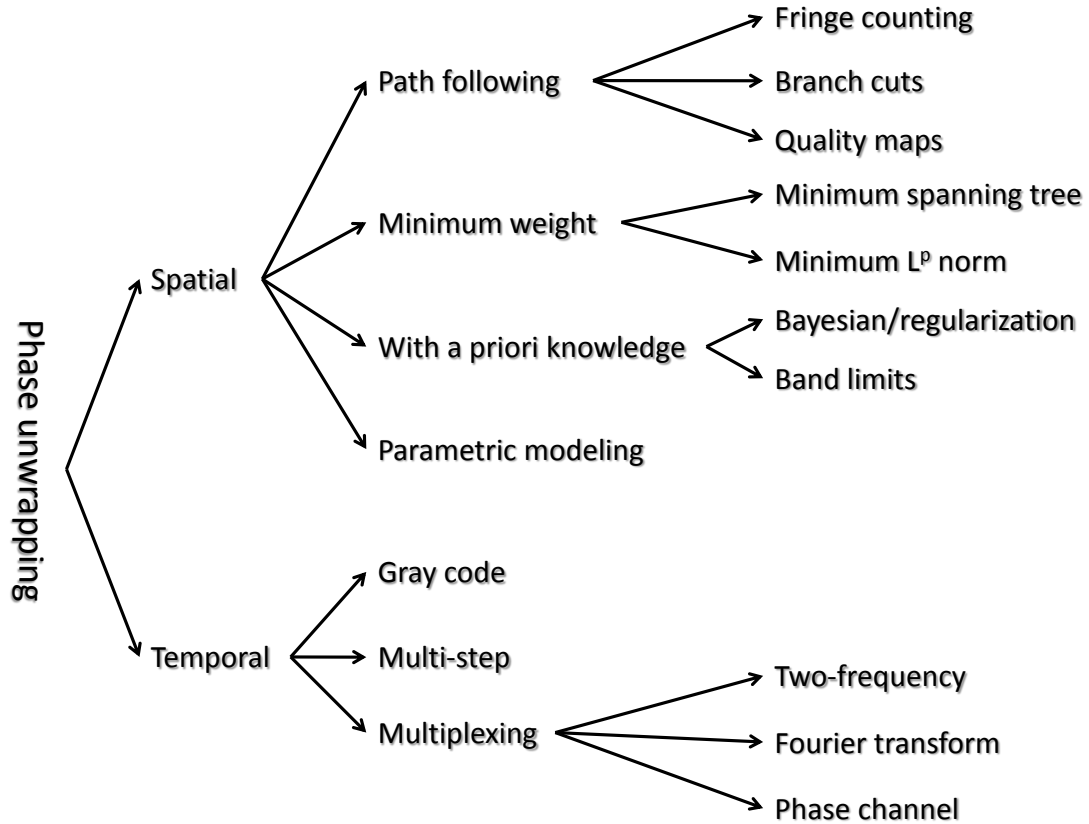


Figure 1.29: Taxonomy of phase unwrapping.

section of the wrapped phase image (bottom-left) and the unwrapped phase image (bottom-right).

For unwrapping phase, typically there are two principal strategies [88]: spatial [89,90,91,92] and temporal [9,93,94]. In spatial approaches, only a single wrapped phase map is employed and the unwrapped phase of a subject pixel is derived according to the phase values within a local neighborhood about the pixel. These methods have a tendency to fail in regions surrounding discontinuities in depth (step edges) [88]. Temporal methods use the intermediate phase values typically generated by projecting several additional unit-frequency patterns and, therefore, are not efficient for real-time operation. Based on the previous works of Judge and Bryanston-

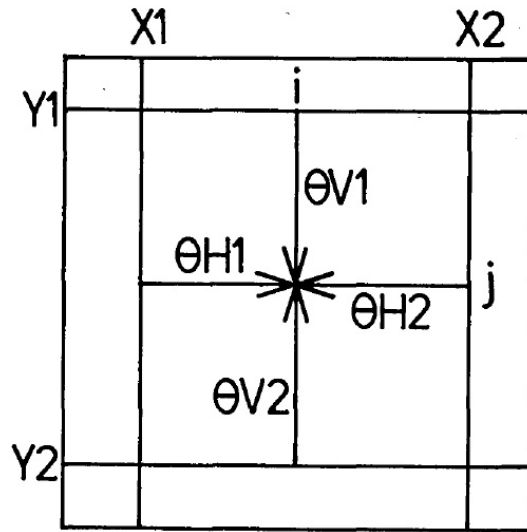


Figure 1.30: Schematic illustration of the phase fringe counting for spatial phase unwrapping proposed by Nakadate [10].

Cross [81], Surrel [16], and Bioucas-Dias and Valadao [87], a taxonomy of phase unwrapping is shown in Fig. 1.29.

A very simple idea for spatial phase unwrapping is phase fringe counting/scanning [81, 10]. First, the noise in phase data should be filtered; second, edge detecting is employed to find the phase jump; the number of multiples for unwrapping is obtained by counting the jumps along a scanning line; and finally the number of multiples will be applied to each point to unwrapped the wrapped phase into an absolute phase. Figure 1.30 shows this idea proposed by Nakadate and Saito. This method strongly relies on the quality of phase fringe edges and a good starting point.

Ghiglia et al. proposed a simple and mathematical cellular-automata method [11] to unwrap consistent phase data in one-, two- and n-dimensions. Noise-induced inconsistent phase data are taken care automatically through the automaton logic preventing the propagation of phase discontinuities. Aliasing-induced or natural phase

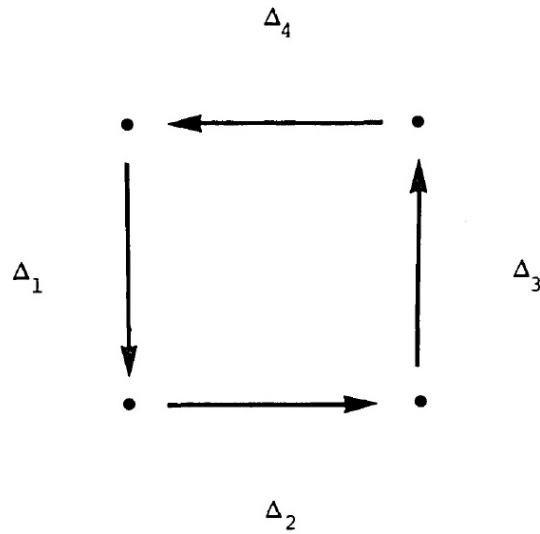


Figure 1.31: Graphical representation, checking for all 2×2 sample path inconsistencies, of the spatial phase unwrapping method proposed by Ghiglia et al. [11].

dislocations can be dealt with by region partitioning with a priori knowledge or by any partitioning which prevents phase unwrapping across inconsistent boundaries. So the cellular-automata method is naturally parallel and is independent to path. Figure 1.31 shows the graphical representation, checking for all 2×2 sample path inconsistencies, of the cellular-automata method proposed by Ghiglia et al.

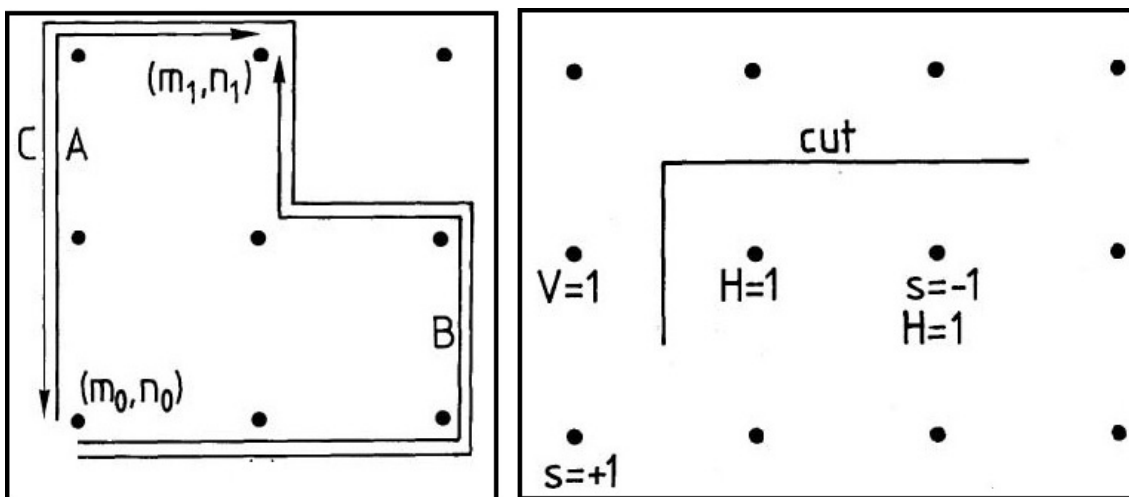


Figure 1.32: Graphical representation of the spatial phase unwrapping method proposed by Huntley [12]: basic requirement (left) and a cut example (right).

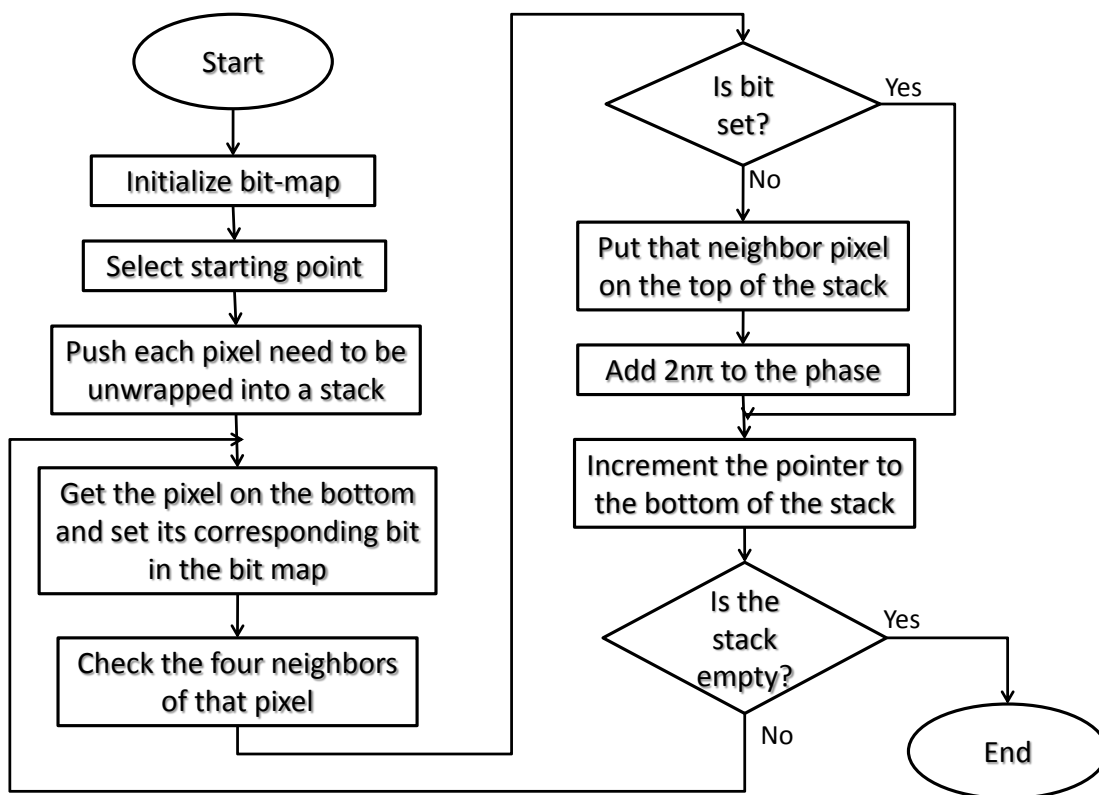


Figure 1.33: Work flow of the flood fill algorithm proposed by Bone.

Huntley proposed a noise-immune cut method for spatial phase unwrapping [12]. The goal of his algorithm is solving consistent phase maps with noise spikes. Huntley's algorithm requires that, given the phase at point (m_0, n_0) in Fig. 1.32 (left), there is a unique definition of the phase at any other pixel (m_1, n_1) in Fig. 1.32 (right), which is independent of the path for unwrapping, in the image. By placing cuts in the phase image, that requirement can be achieved. The cuts act as barriers to phase unwrapping. In the implement of the algorithm, two flag arrays, $H(m, n)$ and $V(m, n)$ are involved with initial value of zero. Once the process is done, the cuts information will be stored in the two arrays. A cut example is shown in Fig. 1.32 (right).

Bone proposed a flood fill algorithm for spatial phase unwrapping [95]. In that

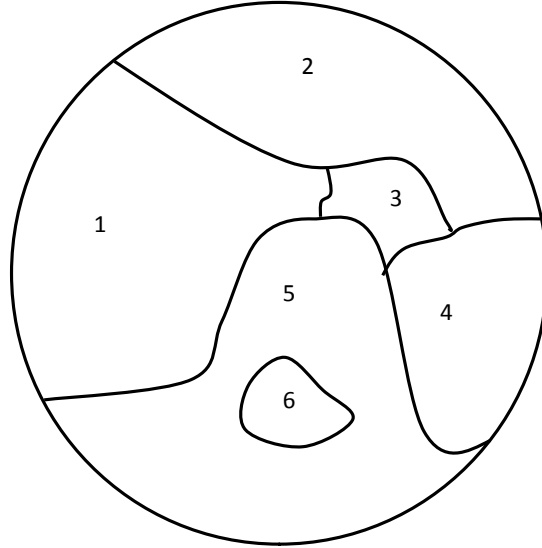


Figure 1.34: An example of circular field segmented into regions for the algorithm proposed by Gierloff.

algorithm, local phase information is employed to mask out the parts of the pixel which cause an inconsistent unwrapping. The flood fill algorithm is easy to implement and works fast and efficient. For the discontinuities and noise in the phase, the algorithm also is tolerant well. Figure 1.33 shows the work flow of the flood fill algorithm. If the regions needing to be unwrapped contain non-integer fringe shift across the discontinuity or the spatial frequencies either side of the discontinuity are significantly different, the algorithm will not be immune.

Differing from the previous spatial phase unwrapping algorithms, Gierloff proposed a regions based algorithm [96]. By dividing the fringe field into inconsistent regions, as shown in Fig. 1.34, the algorithm builds the relationship among those regions each other. For large scale discontinuities, the algorithm works well. Regions are segmented by checking whether pixels are in a tolerance of adjacent pixels already included. If all pixels have been processed, the regions' edges will be compared

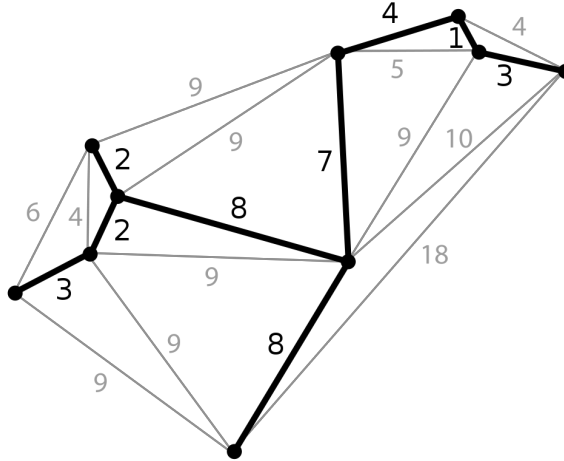


Figure 1.35: Labeled with weight, a minimum spanning tree of a planar graph (from http://en.wikipedia.org/wiki/Minimum_spanning_tree)

in order to find whether there exists a discontinuity between them. Once all edges between adjacent regions have been tested, the points of edge will be compared in order to see whether a phase shift is needed. The shortcomings of this method are: first, it can not guarantee path independence; second, it flaws the weighting criterion for connecting regions together; and finally, as stated by Gierloff, it did not perform perfectly.

Based on minimizing phase changes between pixels with minimum spanning tree (MST), as shown in Fig. 1.35, Judge et al. proposed an algorithm which was claimed to be tolerant of noise [97]. A MST is a minimal weighted subgraph connecting all the vertices in a graph. There are two levels for phase unwrapping with MST: the low level covers all the procedures which are required to perform phase unwrapping pixel to pixel; and high level assembles each unwrapped phase component into an entire phase field solution by means of some weighting strategies. The issue of discontinuities is still a significant challenge for this kind of algorithm.

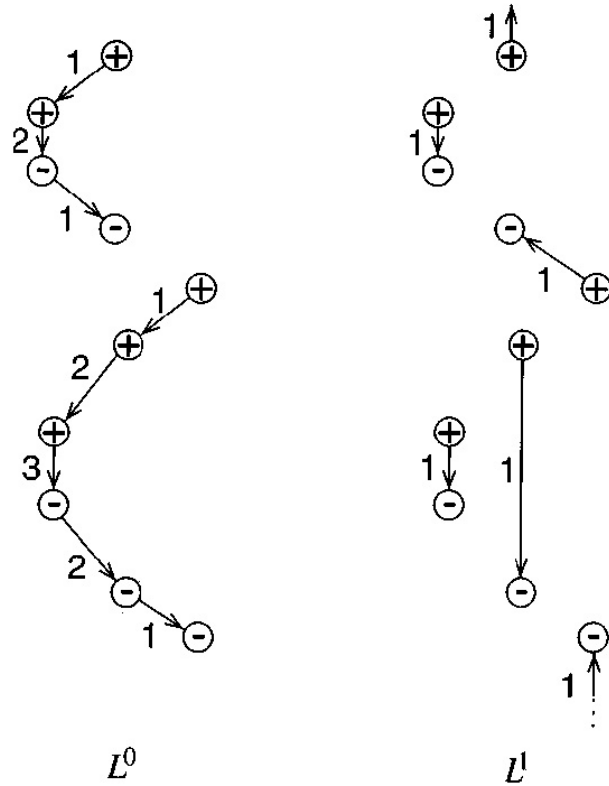


Figure 1.36: Minimization of L^0 (left) and L^1 algorithms proposed by Chen and Zebker [13].

Minimum norm approaches attempt to solve phase unwrapping by minimizing the L^p norm of the difference between the wrapped phase differences and the absolute phase differences. The value of p can be 0, 1, 2, and in the range of $(0, 1)$ [87]. L^2 norm is equivalent to a least squares method (LSM) [98, 99]. The drawback of L^2 norm-based methods is a tendency to smoothing discontinuities. Flynn solved that problem with an L^1 norm algorithm [100]. L^0 norm is desirable in practice, but minimizing it will lead to an NP-hard problem. An approximate solution for L^0 norm has been proposed by Chen and Zebker [13, 101]. If $p \in (0, 1)$, highly complicated algorithms should be employed to solve the minimization of L^p norm [101].

Taking advantage of the knowledge of the frequency band limits of a wrapped

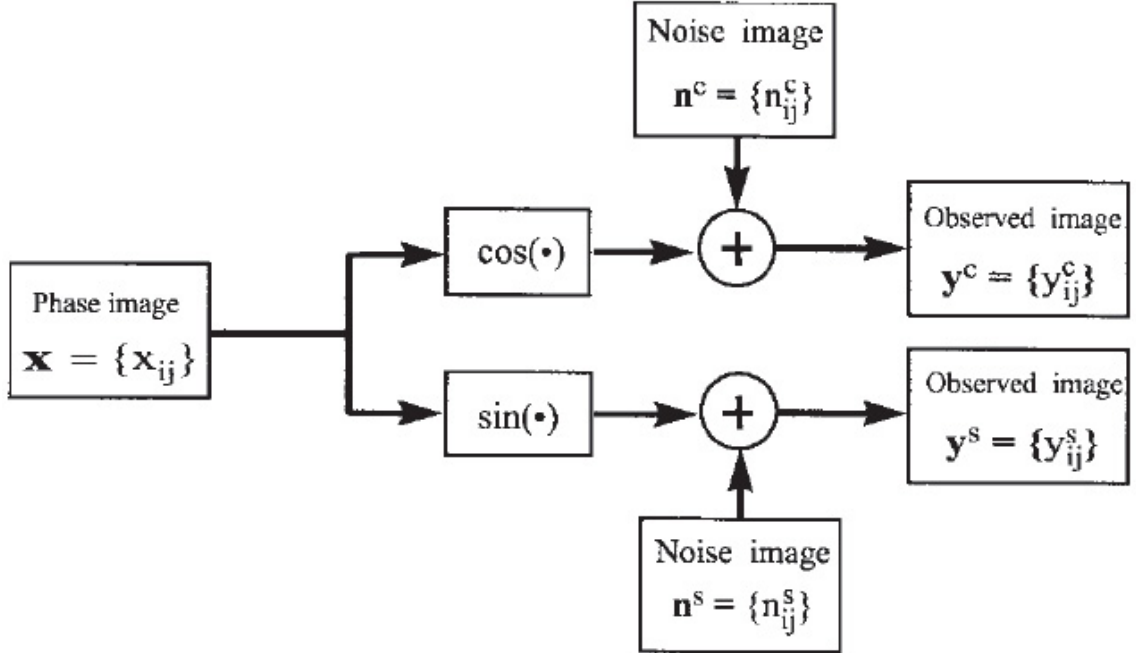


Figure 1.37: Bayesian algorithms proposed by Leitao and Figueiredo [14].

phase map, Green and Walker presented their spatial phase unwrapping algorithm which was helpful to large scale phase discontinuities [102]. If a phase function is wrapped, there is a modulo 2π or 2π -jump. When a frequency-band-limited phase function is wrapped, the spectrum of the resulting function can be extended beyond the bandlimits. With rewriting the bandlimited phase function and taking Fourier Transform as well as other corresponding operations, phase unwrapping can be achieved and is noise-immune. Bayesian methods are another a priori knowledge based phase unwrapping. Bayesian approach depends on a model of data-observation mechanism of the phase. Leitao and Figueiredo employed a nonlinear filter to optimize phase unwrapping [14]. Dias and Leitao proposed another InSAR observation model by involving the image phase, the backscattering coefficient image and correlation factor image [103].

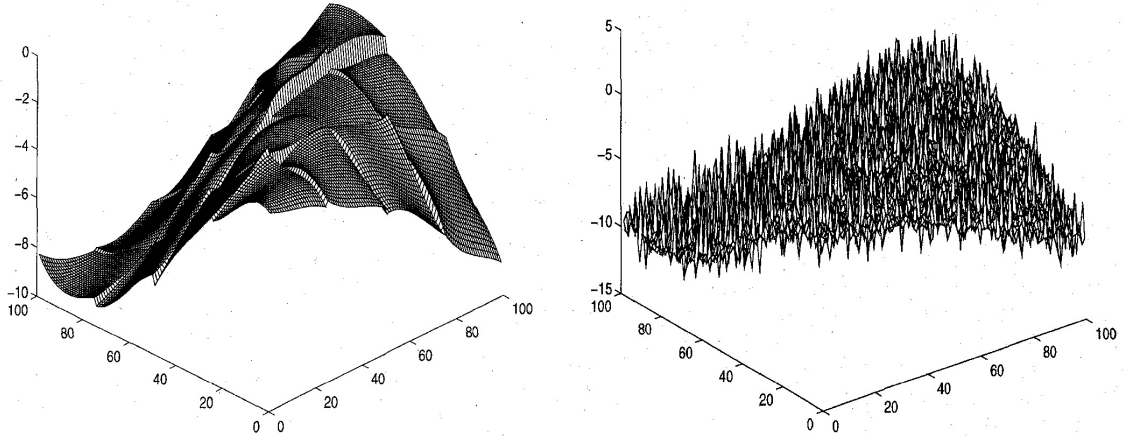


Figure 1.38: Parametric algorithms proposed by Friedlander and Francos [15].

Friedlander and Francos proposed a parametric algorithm for spatial phase unwrapping by constraining the unwrapped phase to a parametric surface [15]. In practice, a complete surface can not be modeled accurately with only one polynomial. To solve such problem, the algorithm employs low-order polynomial surface and segments phase image with different parametric models.

Contrast to spatial approaches, the advantages of temporal phase unwrapping methods are [104]: first, the principle and implement is easy and simple; second, phase errors are bounded within the high-noise regions and will not propagate to other regions; and finally, discontinuities will not be an considerable issue anymore.

Some commercial SLI scanners employ gray code to achieve phase unwrapping robustly [16]. In this method, the wrapped phase fringe order will be determined by a serial gray code patterns. The total number of the gray code patterns is

$$N_{gray} = \text{floor}[\log_2 F] + 1, \quad (1.18)$$

where F is the number of fringes in the phase map, and floor is the function to

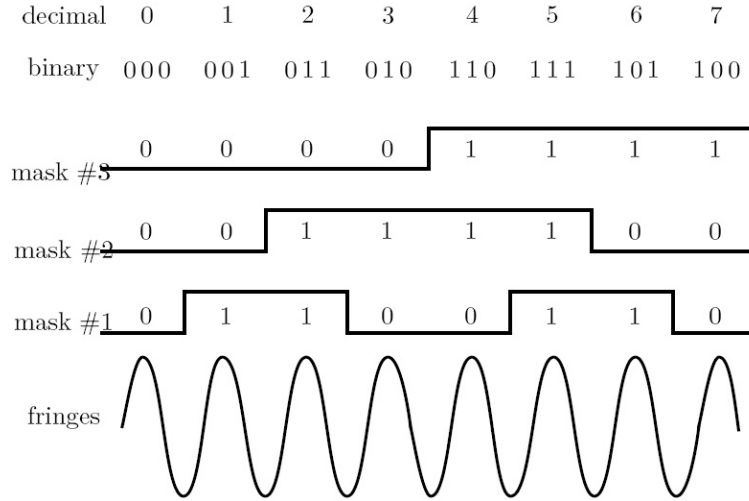


Figure 1.39: Gray code temporal phase unwrapping algorithms proposed by Surrel [16].

extract the integer part of a number. Figure 1.39 shows the procedure of gray code based temporal phase unwrapping.

In multi-step temporal methods, typically high-frequency patterns differ low- or unit-frequency patterns only from frequency [104, 9, 50]. The phase obtains from low- or unit-frequency patterns is noised and acts as a reference information for unwrapping the wrapped high-quality phase. The procedure of this kind of method is shown in Fig. 1.40. The example of phase unwrapping in Fig. 1.28 was also based multi-step approach.

Either gray code or multi-step temporal phase unwrapping algorithms need some additional patterns to generate one or more intermediate phase helping phase unwrapping, so in some situations such as real-time scanning requirement, those temporal methods are not efficient. Many researchers attempted to solve that problem by multiplexing.

Takeda [17] proposed a frequency-multiplex Fourier-transform profilometry (FMFTP)

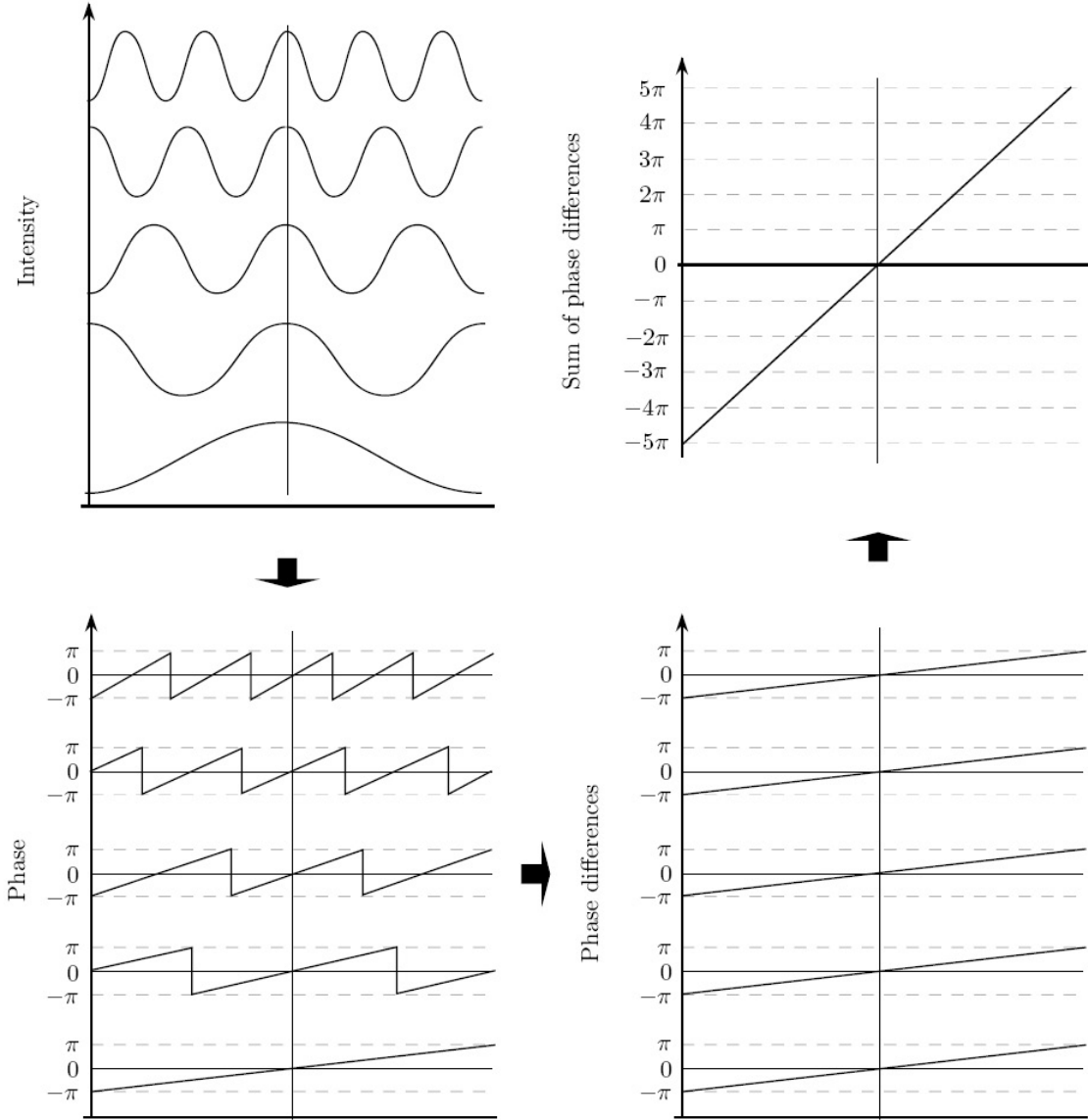


Figure 1.40: Multi-step temporal phase unwrapping [16].

which, based on the FTP method [53], modulated several different-frequency patterns into to single pattern. After camera captured a patterned image, demodulation was taken by spatial Fourier Transform method. Then several patterned images could be extracted and dealt with multi-step method to achieve phase unwrapping. Figure 1.41 shows the multiplexed spectra in the spatial frequency domain of the FMFTP algorithm.

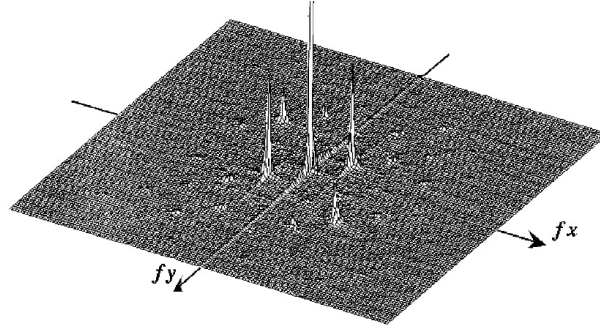


Figure 1.41: Multiplexed spectra in the spatial frequency domain of the algorithm proposed by Takeda et al. [17].

Li et al. [105] proposed a two-frequency pattern strategy which integrates both high-frequency and unit-frequency into one pattern, but $2N$ ($N \geq 3$) patterns were needed and the high frequency must be equal to N . Two equations are needed to

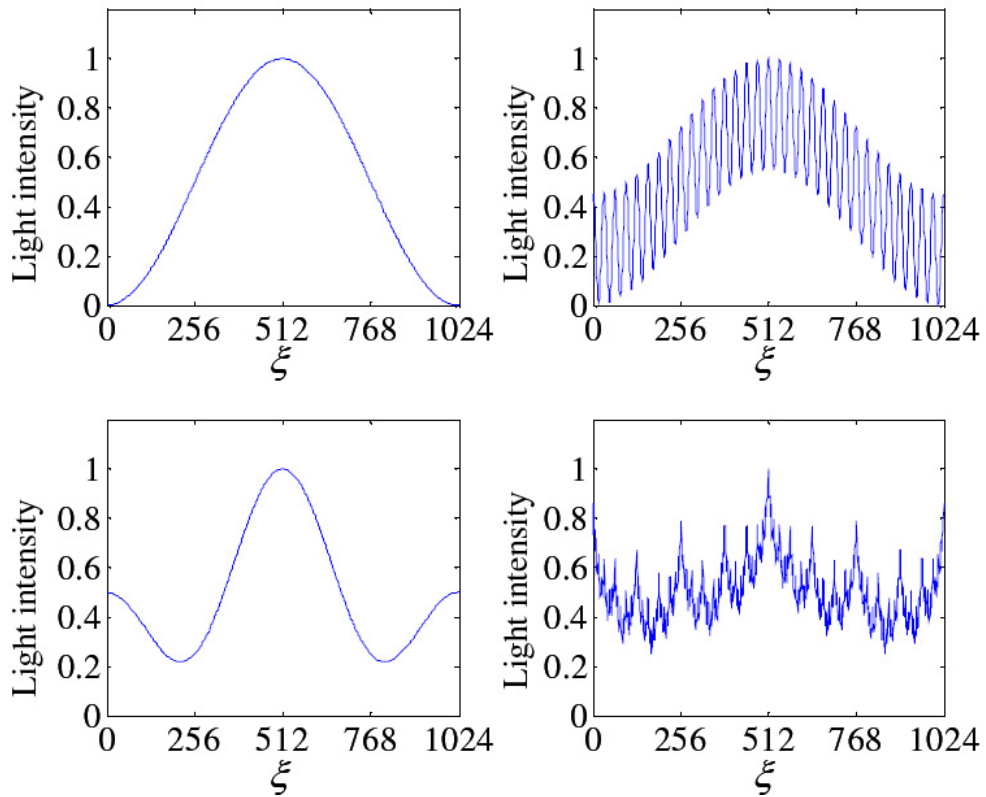


Figure 1.42: Composite multi-frequency sinusoidal fringe pattern proposed by Kim et al. [18].

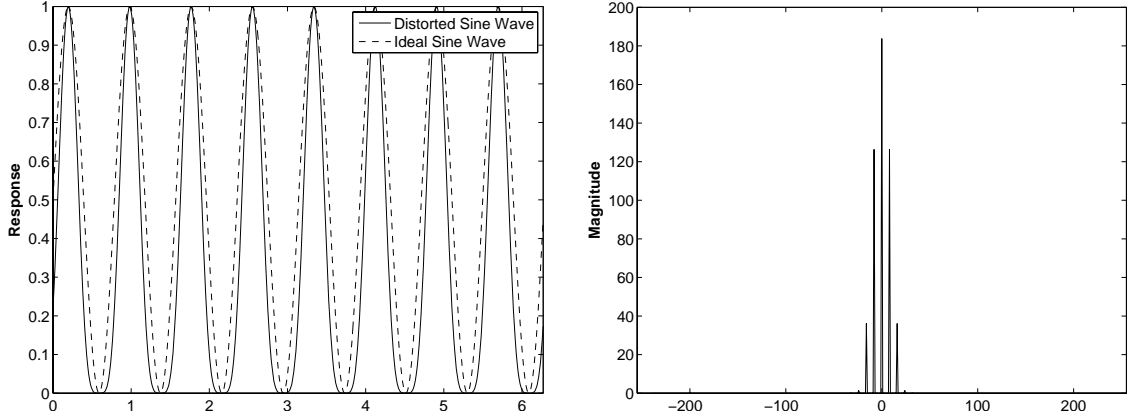


Figure 1.43: Ideal and distorted ($\gamma = 2.2$) sine wave (left), and the magnitude of the distorted sine wave in the frequency domain (right).

describe the two groups of coding strategy. Separately, Kim et al. [18] proposed a composite multi-frequency sinusoidal fringe algorithm without phase unwrapping but did so requiring $4N$ ($N \geq 2$) patterns. Figure 1.42 shows Kim et al.’s pattern strategy.

Gamma Distortion

While the effects of gamma distortion diminish with an increasing number of employed phase-shifted patterns, gamma distortion may be unavoidable in real time systems where the number of projected patterns is limited by the presence of target motion. Gamma distortion [106, 107, 108] makes ideal sinusoidal waveforms non-sinusoidal, as illustrated in Fig. 1.43 (left), such that the resulting distortion is phase dependent. Figure 1.43 (right) shows the magnitude of the distorted sine wave in the frequency domain where the highest pulse is the direct component (DC) while the second highest pulse is the first-order harmonic, which is the phase component used in PMP.

Under ideal conditions, the DC and first-order harmonic are the only non-zero



Figure 1.44: The visualization of magnitude of harmonics: (left) first order, (middle) second order, and (right) third order.

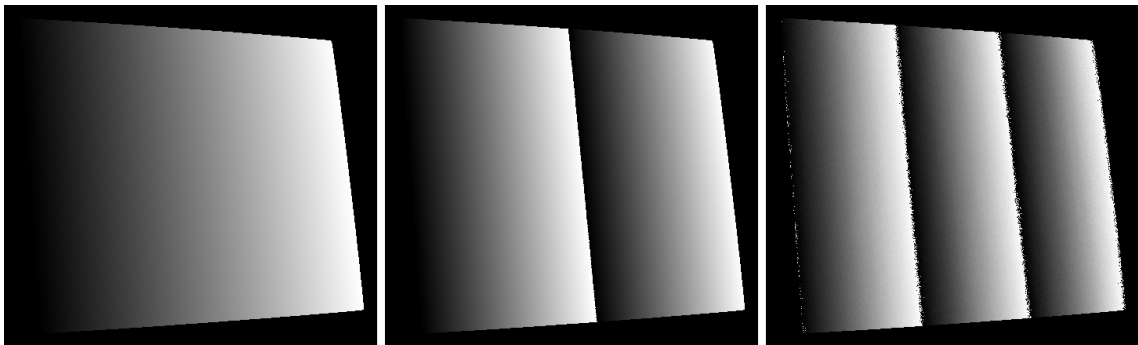


Figure 1.45: The visualization of phase of harmonics: (left) first order, (middle) second order, and (right) third order.

components, but if there exists gamma distortion, higher-order harmonics will appear. In Fig. 1.43 (right), there are higher order harmonics including a fourth and fifth components, that although not visible in the figure, are significant. Employing a sufficiently large number of component patterns, one can disperse this error over the many patterns such that its effects are minimized, but where only a few patterns are employed, the effects of gamma distortion can be significant. Scanning of a white foam board with three PMP unit-frequency patterns, Fig. 1.44 shows the visualization of magnitude of harmonics of 1st, 2nd and 3rd order respectively and Fig. 1.45 shows the visualization of phase of harmonics of 1st, 2nd and 3rd order respectively.

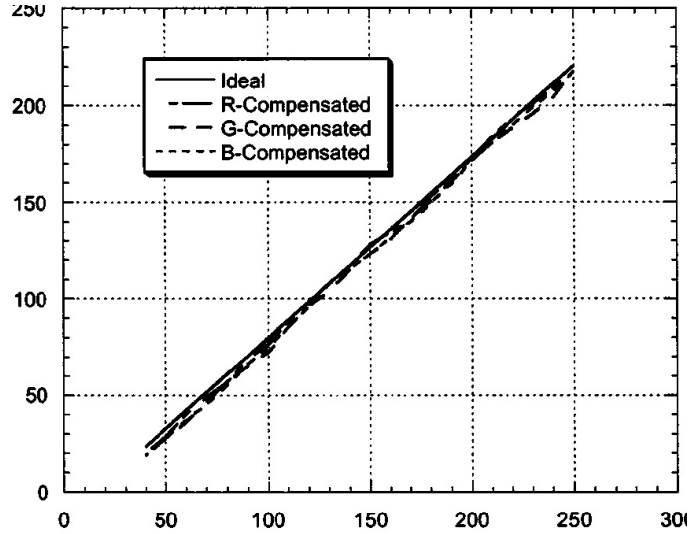


Figure 1.46: pre-compensating non-linearity proposed by Huang et al. [19].

In order to address the effects of gamma on PMP, Huang et al. [19] corrected for gamma distortion by applying tone correction to the SLI patterns before being projected, and the pre-compensation of non-linearity proposed by Huang et al. is shown in Fig. 1.46. But by doing so, as Zhang and Yau pointed out [26], the residual error was still non-negligible. Alternatively, Su et al. [48] defocused their projector to act as a low-pass filter to process square waveforms using the PMP algorithm. Baker et al. [20] followed this technique to deal directly with gamma distortion by defocusing his projector too. Both of these authors expressed the harmonic components by means of an infinite Fourier Series, and filtered out the high order harmonic waveforms directly using the defocus feature without additional computation for correction or compensation, but the improvement was at the cost of diminishing Signal-to-Noise Ratio (SNR) and, for three-step PMP with $\gamma = 3$, the improvement was only $2\times$. The experiments results of Baker et al.'s method is shown in Fig. 1.47.

Alternatively, Hibino et al. [109] eliminated the effects of harmonic components of

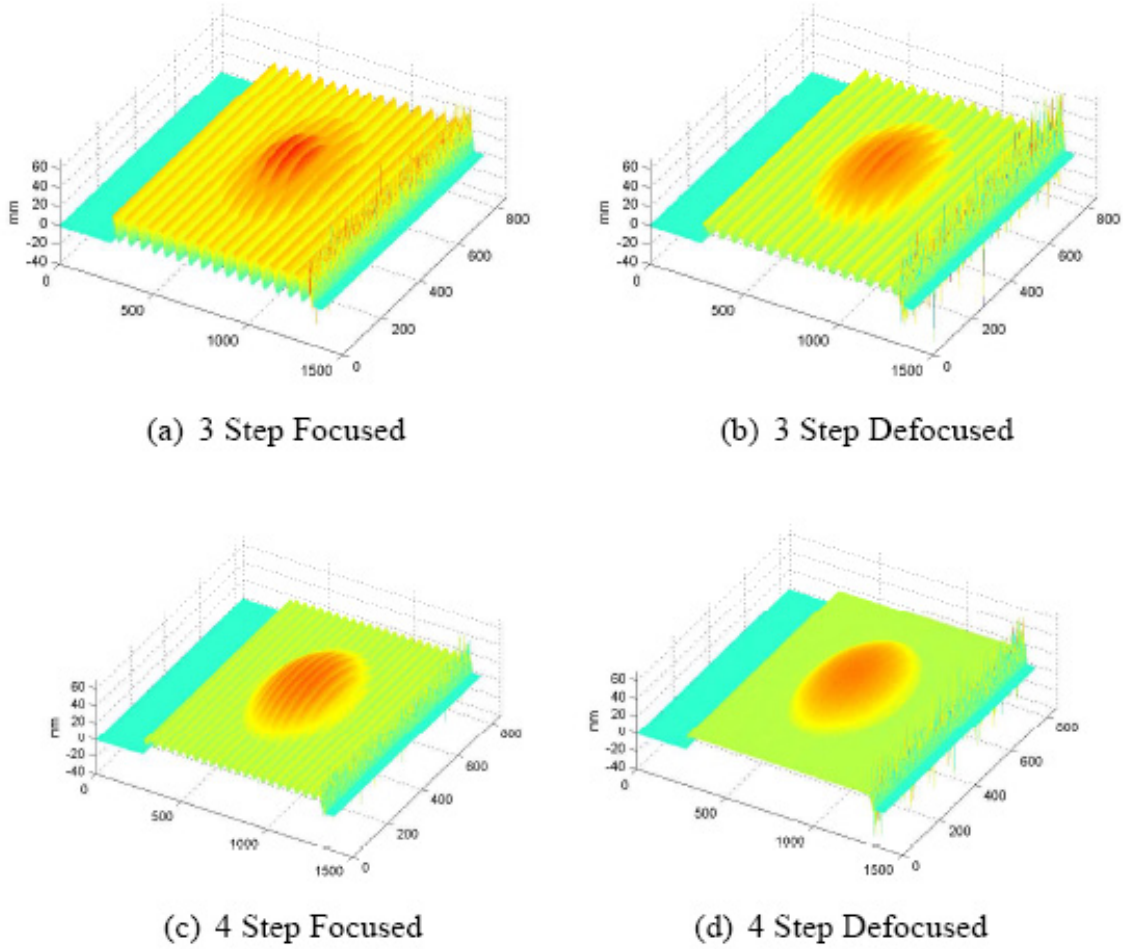


Figure 1.47: Eliminating gamma effects by defocusing projector proposed by Baker et al. [20].

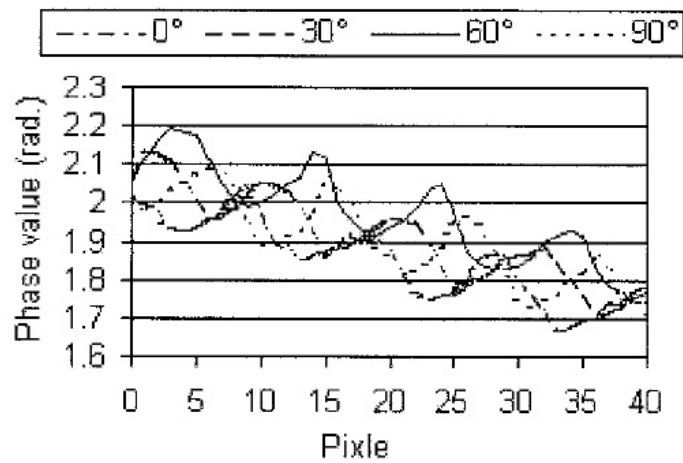


Figure 1.48: Eliminating gamma effects proposed by Huang et al. [21].

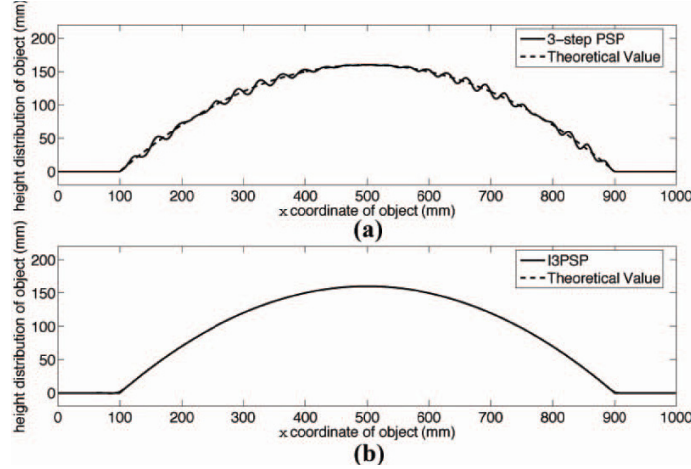


Figure 1.49: Eliminating gamma effects proposed by Hu et al. [22].

the signal and a constant phase-shift error at a cost of requiring at least 5 projected patterns. Similarly, Huang et al. [21] employed six patterns, called double three-step phase-shifting, to obtain two distorted phases with contrary distortion direction and averaged them to cancel the distortion. An experimental result of Huang et al. is shown in Fig. 1.48. Hu et al. [22] applied lowpass filtering to remove high-order harmonics in simulation but provided no experimental results, and a simulation result is shown in Fig. 1.49. Hu et al. [23] also developed a gradient-based shift estimation (GSE) method for gamma that included the second harmonic effect, and an experimental result is shown in Fig. 1.50. Surrel [110] expressed harmonics in polynomial form but needed at least 6 patterns to eliminate the effects of higher-order harmonics. Baker et al. [24] took advantage of the generalization and interpolation of neural network to achieve an improvement of 80% indicated by their simulation, and an experimental result is shown in Fig. 1.51.

Zhang and Huang [25] proposed a LUT-based approach to compensate the phase error directly without employing any mathematical gamma model, and an experi-

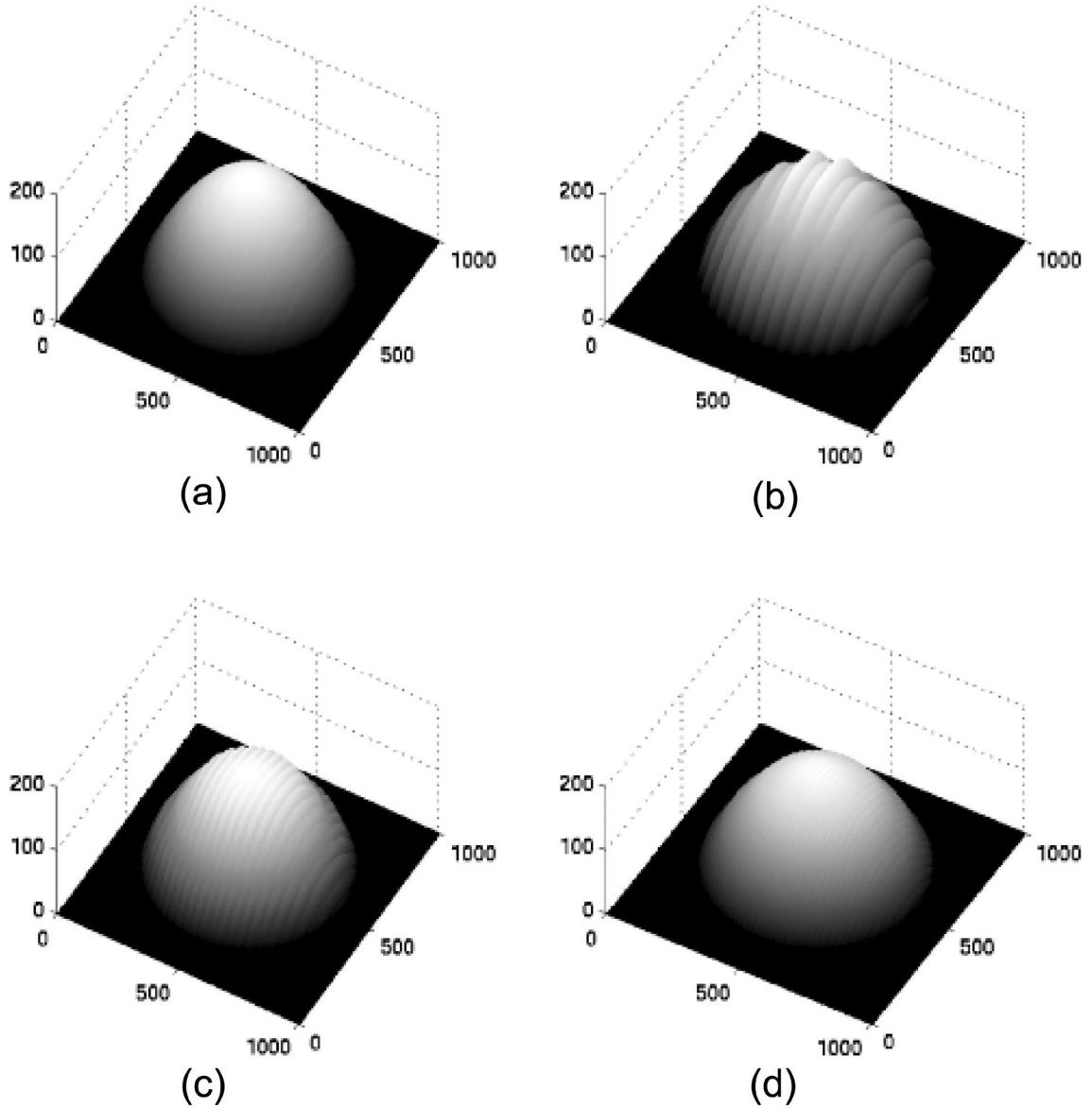


Figure 1.50: Eliminating gamma effects proposed by Hu et al. [23].

mental result is shown in Fig. 1.52. While this method is greatly suitable for non-analytical situations, Zhang employed the concept of gamma, which is an analytical issue. The method of gamma calibration in that paper was traditional and unstable because only the gamma at the center of the projected image was computed. The accuracy of phase compensation depended on the length of LUT because the mea-

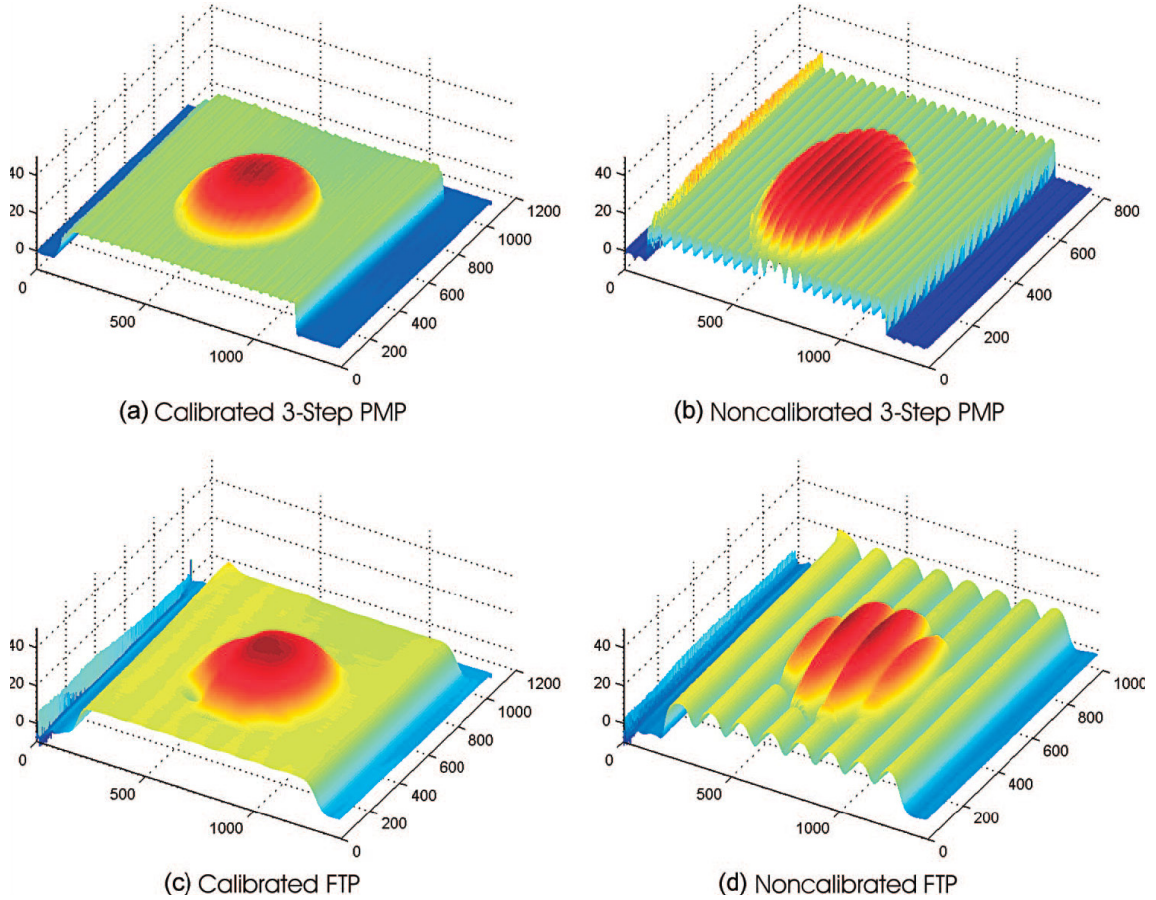


Figure 1.51: Eliminating gamma effects proposed by Baker et al. [24].

sured phase was real-type data involving interpolation. Zhang and Yau [26] presented another LUT-based phase compensation algorithm without pre-computing gamma directly that was also suitable for other phase-shifting-based measuring, and an experimental result is shown in Fig. 1.53. However, Zhang’s second LUT algorithm could not avoid acquiring reference information of gamma distortion before scanning, and the results of phase correction was also dependent on the length of the LUT. According to his paper, the improvement using the second method was only the half that of the first. Jia *et al.* [111] was motivated by Zhang [25] and also proposed a LUT-based compensation algorithm for their two-step, triangulation pattern, which

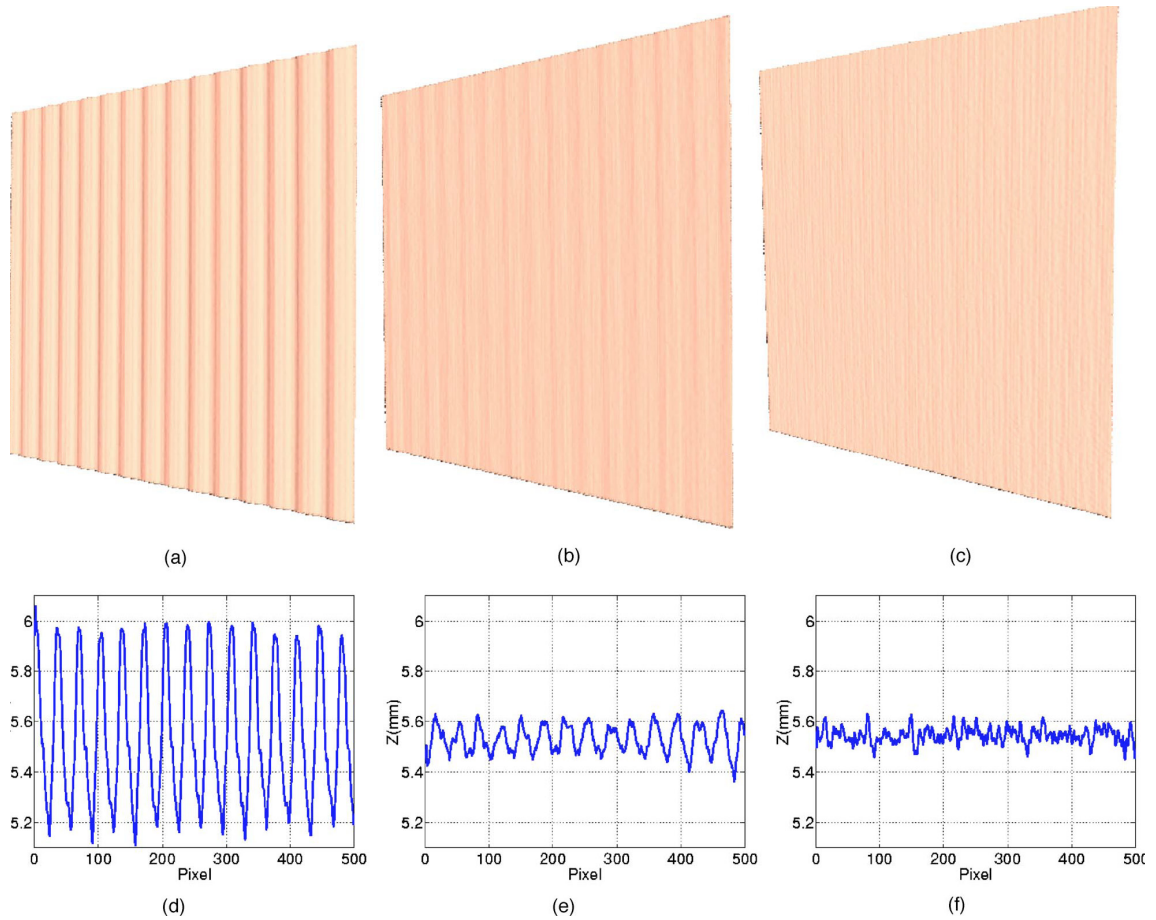


Figure 1.52: Eliminating gamma effects proposed by Zhang et al. [25].

worked well when neither ambient light nor object texture were considered.

Guo et al. [27] employed statistical methods to analyze and correct for gamma distortion by framing gamma distortion as an uncertainty problem. In Guo et al.'s experiment, as shown in Fig. 1.54, high-frequency four-step PMP was adopted for a gamma value of 1.4802, which was not a particularly challenging problem. Pan et al. [28] proposed approach suffered from an inaccuracy gamma calibration and had to employ an approximate and simplified one-order equation, and an experimental results is shown in Fig. 1.55. This is the short-coming of many of these prior works to rely on simple, second-order, gamma models or on complicated calibration procedures

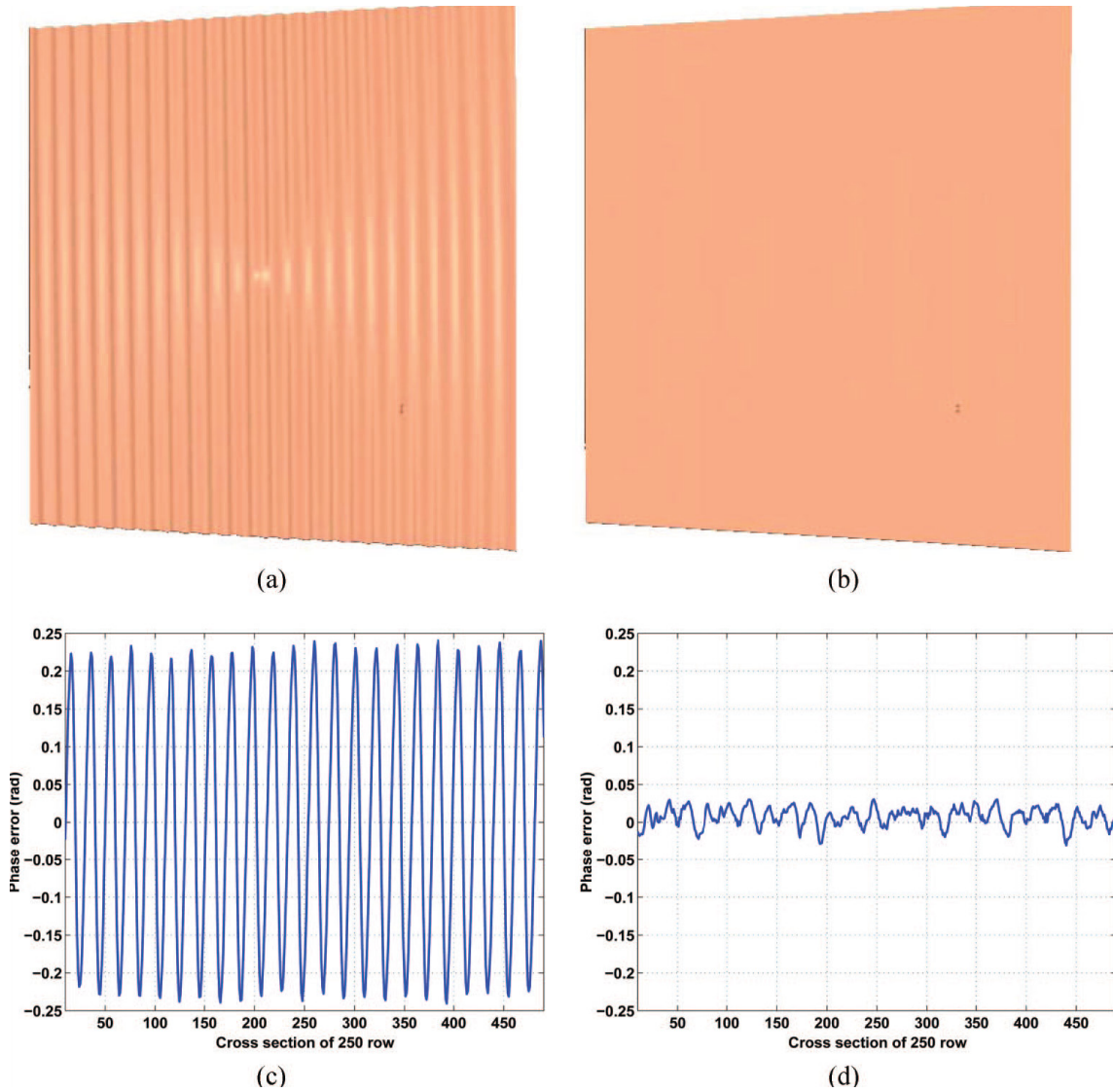


Figure 1.53: Eliminating gamma effects proposed by Zhang et al. [26].

when, as will be shown in this dissertation, having an accurate model, for predicting the effects of gamma distortion on PMP, allows one to avail themselves of the pre-calibration procedure and to measure phase more accurately.

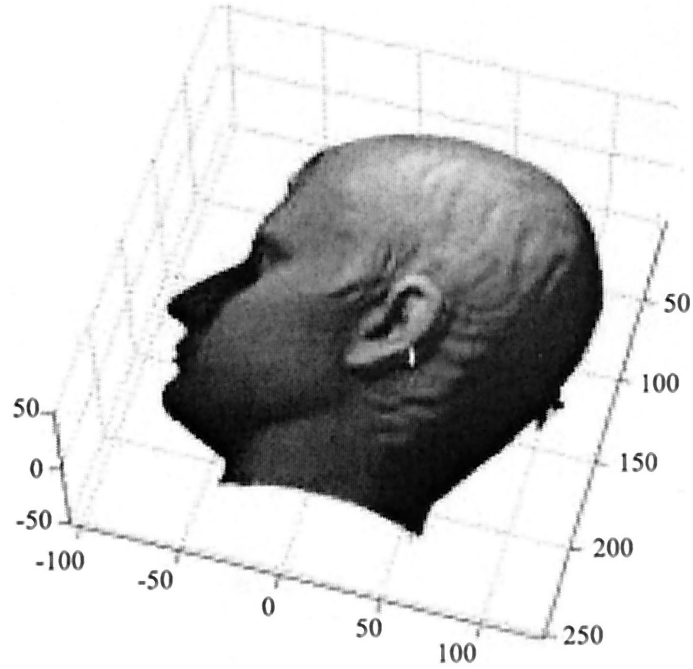


Figure 1.54: Eliminating gamma effects proposed by Guo et al. [27].

1.3 Contributions of this Dissertation

Now although many approaches to 3-D reconstruction have been proposed that claim to operate in real time, each study has proposed varying definitions of what con-

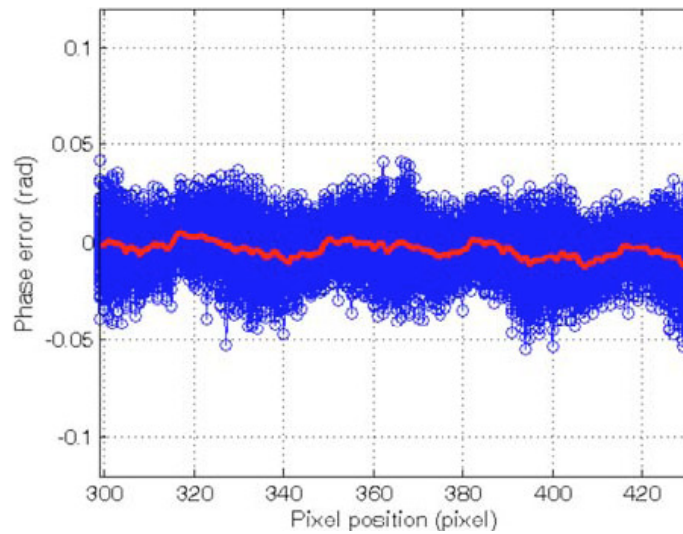


Figure 1.55: Eliminating gamma effects proposed by Pan et al. [28].

stitutes real-time operation. Actually there are four stages to real-time 3-D reconstruction. First, data should be acquired in real time; second, generating the phase or finding the correspondence between camera and projector should be performed in real time, which is very difficult for many pattern schemes such as frequency multiplexing and neighborhood coding one-shot SLI pattern schemes; third, 3-D point clouds should be reconstructed in real time by using either phase-to-height conversion or absolute 3-D coordinates computation, which is the bottle neck for most proposed strategies; and finally, the reconstructed 3-D point clouds should be displayed in real time. Because none of the methods reviewed so far achieve real-time operation for all four stages of SLI, we classify them as, “Fast SLI,” but in this dissertation, a novel SLI system satisfying all four of these real-time stages will be demonstrated [29].

Because our proposed real-time system relies, like similar multi-pattern techniques, on minimizing the number of component patterns in order to minimize the effects of target motion, we further introduce a novel pattern scheme that attempts to limit the effects of sensor noise on the resulting 3-D point clouds, we further developed a novel strategy that employs a high-frequency sinusoidal grating that, during modulation, produces an additive-noise-suppressed, high-quality, wrapped phase signal. Embedded with this high-frequency sinusoid is a unit-frequency sinusoid whose coarse unit-frequency signal is used during demodulation to produce an instantly decodable, unwrapped-phase term temporally such that the process of unwrapping the higher frequency phase spatially is avoided.

Finally in light of the effect of gamma distortion, this dissertation looks to introduce a gamma model from which we can compensate the phase error caused by

non-unitary gamma on PMP. At the same time, with such a detailed and accurate gamma model, an accurate gamma calibration method is derived, and two strategies for minimizing gamma's effect on phase determination are presented. These phase correction strategies include phase corrections with and without gamma calibration.

Real-time SLI

To achieve real-time 3-D video acquisition and reconstruction, Chapter 2 of this dissertation introduces a lossless look-up table (LUT) method for real-time phase, intensity/texture, and depth video that works in combination with a high-speed projector/camera pair employing the widely used SLI technique of PMP. While LUT-based methods have been known for the low computational cost and have been employed in many applications for various purposes [112, 113], we introduce a novel processing method that extracts phase and intensity/texture information from the incoming PMP video as a means of reducing the computational complexity of the arctangent and square-root functions.

The intensity/texture information is used for the purpose of segmenting out background clutter as well as for texture encoding the final point cloud. Furthermore since no LUT-based method has so far been introduced for inverting the camera's calibration matrix in combination with the phase video to produce a 3-D point cloud in real time, we introduce such a method that can also be applied to other triangulation-based 3-D reconstruction techniques.

Divided across threads, the first thread is for grabbing images from the camera; the second thread generates the phase map; the third thread computes the absolute

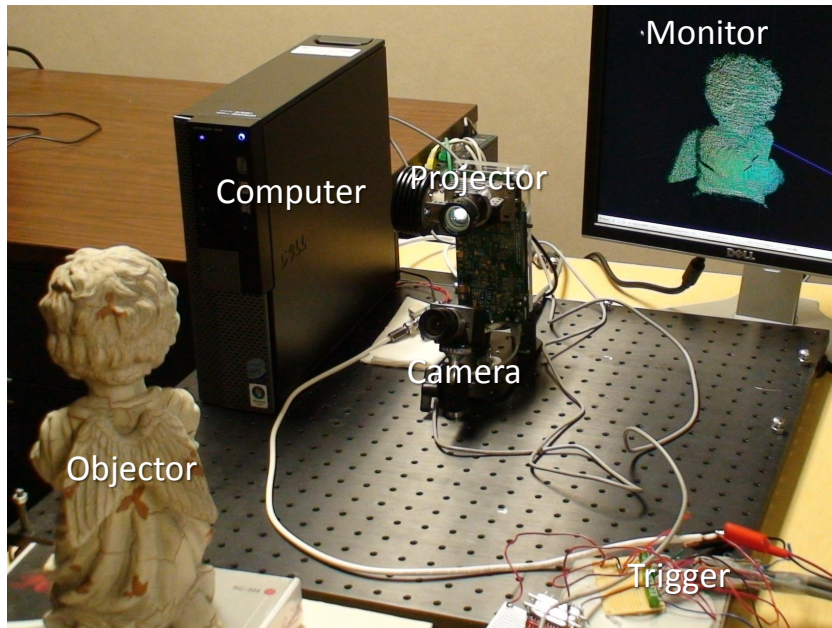


Figure 1.56: A real-time 3-D measurement system developed by Liu et al. [29] in 2010.

3-D coordinates; and finally, the fourth threads displays the measured 3-D data in real time. For deriving phase, we take advantage of the fixed bit depth of the camera sensor by building a LUT instead of employing a time-consuming arctangent process. For deriving the absolute 3-D coordinates from the phase information, we eliminated the matrix inverse and multiplication by expanded them into a complex form that can be divided into two separate parts containing static information about the camera calibration, in one part, and dynamic phase information, in the second. As such, the first part can be pre-computed to form seven LUTs and whose output is combined with the phase information using 1 division, 4 multiplications and 4 additions to produce absolute 3-D point clouds. At no point does the use of LUTs reduce the accuracy of the calculations since we have one LUT entry for each and every possible bit combination of input pixel values.

As will be demonstrated in this dissertation, our experimental system achieves a processing rate of 714.29 fps to generate phase+texture video and 228.83 fps to produce 3-D point clouds using just one core of an Intel Core 2 Duo Quad Q9650 processor running at 3.0 GHz. No additional processing through added cores or even GPU processing is needed, but using such resources would, of course, increase our frame rate if necessary. Figure 1.56 shows our experimental setup.

Additive Noise

In order to limit the effects of sensor noise on the resulting 3-D point clouds, we developed a novel strategy, in Chapter 3, that employs a high-frequency sinusoidal grating that, during modulation, produces an additive-noise-suppressed, high-quality, wrapped phase signal. Embedded with this high-frequency sinusoid is a unit-frequency sinusoid whose coarse unit-frequency signal is used during demodulation to temporally produce an instantly decodable, unwrapped-phase term such that the process of spatially unwrapping the higher frequency phase is avoided. Traditional phase-unwrapping would make the differentiation of two discontinuous objects, in absolute space, impossible [104].

According to Eq. (1.2), the minimum number of patterns is 3, because there are three unknown parameters in the equation [114]. If we employ temporal method based on PMP, at least 6 patterns should be involved, i.e., 3 high-frequency patterns and 3 unit-frequency patterns. Reported by Li et al., there two-frequency grating also need 6 patterns at least. In this dissertation, a group of novel pattern schemes are proposed based on multiplexing phase channels according to the number of patterns, i.e., $N = 3$,

4, and 5 respectively. For $N = 3$, the DC channel is used to embedded a reference signal; for $N = 4$, the half phase channel is utilized to contain the reference signal; and for $N = 5$, the second full phase channel will be employed to contain the reference signal. All these three coding strategies are called phase channel multiplexing pattern (PCMP) strategy. Although the proposed algorithms are also suited for $N > 5$, we only consider the cases, i.e., $N = 3, 4$, and 5 , which can not be handled by traditional 3+3 two-frequency PMP or Li et al.' two-frequency grating.

Before the proposed PCMP is introduced, traditional PMP equations are rewritten with new forms. The parameters in the new equations can clearly describe the phenomena appeared a PMP scanning, and those parameters are analyzed carefully as well as the solutions for them are provided. With the new equation forms, an additive noise model is built for PMP. Each absolute errors of parameters are derived. The original error equations look very complicated, so a group of simplified error equations are proposed after the features of noise are analyzed. Then a serial of similar noise analyzing method are applied to the proposed PCMP. The performance of the each PCMP can be estimated by its corresponding noise analysis. Both simulation and lots of experiments were taken to test and prove the proposed PCMP. Finally the PCMP are helpful to improve the quality of 3-D measurement.

Gamma Model

Due to the non-linear response of the optical devices, the captured images are distorted by the gamma. While the effects of this distortion diminish with an increasing number of employed phase-shifted patterns, gamma distortion may be unavoidable

in real-time systems where the number of projected patterns is limited by the presence of target motion. In the previous works, researchers attempted to correct that distortion but they suffered from their inaccurate gamma model and had to employ approximate approaches to minimize the distortion.

As stated previously, this is the short-coming of a simple, second-order, gamma model or on using complicated calibration procedures when, as will be shown in Chapter 4, having an accurate model, for predicting the effects of gamma distortion on PMP, allows one to avail themselves of the pre-calibration procedure and to measure phase more accurately.

Chapter 4 proposes a detailed mathematical gamma model [115] to determine the relationship between phase error and gamma, and with this relationship, we will demonstrate that phase correction can be performed with or without an explicit gamma calibration procedure based upon involving the higher-order harmonics from the captured PMP sequence. Gamma calibration is performed by computing the energy in the higher order harmonics on a pixel-by-pixel basis, from a set of PMP patterns reflected off an arbitrary surface, instead of fitting a one-parameter gamma model to the tone reproduction curve observed from a small center section of the projected pattern reflecting off a flat, textureless surface. Without explicit calibration, gamma correction is achieved by deriving both a gamma parameter and a phase parameter, when processing the collected patterns of a PMP scan, such that the energy in the higher order harmonics are driven toward zero. For those willing to perform gamma calibration, the proposed gamma model greatly improves the resulting calibration accuracy.

In our experiments, the root mean squared (RMS) of phase error for 3-pattern PMP can be reduced $60\times$ when our gamma model is applied with gamma calibration and by at least $33\times$ without calibration. To this end, we propose two categories of methods for minimizing the effects of gamma according to our model: (1) correction without gamma calibration; and (2) correction with a calibrated gamma value. Finally using the proposed model, it will be shown that as the number of projected, phase-shifted patterns, increases, the effects of gamma are lessened. Although this feature of PMP has been observed previously, no quantitative analysis has been performed to predict the relationship between the effects of gamma and the pattern number.

1.4 Summation

To summarize the contributions of this research, the basic study aims at 3-D reconstruction in real time where, in order to achieve a high-quality 3-D measurement, two typical issues of pattern robustness need to be addressed. The first issue relates to additive uncertainty and our strategy of a novel high-frequency stripe pattern that is instantly decodable by means of temporal phase unwrapping. The issue of gamma distortion and its affect on the reconstructed phase image is also addressed where we claim that the gamma distortion in PMP is solved by building a detailed and accurate gamma model. And from this model, we describe a means of measuring the distortion parameters from the captured PMP images, which we then use to either calibrate the system for subsequent scans or even correct the distortion without any calibration. It is believed that these contributions will have a lasting impact on the

SLI research community as a commercially viable real-time SLI system has finally been achieved.

Chapter 2 Real-time 3-D Reconstruction

As mentioned in the previous Introduction section, in order to conquer the two bottlenecks, i. e., the arctangent function for phase generation and matrix computation for 3-D coordinates reconstruction, we proposed LUT-based solutions to achieve 3-D reconstruction in real time. By analyzing the original equations and rewriting the equations into new forms, the involved LUTs are built accurately. In our experiments, tested by our special software, the framerate of phase generation and 3-D coordinates reconstruction can achieve more than 1000 fps and nearly 230 fps respectively, which are, respectively, 25 and 10 times faster than traditional methods.

2.1 LUT-based processing

LUT-based programming is a well known and widely used technique [112] for minimizing processing latency. In this section, we implement LUT-based processing for deriving the modulation, B^c , and phase, ϕ , terms for traditional PMP that is suitable for all triangulation-based 3-D measurement, such as 2+1 [6], fast three-step [71], and our proposed PCMP. The proposed LUT-based processing takes advantage of the need by real-time systems to use as few patterns as possible by using the 8-bits per pixel, of the captured pattern set, as the indices into the LUT. By having LUTs that account for every possible combination of captured pixel value over the pattern set while storing double-precision results, the proposed scheme is completely lossless compared to traditional processing.

Modulation

As a first step in reducing the computational complexity associated with Eqs. (1.4), (1.7), and (1.15), we simplify the determination of B^c by rewriting Eq. (1.4) as:

$$B^c = \frac{1}{3}\sqrt{3(I_1^c - I_2^c)^2 + (2I_0^c - I_1^c - I_2^c)^2} \quad (2.1)$$

for $N = 3$,

$$B^c = \frac{1}{2}\sqrt{(I_1^c - I_3^c)^2 + (I_0^c - I_2^c)^2} \quad (2.2)$$

for $N = 4$, or

$$B^c = \frac{1}{6}\sqrt{3(I_1^c + I_2^c - I_4^c - I_5^c)^2 + (2I_0^c - 2I_3^c + I_1^c - I_2^c - I_4^c + I_5^c)^2} \quad (2.3)$$

for $N = 6$. Noting that we need only solve these equations for 8-bits per pixel I_n^c images, we can implement a modulation look-up table, MLUT, that, for $N = 3$, is defined according to

$$MLUT[U_3, V_3] = \frac{1}{3}\sqrt{3V_3^2 + U_3^2}, \quad (2.4)$$

where integer indices V_3 and U_3 are derived from

$$V_3 = I_1^c - I_2^c \quad (2.5)$$

and

$$U_3 = 2I_0^c - I_1^c - I_2^c; \quad (2.6)$$

for $N = 4$, is defined according to

$$MLUT[U_4, V_4] = \frac{1}{2}\sqrt{V_4^2 + U_4^2}, \quad (2.7)$$

where integer indices V_4 and U_4 are derived from

$$V_4 = I_1^c - I_3^c \quad (2.8)$$

and

$$U_4 = I_0^c - I_2^c; \quad (2.9)$$

or for $N = 6$, is defined according to

$$MLUT[U_6, V_6] = \frac{1}{6} \sqrt{3V_6^2 + U_6^2}, \quad (2.10)$$

where integer indices V_6 and U_6 are derived from

$$V_6 = I_1^c + I_2^c - I_4^c - I_5^c \quad (2.11)$$

and

$$U_6 = 2I_0^c - 2I_3^c + I_1^c - I_2^c - I_4^c + I_5^c. \quad (2.12)$$

The double-precision results of Eq. (2.4), (2.7) or (2.10) are stored in the MLUT. In contrast to Eq. (1.4), MLUT reduces the run-time computation cost of modulation without losing accuracy, where the size of the LUT is determined by the number of bits per pixel of the camera sensor and the number of patterns being projected.

In practice, the term B^c is typically employed as a shadow noise filter [49], and additionally, as discussed in later section on PCMP, we prefer to using it as texture of the scanned object too. Figure 2.1 (left) shows the MLUTs for $N = 3$ (top), $N = 4$ (middle) and $N = 6$ (bottom) respectively. Because the valid and normalized value in the MLUTs is in $[0, 1]$ according to the discuss on PCMP later, the MLUTs look like a ellipse for $N = 3$ and $N = 6$ or a circle for $N = 4$.

Phase

As our second step to producing real-time 3-D video with texture, we intend to minimize the computational complexity associated with generating phase video where

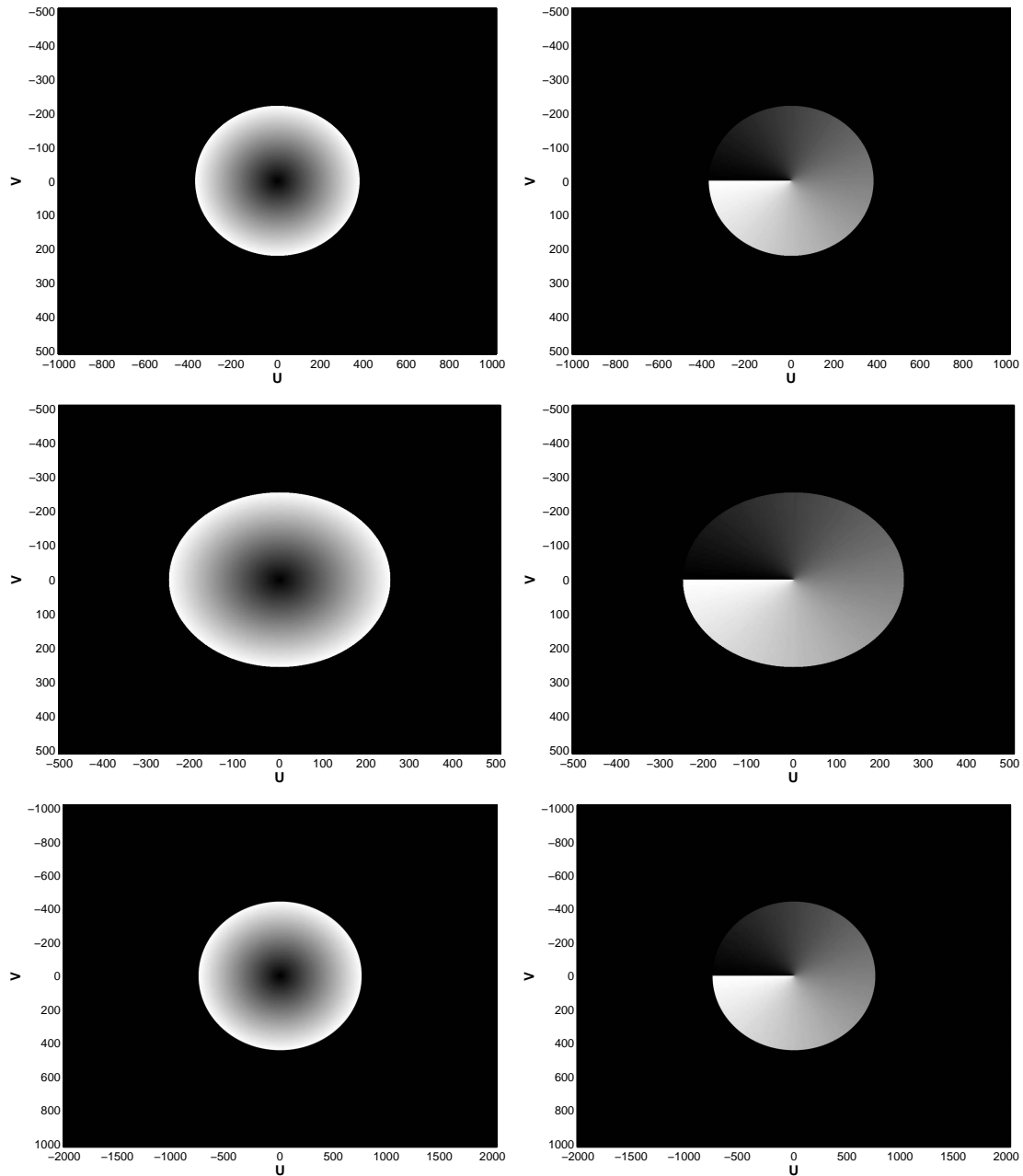


Figure 2.1: Visualizations of MLUT (left) and PLUT (right) for $N = 3$ (top), $N = 4$ (middle) and $N = 6$ (bottom) respectively.

the arctangent function has long been considered a significant obstacle for fringe pattern analysis [116]. Previous approaches to this problem include Huang *et al.*'s cross ratio algorithm [71] and Guo *et al.*'s approximation algorithm [116]. However, these methods reduce computational cost at the expense of accuracy and are not

faster than our LUT-based algorithms.

As we did with Eq. (1.4) for B^c , we simplify Eq. (1.7) according to the number of patterns N such that

$$\phi = \arctan \left[\frac{\sqrt{3}(I_1^c - I_2^c)}{2I_0^c - I_1^c - I_2^c} \right] \quad (2.13)$$

for $N = 3$,

$$\phi = \arctan \left[\frac{I_1^c - I_3^c}{I_0^c - I_2^c} \right] \quad (2.14)$$

for $N = 4$, or

$$\phi = \arctan \left[\frac{\sqrt{3}(I_1^c + I_2^c - I_4^c - I_5^c)}{2I_0^c - 2I_3^c + I_1^c - I_2^c - I_4^c + I_5^c} \right] \quad (2.15)$$

for $N = 6$.

Again based on the fact that the intensity values of grabbed images are range-limited integers, we can implement these calculations through a phase LUT (PLUT), for $N = 3$, defined according to

$$PLUT[U_3, V_3] = \arctan \left[\frac{\sqrt{3}V}{U} \right], \quad (2.16)$$

where V_3 and U_3 are defined in Eqs. (2.5) and (2.6) respectively; for $N = 4$, defined according to

$$PLUT[U_4, V_4] = \arctan \left[\frac{V}{U} \right], \quad (2.17)$$

where V_4 and U_4 are defined in Eqs. (2.8) and (2.9) respectively; or for $N = 6$, defined according to

$$PLUT[U_6, V_6] = \arctan \left[\frac{\sqrt{3}V}{U} \right], \quad (2.18)$$

where V_6 and U_6 are defined in Eqs. (2.11) and (2.12) respectively.

The double-precision results are stored in the PLUT. Thus, the time-consuming arctangent operation is pre-performed, and phase values are obtained by accessing the pre-computed PLUT whose size is, again, determined by the number of bits per pixel of the sensor as well as the number of patterns projected with no loss in accuracy. Compared to Eqs. (1.7), PLUT avoids computing arctangent function at run-time such that the computational cost of phase is greatly reduced without introducing distortion. Figure 2.1 (right) shows the PLUTs for $N = 3$ (top), $N = 4$ (middle) and $N = 6$ (bottom). The valid value in the PLUT is determined by its corresponding MLUT.

3-D Point Cloud

Having obtained both the phase and modulation images by means of LUTs, we begin our derivation of a LUT for the purpose of implementing Eq. (1.15). For a 3×3 matrix A which is defined as

$$A = \begin{pmatrix} a_{11}, & a_{12}, & a_{13} \\ a_{21}, & a_{22}, & a_{23} \\ a_{31}, & a_{32}, & a_{33} \end{pmatrix}, \quad (2.19)$$

its inverse matrix is

$$A^{-1} = \frac{1}{|A|} \begin{pmatrix} a_{22}a_{33} - a_{23}a_{32}, & a_{13}a_{32} - a_{12}a_{33}, & a_{12}a_{23} - a_{13}a_{22} \\ a_{23}a_{31} - a_{21}a_{33}, & a_{11}a_{33} - a_{13}a_{31}, & a_{13}a_{21} - a_{11}a_{23} \\ a_{21}a_{32} - a_{22}a_{31}, & a_{12}a_{31} - a_{11}a_{32}, & a_{11}a_{22} - a_{12}a_{21} \end{pmatrix}, \quad (2.20)$$

where $|\cdot|$ is matrix determinant operation.

After matrix inverse and matrix multiplication operations are performed, Eq (1.15) can be expanded into our first direct algebraic forms as

$$T_1 = [C(x^c, y^c)y^p + 1]^{-1}, \quad (2.21)$$

$$X^w = [A_x(x^c, y^c)y^p + B_x(x^c, y^c)]T_1, \quad (2.22)$$

$$Y^w = [A_y(x^c, y^c)y^p + B_y(x^c, y^c)]T_1, \quad (2.23)$$

and

$$Z^w = [A_z(x^c, y^c)y^p + B_z(x^c, y^c)]T_1, \quad (2.24)$$

where

$$D(x^c, y^c) = [d_1x^c + d_2y^c + d_3]^{-1},$$

$$A_x(x^c, y^c) = [a_{x1}x^c + a_{x2}y^c + a_{x3}]D,$$

$$B_x(x^c, y^c) = [b_{x1}x^c + b_{x2}y^c + b_{x3}]D,$$

$$A_y(x^c, y^c) = [a_{y1}x^c + a_{y2}y^c + a_{y3}]D,$$

$$B_y(x^c, y^c) = [b_{y1}x^c + b_{y2}y^c + b_{y3}]D,$$

$$A_z(x^c, y^c) = [a_{z1}x^c + a_{z2}y^c + a_{z3}]D,$$

$$B_z(x^c, y^c) = [b_{z1}x^c + b_{z2}y^c + b_{z3}]D,$$

and

$$C(x^c, y^c) = [c_1x^c + c_2y^c + c_3]D,$$

with

$$a_{x1} = m_{22}^c m_{34}^c m_{33}^p + m_{23}^c m_{32}^c m_{34}^p + m_{24}^c m_{33}^c m_{32}^p - m_{22}^c m_{33}^c m_{34}^p - m_{23}^c m_{34}^c m_{32}^p - m_{24}^c m_{32}^c m_{33}^p,$$

$$a_{x2} = m_{12}^c m_{33}^c m_{34}^p + m_{13}^c m_{34}^c m_{32}^p + m_{14}^c m_{32}^c m_{33}^p - m_{12}^c m_{34}^c m_{33}^p - m_{13}^c m_{32}^c m_{34}^p - m_{14}^c m_{33}^c m_{32}^p,$$

$$a_{x3} = m_{12}^c m_{24}^c m_{33}^p + m_{13}^c m_{22}^c m_{34}^p + m_{14}^c m_{23}^c m_{32}^p - m_{12}^c m_{23}^c m_{34}^p - m_{13}^c m_{24}^c m_{32}^p - m_{14}^c m_{22}^c m_{33}^p,$$

$$a_{y1} = m_{21}^c m_{33}^c m_{34}^p + m_{23}^c m_{34}^c m_{31}^p + m_{24}^c m_{31}^c m_{33}^p - m_{21}^c m_{34}^c m_{33}^p - m_{23}^c m_{31}^c m_{34}^p - m_{24}^c m_{33}^c m_{31}^p,$$

$$\begin{aligned}
a_{y2} &= m_{11}^c m_{34}^c m_{33}^p + m_{13}^c m_{31}^c m_{34}^p + m_{14}^c m_{33}^c m_{31}^p - m_{11}^c m_{33}^c m_{34}^p - m_{13}^c m_{34}^c m_{31}^p - m_{14}^c m_{31}^c m_{33}^p, \\
a_{y3} &= m_{11}^c m_{23}^c m_{34}^p + m_{13}^c m_{24}^c m_{31}^p + m_{14}^c m_{21}^c m_{33}^p - m_{11}^c m_{24}^c m_{33}^p - m_{13}^c m_{21}^c m_{34}^p - m_{14}^c m_{23}^c m_{31}^p, \\
a_{z1} &= m_{21}^c m_{34}^c m_{32}^p + m_{22}^c m_{31}^c m_{34}^p + m_{24}^c m_{32}^c m_{31}^p - m_{21}^c m_{32}^c m_{34}^p - m_{22}^c m_{34}^c m_{31}^p - m_{24}^c m_{31}^c m_{32}^p, \\
a_{z2} &= m_{11}^c m_{32}^c m_{34}^p + m_{12}^c m_{34}^c m_{31}^p + m_{14}^c m_{31}^c m_{32}^p - m_{11}^c m_{34}^c m_{32}^p - m_{12}^c m_{31}^c m_{34}^p - m_{14}^c m_{32}^c m_{31}^p, \\
a_{z3} &= m_{11}^c m_{24}^c m_{32}^p + m_{12}^c m_{21}^c m_{34}^p + m_{14}^c m_{22}^c m_{31}^p - m_{11}^c m_{22}^c m_{34}^p - m_{12}^c m_{24}^c m_{31}^p - m_{14}^c m_{21}^c m_{32}^p, \\
b_{x1} &= m_{22}^c m_{33}^c m_{24}^p + m_{23}^c m_{34}^c m_{22}^p + m_{24}^c m_{32}^c m_{23}^p - m_{22}^c m_{34}^c m_{23}^p - m_{23}^c m_{32}^c m_{24}^p - m_{24}^c m_{33}^c m_{22}^p, \\
b_{x2} &= m_{12}^c m_{34}^c m_{23}^p + m_{13}^c m_{32}^c m_{24}^p + m_{14}^c m_{33}^c m_{22}^p - m_{12}^c m_{33}^c m_{24}^p - m_{13}^c m_{34}^c m_{22}^p - m_{14}^c m_{32}^c m_{23}^p, \\
b_{x3} &= m_{12}^c m_{23}^c m_{24}^p + m_{13}^c m_{24}^c m_{22}^p + m_{14}^c m_{22}^c m_{23}^p - m_{12}^c m_{24}^c m_{23}^p - m_{13}^c m_{22}^c m_{24}^p - m_{14}^c m_{23}^c m_{22}^p, \\
b_{y1} &= m_{21}^c m_{34}^c m_{23}^p + m_{23}^c m_{31}^c m_{24}^p + m_{24}^c m_{33}^c m_{21}^p - m_{21}^c m_{33}^c m_{24}^p - m_{23}^c m_{34}^c m_{21}^p - m_{24}^c m_{31}^c m_{23}^p, \\
b_{y2} &= m_{11}^c m_{33}^c m_{24}^p + m_{13}^c m_{34}^c m_{21}^p + m_{14}^c m_{31}^c m_{23}^p - m_{11}^c m_{34}^c m_{23}^p - m_{13}^c m_{31}^c m_{24}^p - m_{14}^c m_{33}^c m_{21}^p, \\
b_{y3} &= m_{11}^c m_{24}^c m_{23}^p + m_{13}^c m_{21}^c m_{24}^p + m_{14}^c m_{23}^c m_{21}^p - m_{11}^c m_{23}^c m_{24}^p - m_{13}^c m_{24}^c m_{21}^p - m_{14}^c m_{21}^c m_{23}^p, \\
b_{z1} &= m_{21}^c m_{32}^c m_{24}^p + m_{22}^c m_{34}^c m_{21}^p + m_{24}^c m_{31}^c m_{22}^p - m_{21}^c m_{34}^c m_{22}^p - m_{22}^c m_{31}^c m_{24}^p - m_{24}^c m_{32}^c m_{21}^p, \\
b_{z2} &= m_{11}^c m_{34}^c m_{22}^p + m_{12}^c m_{31}^c m_{24}^p + m_{14}^c m_{32}^c m_{21}^p - m_{11}^c m_{32}^c m_{24}^p - m_{12}^c m_{34}^c m_{21}^p - m_{14}^c m_{31}^c m_{22}^p, \\
b_{z3} &= m_{11}^c m_{22}^c m_{24}^p + m_{12}^c m_{24}^c m_{21}^p + m_{14}^c m_{21}^c m_{22}^p - m_{11}^c m_{24}^c m_{22}^p - m_{12}^c m_{21}^c m_{24}^p - m_{14}^c m_{22}^c m_{21}^p, \\
c_1 &= m_{21}^c m_{32}^c m_{33}^p + m_{22}^c m_{33}^c m_{31}^p + m_{23}^c m_{31}^c m_{32}^p - m_{21}^c m_{33}^c m_{32}^p - m_{22}^c m_{31}^c m_{33}^p - m_{23}^c m_{32}^c m_{31}^p, \\
c_2 &= m_{11}^c m_{33}^c m_{32}^p + m_{12}^c m_{31}^c m_{33}^p + m_{13}^c m_{32}^c m_{31}^p - m_{11}^c m_{32}^c m_{33}^p - m_{12}^c m_{33}^c m_{31}^p - m_{13}^c m_{31}^c m_{32}^p, \\
c_3 &= m_{11}^c m_{22}^c m_{33}^p + m_{12}^c m_{23}^c m_{31}^p + m_{13}^c m_{21}^c m_{32}^p - m_{11}^c m_{23}^c m_{32}^p - m_{12}^c m_{21}^c m_{33}^p - m_{13}^c m_{22}^c m_{31}^p, \\
d_1 &= m_{21}^c m_{33}^c m_{22}^p + m_{22}^c m_{31}^c m_{23}^p + m_{23}^c m_{32}^c m_{21}^p - m_{21}^c m_{32}^c m_{23}^p - m_{22}^c m_{33}^c m_{21}^p - m_{23}^c m_{31}^c m_{22}^p, \\
d_2 &= m_{11}^c m_{32}^c m_{23}^p + m_{12}^c m_{33}^c m_{21}^p + m_{13}^c m_{31}^c m_{22}^p - m_{11}^c m_{33}^c m_{22}^p - m_{12}^c m_{31}^c m_{23}^p - m_{13}^c m_{32}^c m_{21}^p,
\end{aligned}$$

and

$$d_3 = m_{11}^c m_{23}^c m_{22}^p + m_{12}^c m_{21}^c m_{23}^p + m_{13}^c m_{22}^c m_{21}^p - m_{11}^c m_{22}^c m_{23}^p - m_{12}^c m_{23}^c m_{21}^p - m_{13}^c m_{21}^c m_{22}^p.$$

Expressed by normalized homogeneous coordinates, Eqs. (2.21), (2.22), (2.23) and

(2.24) can be written as

$$s \begin{pmatrix} X^w \\ Y^w \\ Z^w \\ 1 \end{pmatrix} = \begin{bmatrix} A_x(x^c, y^c), & B_x(x^c, y^c) \\ A_y(x^c, y^c), & B_y(x^c, y^c) \\ A_z(x^c, y^c), & B_z(x^c, y^c) \\ C(x^c, y^c), & 1 \end{bmatrix} \begin{pmatrix} y^p \\ 1 \end{pmatrix},$$

where s is a scalar. If the 3-D coordinates are computed by Eqs. (2.21), (2.22), (2.23)

and (2.24), there are 1 division, 7 multiplications and 4 additions involved.

Analyzing Eqs. (2.21), (2.22), (2.23) and (2.24) furthermore, our second forms of 3-D LUT can be obtained as

$$T_2 = [C(x^c, y^c)y^p + 1]^{-1}, \quad (2.25)$$

$$X^w = M_x(x^c, y^c) + N_x(x^c, y^c)T_2, \quad (2.26)$$

$$Y^w = M_y(x^c, y^c) + N_y(x^c, y^c)T_2, \quad (2.27)$$

and

$$Z^w = M_z(x^c, y^c) + N_z(x^c, y^c)T_2, \quad (2.28)$$

where

$$M_x(x^c, y^c) = A_x(x^c, y^c)C^{-1}(x^c, y^c),$$

$$N_x(x^c, y^c) = B_x(x^c, y^c) - M_x(x^c, y^c),$$

$$M_y(x^c, y^c) = A_y(x^c, y^c)C^{-1}(x^c, y^c),$$

$$N_y(x^c, y^c) = B_y(x^c, y^c) - M_y(x^c, y^c),$$

$$M_z(x^c, y^c) = A_z(x^c, y^c)C^{-1}(x^c, y^c),$$

and

$$N_z(x^c, y^c) = B_z(x^c, y^c) - M_z(x^c, y^c).$$

Note that $C^{-1}(x^c, y^c)$ is the reciprocal of $C(x^c, y^c)$ other than its inverse matrix. If the 3-D coordinates are computed by Eqs. (2.25), (2.26), (2.27) and (2.28), there are 1 division, 4 multiplications and 4 additions involved.

We then note that, based on the mapping of world coordinates to the camera plane [9] by M^c , if Z^w is calculated according to

$$Z^w = M_z(x^c, y^c) + \frac{N_z(x^c, y^c)}{C(x^c, y^c)y^p + 1}, \quad (2.29)$$

then X^w and Y^w can be computed respectively as

$$X^w = E_x(x^c, y^c)Z^w + F_x(x^c, y^c), \quad (2.30)$$

and

$$Y^w = E_y(x^c, y^c)Z^w + F_y(x^c, y^c), \quad (2.31)$$

where

$$E_x(x^c, y^c) = \frac{(m_{22}^c m_{33}^c - m_{23}^c m_{32}^c)x^c + (m_{13}^c m_{32}^c - m_{12}^c m_{33}^c)y^c + (m_{12}^c m_{23}^c - m_{13}^c m_{22}^c)}{(m_{21}^c m_{32}^c - m_{22}^c m_{31}^c)x^c + (m_{12}^c m_{31}^c - m_{11}^c m_{32}^c)y^c + (m_{11}^c m_{22}^c - m_{12}^c m_{21}^c)},$$

$$F_x(x^c, y^c) = \frac{(m_{22}^c m_{34}^c - m_{24}^c m_{32}^c)x^c + (m_{14}^c m_{32}^c - m_{12}^c m_{34}^c)y^c + (m_{12}^c m_{24}^c - m_{14}^c m_{22}^c)}{(m_{21}^c m_{32}^c - m_{22}^c m_{31}^c)x^c + (m_{12}^c m_{31}^c - m_{11}^c m_{32}^c)y^c + (m_{11}^c m_{22}^c - m_{12}^c m_{21}^c)},$$

$$E_y(x^c, y^c) = \frac{(m_{23}^c m_{31}^c - m_{21}^c m_{33}^c)x^c + (m_{11}^c m_{33}^c - m_{13}^c m_{31}^c)y^c + (m_{13}^c m_{21}^c - m_{11}^c m_{23}^c)}{(m_{21}^c m_{32}^c - m_{22}^c m_{31}^c)x^c + (m_{12}^c m_{31}^c - m_{11}^c m_{32}^c)y^c + (m_{11}^c m_{22}^c - m_{12}^c m_{21}^c)},$$

and

$$F_y(x^c, y^c) = \frac{(m_{21}^c m_{32}^c - m_{22}^c m_{31}^c)x^c + (m_{12}^c m_{31}^c - m_{11}^c m_{32}^c)y^c + (m_{11}^c m_{22}^c - m_{12}^c m_{21}^c)}{(m_{21}^c m_{32}^c - m_{22}^c m_{31}^c)x^c + (m_{12}^c m_{31}^c - m_{11}^c m_{32}^c)y^c + (m_{11}^c m_{22}^c - m_{12}^c m_{21}^c)}.$$

This is the third forms of our 3-D LUT. If the 3-D coordinates are computed by Eqs. (2.29), (2.30) and (2.31), there are 1 division, 3 multiplications and 4 additions involved.

Table 2.1 shows number of operations involved in the proposed three kinds of 3-D reconstruction LUTs. So finally the method for computing 3-D coordinates is by employing Eqs. (2.29), (2.30) and (2.31). Implementing the 7 parameters M_z , N_z , C , E_x , E_y , F_x , and F_y by means of table look-up for indices (x^c, y^c) (camera column and row indices), reduces the total computational complexity associated with deriving the 3-D point cloud from the phase term to 7 look-ups, 4 additions, 3 multiplications, and 1 division, which is significantly less than what is involved in performing matrix inversion and matrix multiplication, as required by Eq. (1.15). It should be noted that the method presented in Eqs. (2.29), (2.30) and (2.31) can be applied to all triangulation-based, 3-D coordinate, reconstruction techniques including stereo vision.

Table 2.1: Comparison of three kinds of 3-D reconstruction LUTs

	Multiplication	division	addition
Eqs (2.21), (2.22), (2.23) and (2.24)	7	1	4
Eqs (2.25), (2.26), (2.27) and (2.28)	4	1	4
Eqs (2.29), (2.30) and (2.31)	3	1	4

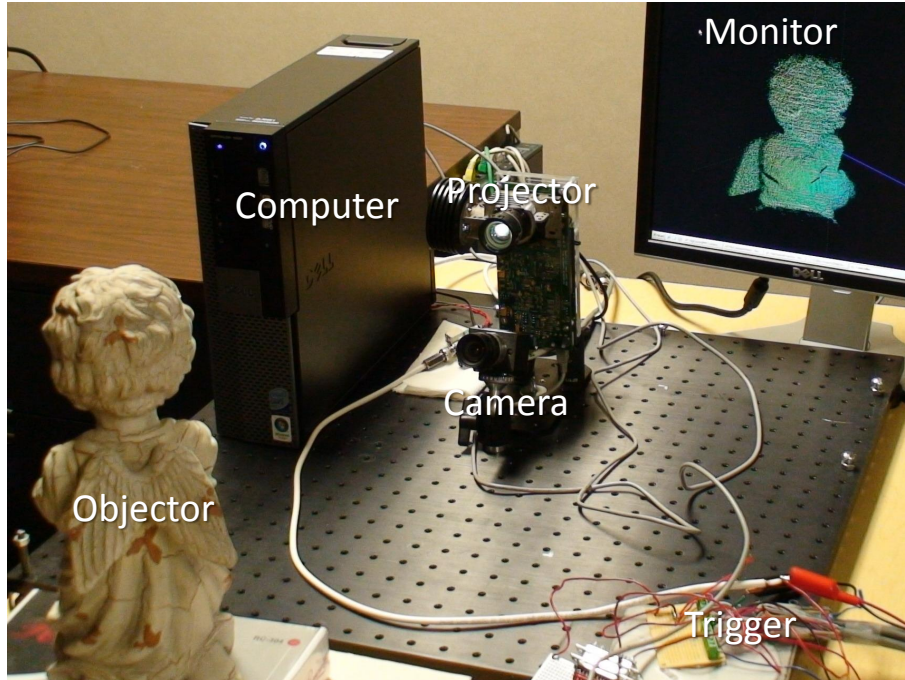


Figure 2.2: Experimental setup.

2.2 Experiments

In order to test the performance of the proposed pattern scheme and LUT-based processing, we programmed the experimental system of Fig. 2.2 using Microsoft Visual Studio 2005 with managed C++. The imaging sensor is an 8-bits per pixel, monochrome, Prosilica GC640M, gigabit ethernet camera with a frame rate of 120 fps and 640×480 pixel resolution. The projector is composed of a Texas Instrument's Discovery 1100 board with ALP-1 controller and LED-OM with 225 ANSI lumens. The projector has a maximum frame rate of 150 fps at a resolution of 1024×768 and 8-bits per pixel grayscale. The camera and projector are synchronized by an external triggering circuit. As our processing unit, we used a Dell Optiplex 960 with an Intel Core 2 Duo Quad Q9650 processor running at 3.0 GHz.

Table 2.2: Processing time and rate, in milliseconds and frames per second (in parentheses), respectively, for various stages of PMP processing by means of the equations and LUT described in this paper.

Process	N = 3	N = 4	N = 6
Eq. (1.4)	58.88 (17.58)	67.34 (14.85)	127.72 (8.22)
Eq. (1.7)	71.40 (14.01)	79.53 (12.57)	135.31 (7.39)
*1 Eq. (1.15)	45.00 (22.22)	44.85 (22.30)	45.16 (22.14)
*2 Eq. (2.1), (2.2) and (2.3)	6.72 (148.81)	2.34 (427.35)	10.00 (100.00)
*3 Eq. (2.13), (2.14) and (2.15)	17.97 (55.65)	18.90 (52.91)	18.75 (53.33)
MLUT: Eq. (2.4), (2.7) and (2.10)	0.94 (1063.83)	1.25 (800.00)	2.18 (458.72)
PLUT: Eq. (2.16), (2.17) and (2.18)	0.94 (1063.83)	1.25 (800.00)	2.19 (456.62)
MLUT and PLUT, combined	1.40 (714.29)	1.72 (581.40)	2.81 (355.87)
MLUT and PLUT for 2 plus 1 [6]	1.39 (719.81)	-	-
3-D LUT: Eq. (2.29), (2.30) and (2.31)	4.37 (228.83)	4.37 (228.83)	4.38 (228.31)
Traditional PMP: *2, *3, and then *1	65.97 (15.16)	65.0 (15.38)	68.75 (14.55)
MLUT and PLUT, and then 3-D LUT	5.77 (173.31)	6.09 (164.20)	7.18 (139.28)

Our experiments include: (1) scanning static scene with the traditional PMP with unit frequency for $N = 3, 4$ and 6 involving LUT-based processing and (2) scanning a moving hand with dual-frequency patterns for $N = 6$ by means of LUT-based processing.

In our first experiment, a static object was scanned using traditional PMP with unit frequency with $N = 3, 4$, and 6 for the purpose of measuring the speed at which our LUT-based algorithms perform without phase unwrapping. Although the processor has four cores, our reported processing rates for each LUT algorithm are based on using just a one core. And although B^c could be used as a shadow noise filter, thus reducing the number of pixels that would need to be processed while

deriving ϕ , we computed a phase value for the full set of 640×480 pixels such that our observed processing times represent an upper limit. Under these conditions, the average computation time over 1,000 runs for modulation B^c and phase ϕ was then reported in Table 2.2. B^c acts as texture in this experiment.

In an overview of Table 2.2 for the total processing time including texture generation, phase generation, and 3-D reconstruction, our LUT-based computations are 173.31 fps for $N = 3$, 164.20 fps for $N = 4$, and 139.28 for $N = 6$ versus, using traditional PMP, 15.16 fps for $N = 3$, 15.38 fps for $N = 4$, and 14.55 fps for $N = 6$, which means our LUT-based algorithms is $10\times$ faster than traditional PMP algorithms. Using the general modulation equation, Eqs. (1.4), and the general phase equation, (1.7), the processing time is increased with larger N , because larger N means more $\sin(\cdot)$, $\cos(\cdot)$ and summation computations. The processing time and rates are listed in Table 2.2.

With the simplified modulation equations of Eq. (2.1), (2.2), and (2.3), the processing time decreases significantly for $N = 4$ (2.34 *ms*) compared with $N = 3$ (6.72 *ms*) because, before performing square-root computation, there are only 2 subtractions, 1 addition, and 2 square computations for $N = 4$. There are 3 subtractions, 1 addition, 2 multiplications, and 2 square computations for $N = 3$. Using the simplified phase equation, Eq. (2.13), (2.14), and (2.15), the processing time is almost the same for different N because, although the processing time for the basic computations, such as addition and subtraction, is still varied for different N . Such basic processing time is negligible compared to the processing time for the processing hungry arctangent function.

Furthermore, it is found from Table 2.2 that the performance of MLUT and PLUT is the same for different N because the computations for the integer indices, U and V , are the same for both MLUT and PLUT with the same N as is the time for accessing MLUT and PLUT. However, the processing time for MLUT/PLUT is increased with increasing N because the time for accessing the image buffer, I_n^c , increases; therefore, accessing this buffer is the predominant factor in this case. In practice when we want to access MLUT and PLUT, the computations of U and V need only be performed once. So Table 2.2 also shows the processing time of the row marked as “MLUT and PLUT, combined” is less than the summation time of the row marked as “MLUT: Eq. (2.4), (2.7) and then (2.10)” and the row marked as “PLUT: Eq. (2.16), (2.17) and then (2.18)” in which their U and V were computed respectively.

For testing 3-D reconstruction using a single processing core, we implemented reconstruction by means of matrix-inversion (Eq. (1.15)) versus our LUT-based implementation of Sec. 2.1. With our 3-D LUT algorithm, the frame rate of 3-D reconstruction is 228.83 fps for 640×480 image resolution, which is 10.3 times faster than matrix inversion by means of Eq (1.15). For added comparison, Zhang et al. reported a reconstruction frame rate of 25.56 fps with a resolution of 532×500 when performing matrix inversion by means of GPU processing on an nVidia Quadro FX 3450 [74]. For Zhang et al.’s $2 + 1$ pattern strategy [6], our LUT analysis can be also applied, and the performance is shown in Table 2.2.

In our second experiment, we scanned a human subject’s hand gestures with PMP ($N = 4$) using LUT-based processing. Different from our first experiment, the most recent N video frames are captured live and stored in a shared image buffer by a



Figure 2.3: Sample video clips.

camera thread. At the same time, a second thread performs modulation and phase generation from the shared buffer and stores the computed data into a modulation and phase buffer. A third thread, simultaneously, performs 3-D reconstruction using data from this modulation buffer, storing the 3-D point cloud results into a 3-D data buffer. Finally, a fourth thread displays the data from the 3-D data buffer using OpenGL. Because the speed of the camera/projector pair is 120 fps, the speed of final 3-D reconstruction is also 120 fps while the display speed is limited by the LCD



Figure 2.4: Sample point clouds, using PMP with $N = 4$, live show of various hand poses.

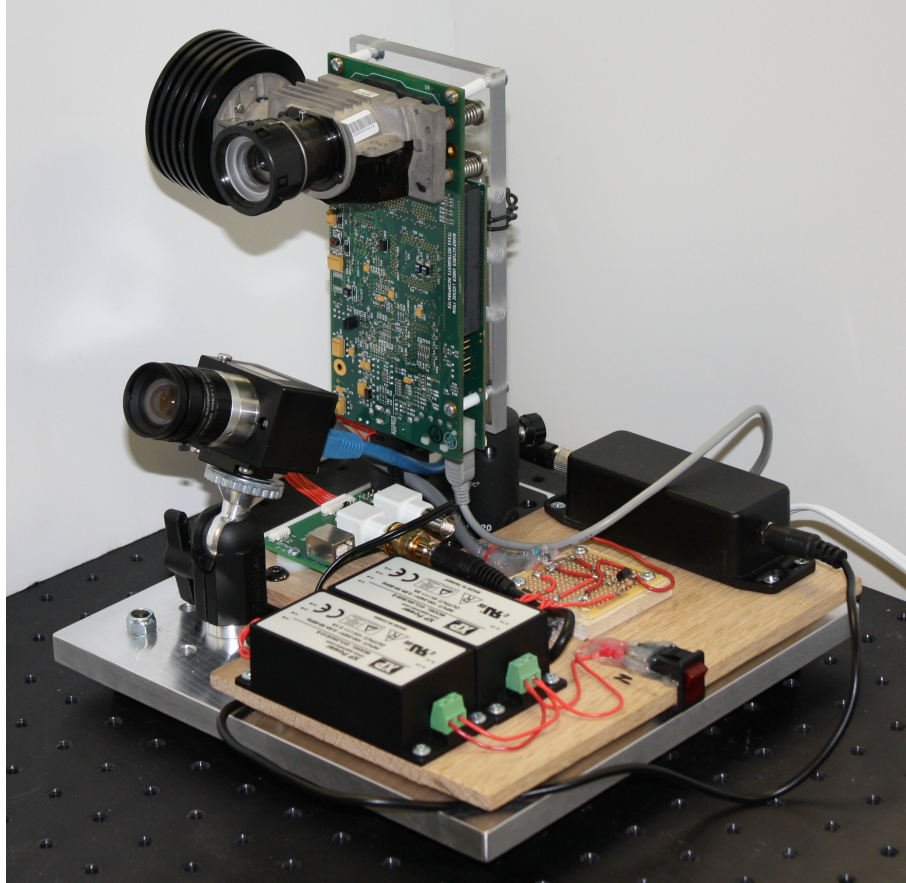


Figure 2.5: Our latest real-time 3-D system.

display at 40 – 50 fps.

Figure 2.3 shows a human subject's hand gestures. In the case of Fig. 2.3 (left), we show the entire system along with the subject's hand as a way of demonstrating that video is being acquired and displayed on screen and in real-time where there is no noticeable delay between the gesture's performed by the subject and displayed on screen. On the LCD panel, you can see the XYZ axes labeled as blue, green, and red lines, respectively, while the 3-D point cloud is also being reflected off the XZ plane as a way of better illustrating the hand coming forward and away from the camera. In the video clips of Fig. 2.3 (center) and (right), we show the subject's hand held

in front of a white cardboard box. The purpose of these clips is to show that we can track multiple, disjoint objects, since there are no phase ambiguities when using dual-frequency pattern scheme. For added inspection, the images in Fig. 2.4 show the live frames of hand poses where, from visual inspection, one can see the texture/intensity encoding of the points derived from B^c . Points with low modulation strength are not displayed.

Differing from the previous experimental system, there is no external trigger circuit in our latest real-time 3-D SLI system. The projector is synchronized to the camera directly, and is triggered by the signal sent from the camera. The previous system suffers from the framerate of the external trigger circuit whose highest framerate is 120 fps. With being triggered by the camera directly, the highest framerate of the system can achieve 140–150 fps finally.

Chapter 3 Phase Channel Multiplexing Pattern Strategy

When Eqs. (1.3), (1.4) and (1.4) are employed to compute A^c , B^c and ϕ respectively, it is supposed under ideal condition. However, in practice, there are all kinds of uncertain and certain factors, such as additive noise thermal, shot noise, non-linear response/gamma distortion, flickering, quantization and so on, effecting the accuracy of computation. In this chapter, we will focus on suppressing the additive thermal noise, which is typically modeled as Gaussian, by phase channel multiplexing pattern (PCMP) strategy.

According to Li et al. [9], there are three factors suppressing noise in a PMP scan. The first factor is the number of patterns where more patterns lead to reduced noise. But for a real-time system, more patterns also means more processing. The second factor is the Signal-to-Noise-Ratio (SNR) between the light strength of the projected patterns versus the variance of sensor noise, where higher SNRs leads to lesser noise in the 3-D reconstructions. But for a fixed system, the projected signal strength is limited by the light source of the projector while sensor noise is inherent to the selected camera. The last factor is the frequency of projected pattern with higher pattern frequency leading to reduced noise in the 3-D reconstruction, but it also introduces ambiguities in the reconstruction process that needs to be dealt with by means of phase unwrapping. In our proposed PCMP, a unit-frequency signal is embedded into the high-frequency signal to achieve phase unwrapping effectively and robustly.

3.1 Parameters and noise analysis for PMP

In order to analyze problems associated with PMP, we can rewrite Eq. (1.1) as

$$I_n^p = \alpha_p \left[\frac{1}{2} + \frac{1}{2} \cos \left(2\pi f y^p - \frac{2\pi n}{N} \right) \right] + \beta_p, \quad (3.1)$$

where I_n^p is the light intensity of that pixel; f is the frequency of the sine wave; n represents the phase-shift index; $N \geq 3$ is the total number of phase shifted patterns; α_p is the amplitude constant of the sine wave; and β_p is the balance constant preventing images captured by a camera from underflow. Here “underflow” means that the intensity value in image captured by the camera becomes zero if the intensity of scene is lower than some threshold. For optimal performance, the term α_p should be as large as possible within the bounds of the projector’s dynamic range. As such, α_p and β_p are related through $\alpha_p + \beta_p = 2^m - 1$, where m is the bits-per-pixel of the projector.

In the camera, the corresponding captured images are defined according to Eq. (1.2), and the three unknown parameters in that equation A^c , B^c and ϕ are computed by Eqs. (1.3), (1.4) and (1.4) respectively. For the purpose of analyzing issues conveniently, we rewrite Eq. (1.2) as

$$I_n^c = \alpha \left\{ \alpha_p \left[\frac{1}{2} + \frac{1}{2} \cos \left(\phi - \frac{2\pi n}{N} \right) \right] + \beta_p + \beta \right\} + \beta, \quad (3.2)$$

where α is the reflectivity of the scanned object for the camera with a value range of $[0, 1]$ and β is the ambient light intensity for the camera. The signal terms inside $\{\cdot\}$, of Eq. (3.2), with the coefficient α represent the light reflected off the target object originating from either the pattern projector or from any ambient light sources, while

the term β , in Eq. (3.2), represents the ambient light directly entering the camera without reflection [25]. Both α and β are functions of (x^c, y^c) in the camera.

From Eq. (3.2), the terms A^c and B^c can be expressed as

$$A^c = \alpha \left[\frac{1}{2} \alpha_p + \beta_p + \beta \right] + \beta \quad (3.3)$$

and

$$B^c = 0.5 \alpha \alpha_p, \quad (3.4)$$

such that the ambient light intensity, β , can be derived from Eq. (3.3) according to

$$\beta = \frac{A^c - \alpha(\frac{1}{2}\alpha_p + \beta_p)}{\alpha + 1} \quad (3.5)$$

while the reflectivity, α , can be computed, from Eq. (3.4), according to

$$\alpha = \frac{2B^c}{\alpha_p}. \quad (3.6)$$

While the ambient light intensity is usually a positive value, there are some special cases, depending on the features of camera, where it may be negative as we will be show in the experimental section.

Now if β is positive, then the term, β_p , will typically be set to zero in order to make α_p as large as possible; however, if β is negative, then it is necessary to choose a suitable positive value for β_p in order to keep I_n^c from an underflow condition. That is, if we let $\alpha_p = 0$ and solve the inequality $I_n^c > 0$, then a suitable value for β_p , in Eq. (3.2), can be derived from

$$\beta_p > - \left(1 + \frac{1}{\alpha} \right) \beta, \quad (3.7)$$

which is very sensitive to α since the derivative of β_p is

$$d\beta_p = -\frac{\beta}{\alpha^2}d\alpha, \quad (3.8)$$

if we replace the inequality of Eq. (3.7) with an equality. So if we select β_p with α_1 , all the pixels with $\alpha \leq \alpha_1$ will no long be reliable. On the other hand, once the value of β_p is fixed, then reliable values of α will be determined according to

$$\alpha > -\frac{\beta}{\beta_p + \beta}, \quad (3.9)$$

if β is negative. If β is positive, then α can usually be any value in the range $[0, 1]$ with smaller α leading to lesser reliability in the phase measurement, which we will analyze in a later section.

In previous studies [5], researchers employed A^c as a measure of the texture of scanned objects with B^c [49] or B^c/A^c [90] as a phase quality indicator. In this paper, we tend to use α as both the texture and the quality indicator where α , in the normalized range of $[0, 1]$, is the reflectivity of the scanned object at each pixel for the common view of the camera and the projector. The term, A^c , depends on α , α_p , β , and β_p , while α is the reflectivity and represents the texture more naturally. The value range of B^c depends on the amplitude, α_p , of the projected patterns while α does not.

Noise analysis

Under ideal conditions, only three PMP patterns are needed according to the PMP algorithm. But in practice, there exist various noise sources, such as camera noise, projector noise, ambient light, shadowing, and so on [9], effecting the quality of 3-D

reconstruction by means of PMP. We combine these various noises into one parameter, w_n , and add it to Eq. (1.2) which, here, is written as

$$\tilde{I}_n^c = I_n^c + w_n, \quad (3.10)$$

where w_n , with the same mean, μ_w , and variance, σ_w^2 , are the additive noise and independent each other over n . When PMP algorithms including Eqs. (1.3), (1.4), and (1.7) are performed to Eq. (1.2) which are noise free, the computed A^c , B^c , and ϕ are treated as their true values and are $A^c = \alpha \left[\frac{1}{2}\alpha_p + \beta_p + \beta \right] + \beta$, $B^c = \frac{1}{2}\alpha\alpha_p$, and $\phi = \arctan[\sin(\phi)/\cos(\phi)]$. But if those PMP algorithms are applied to Eq. (3.10) which are polluted by noise, the computed A^c , B^c , and ϕ are also corrupted by term w_n .

The noised A^c , notated by \tilde{A}^c and computed by Eq. (1.3), is

$$\tilde{A}^c = A^c + \frac{1}{N} \sum_{n=0}^{N-1} (w_n), \quad (3.11)$$

and its absolute error, defined as $\Delta A^c = A^c - \tilde{A}^c$, is

$$\Delta A^c = -\frac{1}{N} \sum_{n=0}^{N-1} (w_n), \quad (3.12)$$

which is a linear combination of w_n . The mean and variance of ΔA^c are easily derived, respectively, as

$$\mu_{\Delta A^c} = -\mu_w \quad (3.13)$$

and

$$\sigma_{\Delta A^c}^2 = \frac{1}{N} \sigma_w^2. \quad (3.14)$$

With such a simple form, the term ΔA^c is useful for measuring noise level, whatever the distribution of the noise is, of a SLI system by taking advantage of the relationship

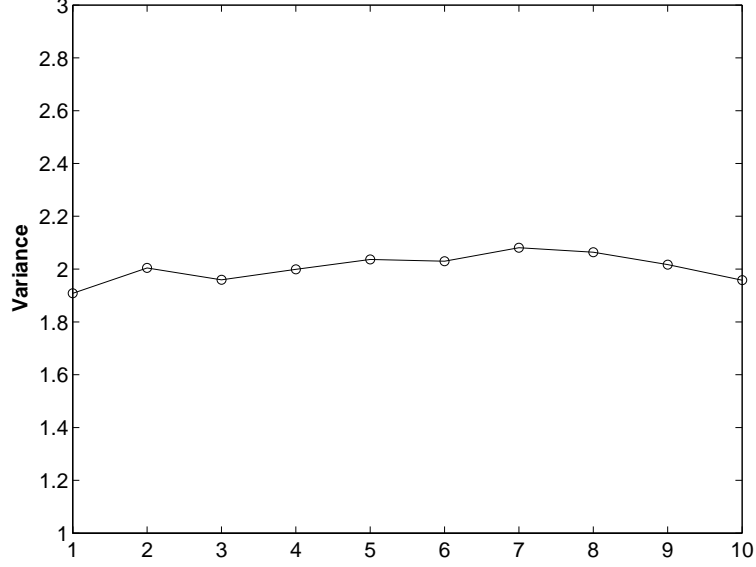


Figure 3.1: With $w_n \sim N(0, 2.0)$ and $N_1 = N_2 = 3$, the averaged σ_w^2 over 10 measurements is 2.0026.

between $\sigma_{\Delta A^c}^2$ and σ_w^2 in Eq. (3.14). However, in practice, it is not easy to obtain the true A^c , although a very good approximation can be found by averaging a large collection of measurements.

In this chapter, a trade-off and low-cost solution is proposed as following. First, we scan an object twice with the same or different number of patterns, N_1 and N_2 respectively; second, \tilde{A}_1^c and \tilde{A}_2^c are computed by Eq. (1.3) respectively as

$$\tilde{A}_1^c = A^c + \frac{1}{N_1} \sum_{n_1=0}^{N_1-1} w_{n_1} \quad (3.15)$$

and

$$\tilde{A}_2^c = A^c + \frac{1}{N_2} \sum_{n_2=0}^{N_2-1} w_{n_2}; \quad (3.16)$$

third, the difference between \tilde{A}_1^c and \tilde{A}_2^c is computed as

$$\Delta A_{12}^c = \frac{1}{N_1} \sum_{n_1=0}^{N_1-1} w_{n_1} - \frac{1}{N_2} \sum_{n_2=0}^{N_2-1} w_{n_2}, \quad (3.17)$$

which indicates

$$\sigma_{\Delta A_{12}^c}^2 = \frac{1}{N_1} \sigma_w^2 + \frac{1}{N_2} \sigma_w^2, \quad (3.18)$$

where $\sigma_{\Delta A_{12}^c}^2$ is the variance of ΔA_{12}^c ; and finally, the variance of w_n , σ_w^2 , can be solved as

$$\sigma_w^2 = \left(\frac{N_1 N_2}{N_1 + N_2} \right) \sigma_{\Delta A_{12}^c}^2. \quad (3.19)$$

Nonlinear response or gamma distortion is not considered in this chapter, so if there exists gamma distortion in a SLI system, to obtain the same certain distortion, N_1 had better equal to N_2 , i.e., $N_1 = N_2 = N$, and Eq. (3.19) will become

$$\sigma_w^2 = \frac{1}{2} N \sigma_{\Delta A_{12}^c}^2. \quad (3.20)$$

In our simulation, with $w_n \sim N(0, 2.0)$ and $N_1 = N_2 = 3$, the averaged σ_w^2 over 10 measurements is 2.0026 and each measurement is shown in Fig. 3.1.

If Eqs. (1.5) and (1.6) are applied to Eq. (3.10) respectively, we obtain

$$\tilde{S}_N = B^c \sin(\phi) + \frac{2}{N} \sum_{n=0}^{N-1} \left[w_n \sin \left(\frac{2\pi n}{N} \right) \right] \quad (3.21)$$

and

$$\tilde{C}_N = B^c \cos(\phi) + \frac{2}{N} \sum_{n=0}^{N-1} \left[w_n \cos \left(\frac{2\pi n}{N} \right) \right]. \quad (3.22)$$

Then the noise polluted B^c , notated as \tilde{B}^c , is computed by

$$\tilde{B}^c = \sqrt{\tilde{S}_N^2 + \tilde{C}_N^2} \quad (3.23)$$

$$= \frac{1}{2} \alpha_p \sqrt{(\alpha + X)^2 + Y^2}, \quad (3.24)$$

where

$$X = \frac{4}{N \alpha_p} \sum_{n=0}^{N-1} \left[w_n \cos \left(\phi - \frac{2\pi n}{N} \right) \right] \quad (3.25)$$

and

$$Y = \frac{4}{N\alpha_p} \sum_{n=0}^{N-1} \left[w_n \sin \left(\phi - \frac{2\pi n}{N} \right) \right]. \quad (3.26)$$

The means of X and Y are the same and equal to 0, i.e., $\mu_X = \mu_Y = 0$. The variances of X and Y are the same too and they are derived as

$$\sigma_X^2 = \sigma_Y^2 = \frac{8}{N\alpha_p^2} \sigma_w^2, \quad (3.27)$$

which are decreased by increasing N and/or, especially, α_p . For example, with $N = 3$ and $\alpha_p = 255$, the variance of X or Y is 24,384 times less than the variance of w_n . The correlation coefficient of X and Y , notated as ρ_{XY} , is 0, which means X and Y are uncorrelated; and furthermore, if w_n is Gaussian, which makes X and Y be Gaussian too, then X and Y are independent each other.

The noise polluted α , notated as $\tilde{\alpha}$ and computed by Eq. (3.6) with \tilde{B}^c , is

$$\tilde{\alpha} = \sqrt{(\alpha + X)^2 + Y^2}. \quad (3.28)$$

Its absolute error, defined as $\Delta\alpha = \alpha - \tilde{\alpha}$, is expressed as

$$\Delta\alpha = \alpha - \sqrt{(\alpha + X)^2 + Y^2}. \quad (3.29)$$

Correspondingly, the noisy ϕ , notated as $\tilde{\phi}$, is computed by

$$\tilde{\phi} = \arctan \left(\frac{\tilde{S}_N}{\tilde{C}_N} \right) \quad (3.30)$$

and its absolute error, defined as $\Delta\phi = \phi - \tilde{\phi}$, is expressed as

$$\Delta\phi = \arctan \left(\frac{Y}{\alpha + X} \right). \quad (3.31)$$

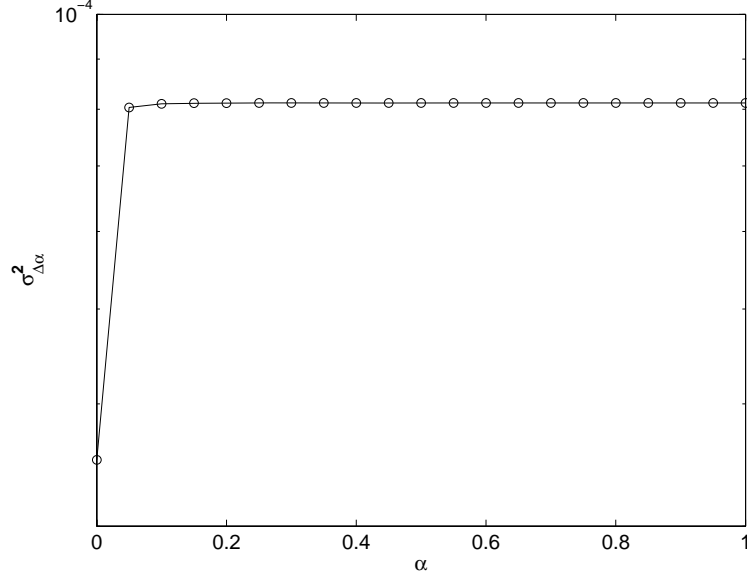


Figure 3.2: With $w_n \sim N(0, 2.0)$, $N = 3$, and $\alpha_p = 255$, the variances of $\Delta\alpha$ versus α varying from 0 to 1 by a step of 0.05, in log scale.

If X and Y are independent each other and are Gaussian respectively, the distribution of $\tilde{\alpha}$ or $\Delta\alpha$ is Rician whose probability density function (PDF) is complicated [8]. The PDF of phase error $\Delta\phi$ is complicated too and had been discussed in [8, 7, 117].

If we write a complex number as $Z = (\alpha + X) + jY$, where $j = \sqrt{-1}$, obviously $\tilde{\alpha}$ is the magnitude of Z and $\Delta\phi$ is the angle of Z . By means of $\tilde{\alpha}$ and $\Delta\phi$, the real part and imaginary part of Z can be expressed as

$$\tilde{\alpha} \cos(\Delta\phi) = \alpha + X \quad (3.32)$$

and

$$\tilde{\alpha} \sin(\Delta\phi) = Y. \quad (3.33)$$

If $\Delta\phi$ is small, there are approximations as $\cos(\Delta\phi) \approx 1$ and $\sin(\Delta\phi) \approx \Delta\phi$. Then Eqs. (3.32) and (3.33) become

$$\tilde{\alpha} \approx \alpha + X \quad (3.34)$$

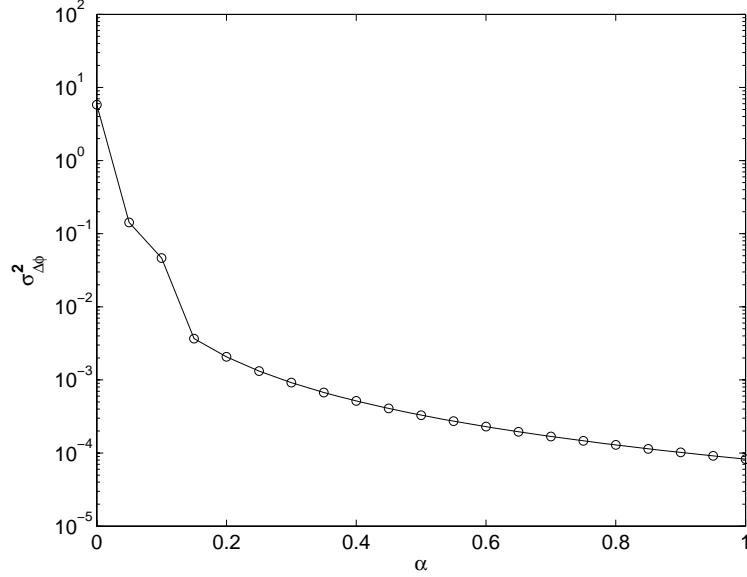


Figure 3.3: With $w_n \sim N(0, 2.0)$, $N = 3$, and $\alpha_p = 255$, the variances of $\Delta\phi$ versus α varying from 0 to 1 by a step of 0.05, in log scale.

and

$$\tilde{\alpha}\Delta\phi \approx Y. \quad (3.35)$$

From Eq. (3.34), the absolute error of α is re-derived as

$$\Delta\alpha = \alpha - \tilde{\alpha} \approx -X, \quad (3.36)$$

which has the mean $-\mu_X$ and variance σ_X^2 . So $\tilde{\alpha}$ can be employed to estimate α robustly and it is $\tilde{\alpha} \approx \alpha$. With the simplified Eq. (3.34), we do not require that X and Y should be independent each other and be Gaussian distributed. Figure 3.2 shows, with $w_n \sim N(0, 2.0)$, $N = 3$, and $\alpha_p = 255$, the variances of $\Delta\alpha$ versus α varying from 0 to 1 by a step of 0.05. It is seen that $\sigma_{\Delta\alpha}^2$ is very stable with the change of α .

From Eqs. (3.34) and (3.35), the absolute error of ϕ is re-derived as

$$\Delta\phi \approx \frac{Y}{\tilde{\alpha}} \approx \frac{Y}{\alpha} = \frac{4}{N\alpha\alpha_p} \sum_{n=0}^{N-1} \left[w_n \sin\left(\phi - \frac{2\pi n}{N}\right) \right], \quad (3.37)$$

which is consistent with the result in [9]. The mean of $\Delta\phi$ is 0 and the variance of $\Delta\phi$ is given by

$$\sigma_{\Delta\phi}^2 \approx \frac{8}{N\alpha^2\alpha_p^2}\sigma_w^2. \quad (3.38)$$

The phase error is decreased by increasing N , α_p and α . For a SLI system, if N and α_p are fixed, the phase quality will mostly depend on the reflectivity, α , of scanned object. From this view, the phase quality is very sensitive to α . Figure 3.3 shows, with $w_n \sim N(0, 2.0)$, $N = 3$, and $\alpha_p = 255$, the variances of $\Delta\phi$ versus α varying from 0 to 1 by a step of 0.05. It is seen that $\sigma_{\Delta\phi}^2$ is very sensitive to change of α . The higher the α , the smaller the $\sigma_{\Delta\phi}^2$;

To compute the 3-D coordinates of the scanned object, one direction of normalized projector coordinates, y^p , should be obtained by $y^p = \phi/(2\pi f)$, so the absolute error of y^p , defined as $\Delta y^p = y^p - \tilde{y}^p$, is described as

$$\Delta y^p \approx \frac{2}{\pi N\alpha\alpha_p f} \sum_{n=0}^{N-1} \left[w_n \sin \left(\phi - \frac{2\pi n}{N} \right) \right]. \quad (3.39)$$

The mean of Δy^p is 0 and the variance of Δy^p is given by

$$\sigma_{\Delta y^p}^2 \approx \frac{2}{\pi^2 N\alpha^2\alpha_p^2 f^2} \sigma_w^2. \quad (3.40)$$

The error for the 3-D coordinates of the scanned object was presented in [9].

Finally when we compute the ambient light intensity with Eq. (3.5), the noised β , notated as $\tilde{\beta}$, is $\tilde{\beta} = [\tilde{A}^c - \tilde{\alpha}(0.5\alpha_p + \beta_p)]/(\tilde{\alpha} + 1)$ and its absolute error, defined as $\Delta\beta = \beta - \tilde{\beta}$, is expressed as

$$\Delta\beta \approx \frac{1}{\alpha + 1} \Delta A^c - \frac{0.5\alpha_p + \beta_p + \beta}{\alpha + 1} \Delta\alpha \quad (3.41)$$

with mean $\mu_{\Delta\beta} \approx \mu_w/(\alpha + 1)$ and variance

$$\sigma_{\Delta\beta}^2 \approx \frac{1}{N(\alpha + 1)^2} \left\{ 2 \left[1 + \frac{2(\beta_p + \beta)}{\alpha_p} \right]^2 + 1 \right\} \sigma_w^2, \quad (3.42)$$

which means we had better employ a large N and a target with high reflectivity, α , to calibrate the ambient light intensity more accurately.

3.2 Phase channel multiplexing pattern strategy

In the previous section, we analyzed the basic parameters in PMP technique and the effects of additive noise. In this section, we will discuss how to embed auxiliary signal used for phase unwrapping into the main signal based on the analysis of sinusoid wave harmonics [118]. The methods of noise analysis employed in this section is similar to them in the previous section.

Suppose we have a group of phase-shifted sinusoid wave signals, mixed with harmonics, defined as

$$I_n = A + B \cos \left(\phi - \frac{2\pi n}{N} \right) + \sum_{k=2}^{\infty} \left\{ B_k \cos \left[k \left(\phi_k - \frac{2\pi n}{N} \right) \right] \right\}, \quad (3.43)$$

where N is total number of the signals and ≥ 3 , n is phase-shift index, A is the basic direct component (DC) of the signals, $\cos(\phi - 2\pi n/N)$ is the main signal with phase ϕ and energy B , and $\cos[k(\phi - 2\pi n/N)]$ are the harmonics with phase ϕ_k and energy B_k . Depending on the number of the signals, N , one phase channel is shared by lots of harmonics. The two basic phase channel are the DC channel and the main channel in which the main signal lives.

When we apply Eq (1.7) to Eq. (3.43) to compute the phase of main signal, ϕ , a harmonics distorted phase will be obtained as

$$\tilde{\phi} = \arctan \left[\frac{B \sin(\phi) + H_s}{B \cos(\phi) + H_c} \right], \quad (3.44)$$

where

$$H_s = \sum_{k=1}^{\infty} \{B_{kN+1} \sin [(kN + 1) \phi_{kN+1}]\} - \sum_{k=1}^{\infty} \{B_{kN-1} \sin [(kN - 1) \phi_{kN-1}]\} \quad (3.45)$$

and

$$H_c = \sum_{k=1}^{\infty} \{B_{kN+1} \cos [(kN + 1) \phi_{kN+1}]\} + \sum_{k=1}^{\infty} \{B_{kN-1} \cos [(kN - 1) \phi_{kN-1}]\}. \quad (3.46)$$

To get a distortion-free main signal ϕ , the harmonics, which share the main phase channel with the main signal, must be suppressed to 0 through setting all the energy $B_{kN\pm 1}$ ($k \geq 1$) to zero.

By doing so, the signals described in Eq. (3.43) will be simplified as

$$I_n = A + B \cos \left(\phi - \frac{2\pi n}{3} \right) + \sum_{k=1}^{\infty} [B_{3k} \cos (3k\phi_{3k})] \quad (3.47)$$

for $N = 3$,

$$I_n = A + B \cos \left(\phi - \frac{\pi n}{2} \right) + \sum_{k=0}^{\infty} \{B_{2+4k} \cos [(2 + 4k) \phi_{2+4k} - \pi n]\} + \sum_{k=1}^{\infty} [B_{4k} \cos (4k\phi_{4k})] \quad (3.48)$$

for $N = 4$, or

$$I_n = A + B \cos \left(\phi - \frac{2\pi n}{5} \right) + \sum_{k=2, k \neq 5m \pm 1}^{\infty} \left\{ B_k \cos \left[k \left(\phi_k - \frac{2\pi n}{5} \right) \right] \right\} \quad (3.49)$$

for $N = 5$. Obviously in some phase channels, many non-zero harmonics are still remained, and if we only need one additional signal in the different phase channel

from the main phase channel, we need to suppress harmonics furthermore according to different cases of N . For $N = 3$, the only additional and available phase channel is the DC channel, so after we keep the first signal and remove the others in the DC channel, Eq. (3.43) becomes

$$I_n = A + B \cos\left(\phi - \frac{2\pi n}{3}\right) + B_3 \cos(3\phi_3). \quad (3.50)$$

For $N = 4$, besides the DC channel, one more available phase channel is at the phase shift π . Because $\cos(n\pi) = \pm 1$ and $\sin(n\pi) = 0$, we call this channel as half phase channel. When only the main signal and the first harmonic signal in the half phase channel are kept, Eq. (3.43) becomes

$$I_n = A + B \cos\left(\phi - \frac{\pi n}{2}\right) + B_2 \cos(2\phi_2 - \pi n). \quad (3.51)$$

Finally for $N = 5$, there is a full phase channel next to the main phase channel at the phase shift 0.8π and we call that channel as second full phase channel. When only the main signal and the first signal in the second full phase channel are kept, Eq. (3.43) becomes

$$I_n = A + B \cos\left(\phi - \frac{2\pi n}{5}\right) + B_2 \cos\left(2\phi_2 - \frac{4\pi n}{5}\right). \quad (3.52)$$

In the paper, our proposed pattern strategies are based on Eqs. (3.50), (3.51) and (3.52) according to the different cases of N and all of them are called phase channel multiplexing pattern (PCMP).

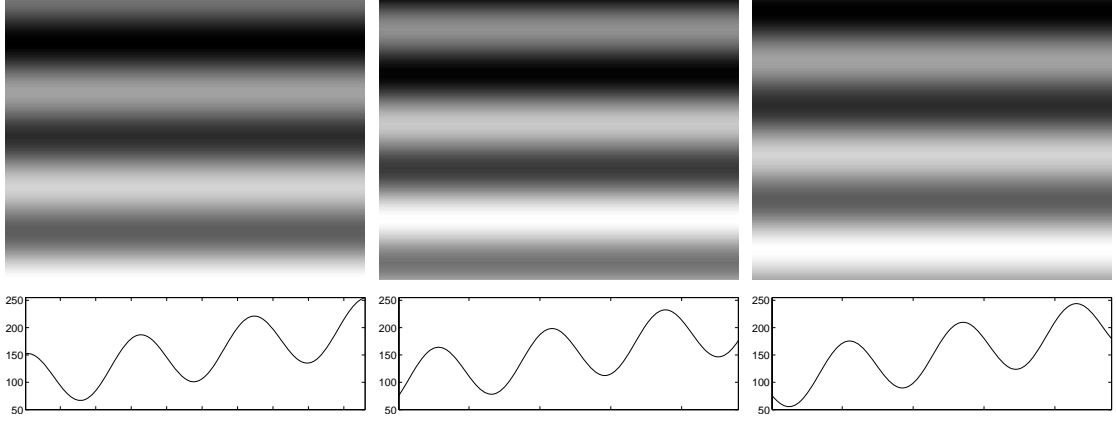


Figure 3.4: Proposed 3-pattern PCMP with $f_h = 3$, $\alpha_p = 200$, $\beta_p = 55$, $c_1 = 0.5$, $c_2 = 0.5$, and $R(y^p) = 2y^p - 1$ (top) and the cross-section of each pattern (bottom).

N=3

When the number of patterns is 3, taking advantage of the features Eq. (3.50), we design the projected patterns as

$$I_n^p = \alpha_p \left[\frac{1}{2} + \frac{1}{2}c_1 \cos \left(2\pi f_h y^p - \frac{2\pi n}{3} \right) + \frac{1}{2}c_2 R(y^p) \right] + \beta_p, \quad (3.53)$$

where y^p is the normalized projector coordinates with range $[0, 1]$, α_p is the amplitude of the pattern, β_p is the minimum value of the pattern, and c_1 and c_2 are modulation coefficients of main signal and reference signal respectively. The terms c_1 and c_2 are related through $c_1 + c_2 = 1$. $R(y^p)$ is the reference signal and it can be any monotonic function with the value range $[-1, 1]$ over the domain of y^p . Figure 3.4 shows a cross-section of proposed PCMP for $N = 3$ with $n = 0$, $f_h = 3$, $\alpha_p = 200$, $\beta_p = 55$, $c_1 = 0.5$, $c_2 = 0.5$, and $R(y^p) = 2y^p - 1$.

The captured patterned images by the camera are expressed by

$$I_n^c = A^c + B^c \cos \left(\phi_h - \frac{2\pi n}{3} \right), \quad (3.54)$$

where A^c , B^c and ϕ_h can be computed by Eq. (1.3), (1.4) and (1.7) respectively.

Equation. (3.54) also can be written as

$$I_n^c = \alpha \left\{ \alpha_p \left[\frac{1}{2} + \frac{1}{2} c_1 \cos \left(\phi_h - \frac{2\pi n}{3} \right) + \frac{1}{2} c_2 R(\phi_u) \right] + \beta_p + \beta \right\} + \beta, \quad (3.55)$$

where ϕ_h is the wrapped high-quality phase, and ϕ_u is the coarse unit-frequency phase used for unwrapping. With the parameters in Eq. (3.55), A^c and B^c are expressed as

$$A^c = \alpha \left\{ \alpha_p \left[\frac{1}{2} + \frac{1}{2} c_2 R(\phi_u) \right] + \beta_p + \beta \right\} + \beta \quad (3.56)$$

and

$$B^c = \frac{1}{2} \alpha \alpha_p c_1. \quad (3.57)$$

Then the reference signal, $R(\phi_u)$, containing the coarse unit-frequency phase ϕ_u can be derived according to

$$R(\phi_u) = \frac{1}{c_2} \left[\frac{2(A^c - \beta)}{\alpha \alpha_p} - \frac{2(\beta_p + \beta)}{\alpha_p} - 1 \right], \quad (3.58)$$

where

$$\alpha = \frac{2B^c}{\alpha_p c_1} \quad (3.59)$$

and β is calibrated by traditional PMP patterns using Eq. (3.5). Once ϕ_u is solved by the inverse function of $R(\cdot)$, phase unwrapping can be performed for ϕ_h .

If there exists additive noise, w_n , in the scanning system, the patterned images captured by the camera will be

$$\tilde{I}_n^c = I_n^c + w_n, \quad (3.60)$$

where I_n^c is defined in Eq. (3.55) and, with the same mean μ_w and variance σ_w^2 , w_n are the additive noise and independent one another. Similar to the noise analysis for

PMP in the previous section, the absolute phase error for the wrapped high-frequency phase, defined as $\Delta\phi_h = \phi_h - \tilde{\phi}_h$, is expressed as

$$\Delta\phi_h \approx \frac{4}{3\alpha\alpha_p c_1} \sum_{n=0}^2 \left[w_n \sin \left(\phi - \frac{2\pi n}{3} \right) \right] \quad (3.61)$$

and its corresponding error of y^p is

$$\Delta y^p \approx \frac{2}{3\pi\alpha\alpha_p c_1 f_h} \sum_{n=0}^2 \left[w_n \sin \left(\phi - \frac{2\pi n}{3} \right) \right], \quad (3.62)$$

whose variance is given by

$$\sigma_{\Delta y^p}^2 \approx \frac{2}{3\pi^2\alpha^2\alpha_p^2 c_1^2 f_h^2} \sigma_w^2. \quad (3.63)$$

When we investigate Eq. (3.40), with $f = 1$ and $N = 3$, and Eq. (3.63), to achieve better performance compared with unit-frequency 3-pattern PMP, the coefficient c_1 in Eq. (3.53) should be satisfied with

$$\frac{1}{f_h} < c_1 < 1, \quad (3.64)$$

where f_h is an integer and ≥ 2 . It dose not mean the larger the c_1 , the better the final result, because a larger c_1 will cause a smaller c_2 , and a smaller c_2 will make the quality of ϕ_u worse, which finally increases the error of phase unwrapping. On the other hand, c_1 should not be too small, because the computation of α depends on c_1 and the quality of α will effect the computation of $R(\phi_u)$.

The noise polluted reference signal $R(\phi_u)$, notated as $\tilde{R}(\phi_u)$, is

$$\tilde{R}(\phi_u) = \frac{1}{c_2} \left[\frac{2(\tilde{A}^c - \beta)}{\tilde{\alpha}\alpha_p} - \frac{2(\beta_p + \beta)}{\alpha_p} - 1 \right], \quad (3.65)$$

where \tilde{A}^c is the noised A^c and the variance of its absolute error is $\sigma_{\Delta A^c}^2 = \sigma_w^2/3$, and $\tilde{\alpha}$ is the noised α and the variance of its absolute error approximates to $\sigma_{\Delta\alpha}^2 \approx$

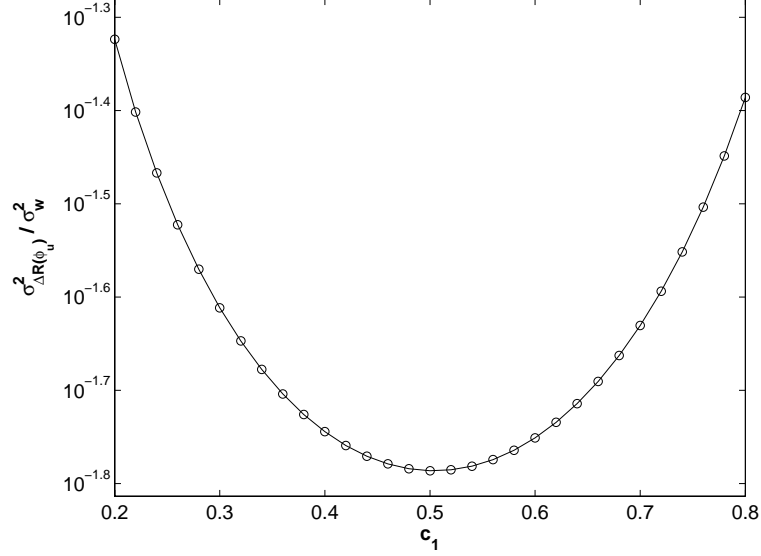


Figure 3.5: Normalized variance of the error of reference signal versus the coefficient c_1 for $N = 3$, in log scale.

$8\sigma_w^2/(3\alpha_p^2c_1^2)$. Then the absolute error of $\tilde{R}(\phi_u)$, defined as $\Delta R(\phi_u) = R(\phi_u) - \tilde{R}(\phi_u)$, is

$$\Delta R(\phi_u) \approx \frac{2}{\alpha\alpha_p c_2} \Delta A^c - \frac{1}{\alpha} \left[\frac{1}{c_2} + \frac{2(\beta_p + \beta)}{\alpha_p c_2} + R(\phi_u) \right] \Delta\alpha \quad (3.66)$$

with a normalized variance as

$$\sigma_{\Delta R_3}^2 = \frac{\sigma_{\Delta R(\phi_u)}^2}{\sigma_w^2} \approx \frac{4}{3\alpha^2\alpha_p^2} \left\{ \frac{1}{c_2^2} + \frac{2}{c_1^2} \left[\frac{1}{c_2} + \frac{2(\beta_p + \beta)}{\alpha_p c_2} + R(\phi_u) \right]^2 \right\}. \quad (3.67)$$

There are so many parameters in Eq. (3.67) effect the value of $\sigma_{\Delta R_3}^2$, but the most important one is α_p , because in some cases, the term α_p is the only parameter under our control. If we solve $d\sigma_{\Delta R_3}^2/dc_1 = 0$, then it is found $\sigma_{\Delta R_3}^2$ has a minimum value at $c_1 \approx 0.5$. So the optimized values of c_1 and c_2 are $c_1 = c_2 = 0.5$ in this case, i.e., $N = 3$, to extract the reference signal as good as possible. Figure 3.5 shows the normalized variance, $\sigma_{\Delta R_3}^2$, of the error of reference signal versus the coefficient c_1 with $\alpha_p = 200$ and $R(y^p) = 2y^p - 1$. The minimum value is nearly at $c_1 = 0.5$.

Table 3.1: Percentage of pixels successfully phase unwrapped for $N = 3$ with different f_h and α_p .

α_p	$f_h = 3$	4	6
200	99.19	96.28	85.17
220	99.76	98.86	92.44
240	99.83	99.67	96.85

If we choose $c_1 = 0.5$, then from the quality condition described in Eq. (3.64), the high frequency f_h should be larger than 2. The high frequency can not be much high, because phase unwrapping will fail for the wavelength of high frequency becoming short compared with the noise in reference signal floor [9]. In our simulation, supposing the additive noise w_n are zero mean Gaussian with $\sigma_w^2 = 1.55$ and setting other parameters as $\alpha = 0.5$, $\beta = -7$, $c_1 = c_2 = 0.5$, $R(y^p) = 2y^p - 1$, $\alpha_p = 200$, 220, and 240 respectively, and $f_h = 3$, 4, and 6 respectively, the percentage of pixels successfully phase unwrapped is listed in Table 3.1. It shows that the lower the f_h and the higher the α_p , the more successful the phase unwrapping.

N=4

In the previous subsection, the DC phase channel was employed to embed a reference signal into the main signal. The shortcomings of that method is that we have to calibrate ambient light intensity before scanning and the noise in DC channel in relative heavier. While in the subsection, when the number of patterns is 4, by employing the half phase channel described in Eq. (3.51), the issues arisen from $N = 3$ can be controlled well and the projected patterns are designed as:

$$I_n^p = \alpha_p \left\{ \frac{1}{2} + \frac{1}{2}c_1 \cos \left(2\pi f_h y^p - \frac{\pi n}{2} \right) + \frac{1}{2}c_2 S[R(y^p), 2n, 4] \right\} + \beta_p, \quad (3.68)$$

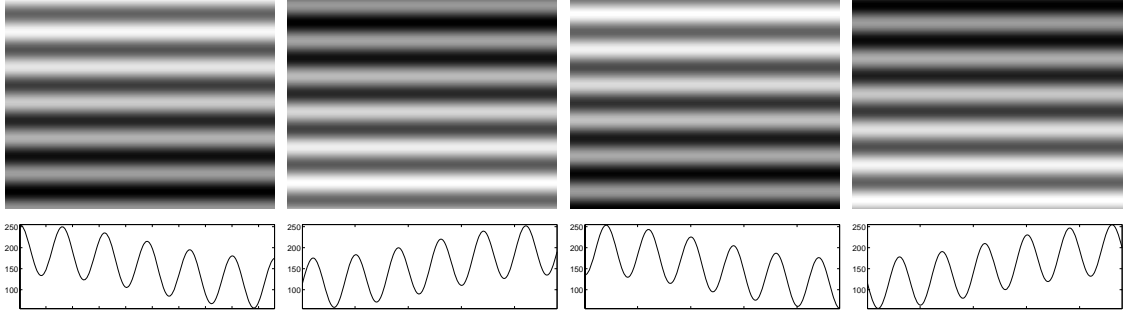


Figure 3.6: Proposed 4-pattern PCMP with $f_h = 6$, $\alpha_p = 200$, $\beta_p = 55$, $c_1 = 0.6$, $c_2 = 0.4$, and $R(y^p) = \cos(\pi y^p)$ (top) and the cross-section of each pattern (bottom).

where $R(y^p)$ is an arbitrary monotonic reference signal, and $S(t, n, N)$ is the phase-shifting function for reference signal and has the same action as $\cos(2\pi ft - 2\pi n/N)$.

Figure 3.6 shows a cross-section of proposed PCMP for $N = 4$ with $n = 0$, $f_h = 6$, $\alpha_p = 200$, $\beta_p = 55$, $c_1 = 0.6$, $c_2 = 0.4$, and $R(y^p) = \cos(\pi y^p)$.

The captured patterned images by the camera are expressed by

$$I_n^c = A^c + B_1^c \cos\left(\phi_h - \frac{\pi n}{2}\right) + B_2^c S[R(y^p), 2n, 4], \quad (3.69)$$

where A^c , B_1^c and ϕ_h can be computed by Eq. (1.3), (1.4) and (1.7) respectively. B_2^c is the modulation for the embedded auxiliary signal in the half phase channel and can not be calculated directly, but in theory, it equals to $B_2^c = B_1^c c_2 / c_1$. The information containing the reference signal in the half phase channel can be computed by

$$B_{cos}^c = \frac{1}{4} \sum_{n=0}^3 [I_n^c \cos(\pi n)]. \quad (3.70)$$

If we write Eq. (3.69) as

$$I_n^c = \alpha \left(\alpha_p \left\{ \frac{1}{2} + \frac{1}{2} c_1 \cos\left(\phi_h - \frac{\pi n}{2}\right) + \frac{1}{2} c_2 S[R(y^p), 2n, N] \right\} + \beta_p + \beta \right) + \beta, \quad (3.71)$$

then B_1^c and B_{cos}^c can be expressed as

$$B_1^c = \frac{1}{2} \alpha \alpha_p c_1 \quad (3.72)$$

and

$$B_{cos}^c = \frac{1}{2}\alpha\alpha_p c_2 R(\phi_u), \quad (3.73)$$

so the reference signal can be solved by

$$R(\phi_u) = \frac{2B_{cos}^c}{\alpha\alpha_p c_2}, \quad (3.74)$$

where $\alpha = 2B_1^c/(\alpha_p c_1)$. Once ϕ_u is obtained by the inverse function of $R(\cdot)$, phase unwrapping for ϕ_h can be achieved.

If there is additive noise in the SLI system, to achieve better performance compared with the unit-frequency 4-pattern PMP, the relationship between f_h and c_1 is the same as it in Eq. (3.64). The noised reference signal, computed by Eq. (3.70) with noised \tilde{I}_n^c , is $\tilde{R}(\phi_u) = 2\tilde{B}_{cos}^c/(\tilde{\alpha}\alpha_p c_2)$, where \tilde{B}_{cos}^c is the noised B_{cos}^c and the variance of its absolute error is $\sigma_{\Delta B_{cos}^c}^2 = 0.25\sigma_w^2$, and $\tilde{\alpha}$ is the noised α and the variance of its absolute error approximates to $\sigma_{\Delta\alpha}^2 \approx 2\sigma_w^2/(\alpha^2 c_1^2)$. The absolute error of $\tilde{R}(\phi_u)$ is

$$\Delta R(\phi_u) \approx \frac{2}{\alpha\alpha_p c_2} \Delta B_{cos}^c - \frac{R(\phi_u)}{\alpha} \Delta\alpha, \quad (3.75)$$

with a normalized variance as

$$\sigma_{\Delta R_4}^2 = \frac{\sigma_{\Delta R(\phi_u)}^2}{\sigma_w^2} \approx \frac{1}{\alpha^2 \alpha_p^2} \left[\frac{1}{c_2^2} + \frac{2R^2(\phi_u)}{c_1^2} \right], \quad (3.76)$$

which is mostly effected by α_p .

If we solve $d\sigma_{\Delta R_4}^2/dc_1 = 0$, then it is found $\sigma_{\Delta R_4}^2$ has a minimum value at $c_1 \approx 0.5$. Figure 3.7 shows the normalized variance, $\sigma_{\Delta R_4}^2$, of the error of reference signal versus the coefficient c_1 with $\alpha_p = 200$ and $R(\phi_u) = \cos(\pi y^p)$. The minimum value is nearly at $c_1 = 0.5$. Compared with Fig. 3.5, the term $\sigma_{\Delta R_4}^2$ is nearly $10\times$ smaller than $\sigma_{\Delta R_3}^2$,

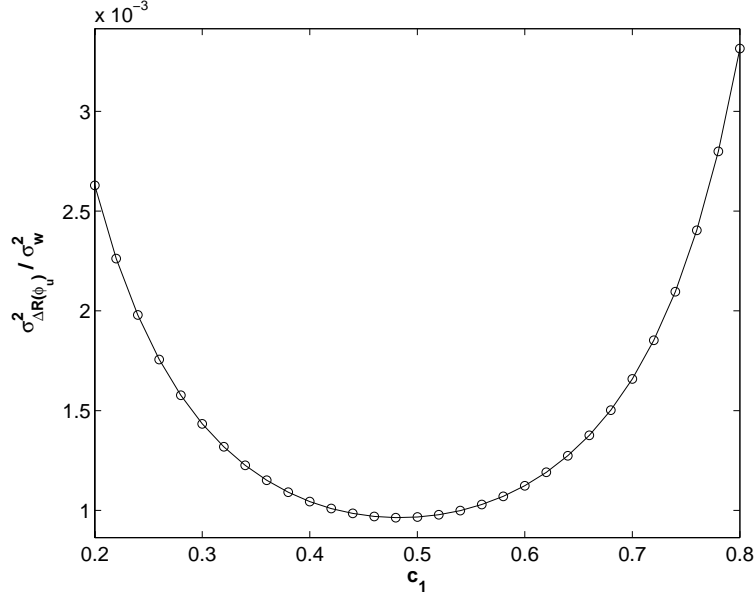


Figure 3.7: Normalized variance of the error of reference signal versus the coefficient c_1 for $N = 4$.

so we can employ a c_1 larger than 0.5 to achieve a much better performance both in phase quality and phase unwrapping. In our simulation, supposing the additive noise w_n are zero mean Gaussian with $\sigma_w^2 = 1.55$ and setting the other parameters as $\alpha = 0.5$, $\beta = -7$, $\alpha_p = 200$, $c_2 = 1 - c_1$, $R(y^p) = \cos(\pi n)$, $c_1 = 0.5, 0.6$, and 0.8 respectively, and $f_h = 6, 8$, and 12 respectively, the percentage of pixels successfully phase unwrapped is listed in Table 3.3.

If Eq. (3.70) is applied to conventional 4-pattern PMP, i.e., Eq. (3.10), both DC

Table 3.2: Percentage of pixels successfully phase unwrapped for $N = 4$ with different f_h and c_1 .

c_1	$f_h = 4$	6	8
0.5	99.79	98.65	96.37
0.6	99.80	98.63	96.30
0.7	99.71	98.15	95.22

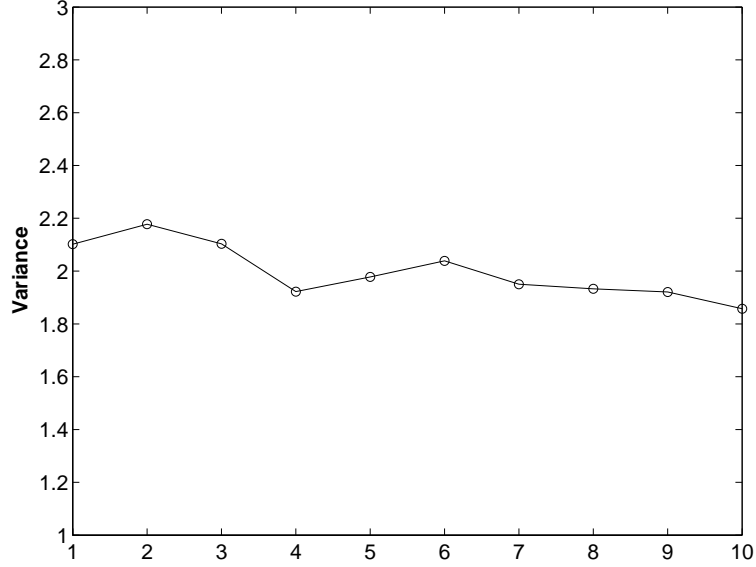


Figure 3.8: With $w_n \sim N(0, 2.0)$ and $N = 4$, the averaged σ_w^2 over 10 measurements is 1.9983.

and AC signal should be canceled and only noise will remain as

$$B_{cos}^c = \frac{1}{4} [(w_0 + w_2) - (w_1 + w_3)], \quad (3.77)$$

with zero mean and variance

$$\sigma_{B_{cos}^c}^2 = \frac{1}{4} \sigma_w^2, \quad (3.78)$$

which can be taken advantage to compute the noise level of the system according to

$$\sigma_w^2 = 4\sigma_{B_{cos}^c}^2. \quad (3.79)$$

In our simulation, with $w_n \sim N(0, 2.0)$ and $N = 4$, the averaged σ_w^2 over 10 measurements is 1.9983 and each measurement is shown in Fig. 3.8.

It should be noticed that the above method of noise measurement requires that there is no gamma distortion, which will be discussed in the later chapter, in the SLI system. Even a very small gamma distortion will cause an inaccurate measurement, and the solution for this situation is similar to the approach of noise measurement

by means of A^c in Eq. (3.20). If there are two measurement of B_{cos}^c , i. e., B_{cos1}^c and B_{cos2}^c , the difference of them is

$$\Delta B_{cos}^c = B_{cos1}^c - B_{cos2}^c = \frac{1}{4} [(w_{10} + w_{12}) - (w_{11} + w_{13}) - (w_{20} + w_{22}) + (w_{21} + w_{23})], \quad (3.80)$$

with zero mean and variance

$$\sigma_{\Delta B_{cos}^c}^2 = \frac{1}{2} \sigma_w^2, \quad (3.81)$$

which indicates the variance of system noise is

$$\sigma_w^2 = 2\sigma_{\Delta B_{cos}^c}^2. \quad (3.82)$$

In the section of experiment, we will show Eq. (3.82) is a robust method, while Eq. (3.79) is not.

N = 5

When the number of patterns is larger than or equal to 5, by taking advantage of Eq. (3.52), we can design the projected patterns as

$$I_n^p = \alpha_p \left[\frac{1}{2} + \frac{1}{2} c_1 \cos \left(2\pi f_h y^p - \frac{2\pi n}{5} \right) + \frac{1}{2} c_2 \cos \left(2\pi y^p - \frac{4\pi n}{5} \right) \right] + \beta_p. \quad (3.83)$$

Because the second full phase channel is employed, the reference signal is a unit-frequency sinusoid wave which can be decoded by an arctangent function more reliably compared to the reference signals employed in the previous subsections. Figure 3.9 shows a cross-section of proposed PCMP for $N = 5$ with $n = 0$, $f_h = 12$, $\alpha_p = 200$, $\beta_p = 55$, $c_1 = 0.7$, and $c_2 = 0.3$.

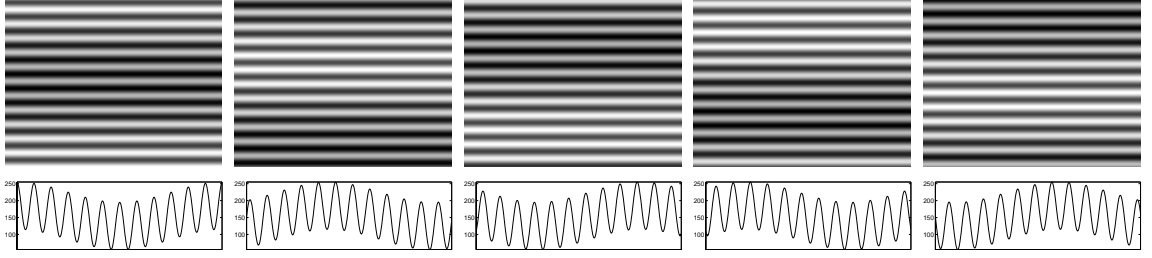


Figure 3.9: Proposed 5-pattern PCMP for with $f_h = 12$, $\alpha_p = 200$, $\beta_p = 55$, $c_1 = 0.7$, and $c_2 = 0.3$ (top) and the cross-section of each pattern (bottom).

Then the captured patterned images in the camera are

$$I_n^c = A^c + B_1^c \cos\left(\phi_h - \frac{2\pi n}{5}\right) + B_2^c \cos\left(\phi_u - \frac{4\pi n}{5}\right), \quad (3.84)$$

where A^c , B_1^c and ϕ_h can be computed by Eq. (1.3), (1.4) and (1.7) respectively. If we let

$$S_{2,N} = \frac{2}{5} \sum_{n=0}^4 \left[I_n^c \sin\left(\frac{4\pi n}{5}\right) \right] \quad (3.85)$$

and

$$C_{2,N} = \frac{2}{5} \sum_{n=0}^4 \left[I_n^c \cos\left(\frac{4\pi n}{5}\right) \right], \quad (3.86)$$

the term B_2^c , the intensity modulation corresponding to ϕ_u , can be derived from

$$B_2^c = \sqrt{S_{2,N}^2 + C_{2,N}^2}, \quad (3.87)$$

and the phase of the reference signal, ϕ_u , is computed by:

$$\phi_u = \arctan\left(\frac{S_{2,N}}{C_{2,N}}\right), \quad (3.88)$$

which will be employed to unwrap ϕ_h . By means of α , α_p , c_1 and c_2 , the terms B_1^c and B_2^c can be respectively expressed as

$$B_1^c = \frac{1}{2} \alpha \alpha_p c_1 \quad (3.89)$$

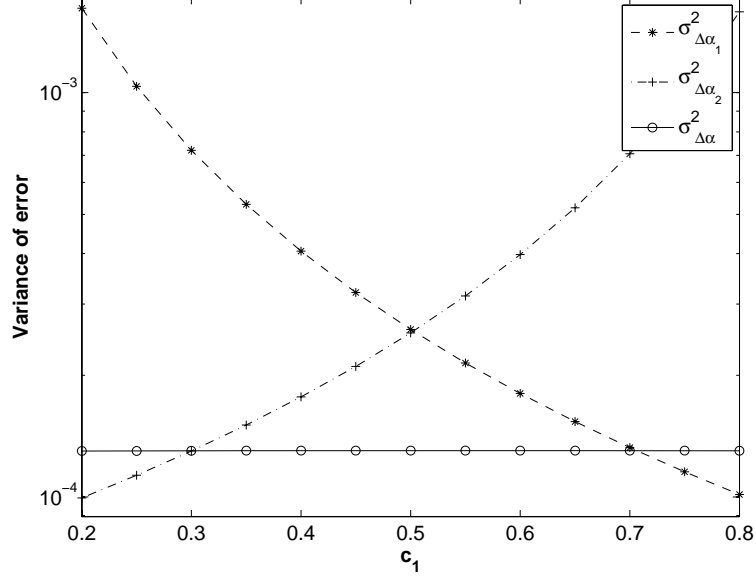


Figure 3.10: With $\sigma_w^2 = 1.6$, $\sigma_{\Delta\alpha_1}^2$, $\sigma_{\Delta\alpha_2}^2$ and $\sigma_{\Delta\alpha}^2$ versus c_1 , in log scale.

and

$$B_2^c = \frac{1}{2}\alpha\alpha_p c_2, \quad (3.90)$$

which indicates B_1^c/B_2^c should equal to c_1/c_2 in theory.

If there exists additive noise, w_n , in the system, to achieve a better performance compared to the unit-frequency 5-pattern PMP, the relationship of f_h and c_1 described in Eq. (3.64) still holds on. Similar to Eq. (3.34), the noised α derived from Eq. (3.89) and Eq. (3.90) respectively, notated as $\tilde{\alpha}_1$ and $\tilde{\alpha}_2$, are expressed as

$$\tilde{\alpha}_1 \approx \alpha + X_1 \quad (3.91)$$

and

$$\tilde{\alpha}_2 \approx \alpha + X_2, \quad (3.92)$$

where

$$X_1 = \frac{4}{5\alpha_p c_1} \sum_{n=0}^4 \left[w_n \cos \left(\phi_h - \frac{2\pi n}{5} \right) \right] \quad (3.93)$$

and

$$X_2 = \frac{4}{5\alpha_p c_2} \sum_{n=0}^4 \left[w_n \cos \left(\phi_u - \frac{4\pi n}{5} \right) \right]. \quad (3.94)$$

The means of X_1 and X_2 are both zero, and the variances of them are

$$\sigma_{X_1}^2 = \frac{8}{5\alpha_p^2 c_1^2} \sigma_w^2 \quad (3.95)$$

and

$$\sigma_{X_2}^2 = \frac{8}{5\alpha_p^2 c_2^2} \sigma_w^2 \quad (3.96)$$

respectively. So the absolute error of $\tilde{\alpha}_1$ is $\Delta\alpha_1 \approx \alpha - \tilde{\alpha}_1 = -X_1$ with variance $\sigma_{\Delta\alpha_1}^2 \approx \sigma_{X_1}^2$ and the absolute error of $\tilde{\alpha}_2$ is $\Delta\alpha_2 \approx \alpha - \tilde{\alpha}_2 = -X_2$ with variance $\sigma_{\Delta\alpha_2}^2 \approx \sigma_{X_2}^2$. As mentioned in the previous subsection, c_1 can neither too large nor too small, so by means of a linear combination of Eqs. (3.91) and (3.92), a weighted and more robust estimation of α can be derived as

$$\tilde{\alpha} \approx c_1 \tilde{\alpha}_1 + c_2 \tilde{\alpha}_2 = \alpha + c_1 X_1 + c_2 X_2. \quad (3.97)$$

Its absolute error is $\Delta\alpha \approx \alpha - \tilde{\alpha} = -c_1 X_1 - c_2 X_2$ with variance

$$\sigma_{\Delta\alpha}^2 \approx \frac{16}{5\alpha_p^2} \sigma_w^2. \quad (3.98)$$

In Fig. 3.10, with $\sigma_w^2 = 1.6$ and c_1 varying from 0.2 to 0.8, $\sigma_{\Delta\alpha_1}^2$, $\sigma_{\Delta\alpha_2}^2$ and $\sigma_{\Delta\alpha}^2$ are shown. It is easy to see $\sigma_{\Delta\alpha}^2$ is very stable when c_1 is changing, which means the estimation of α employing Eq. (3.97) is stable.

By the difference relationship of Eq. (3.91) and (3.92), we have $\Delta\alpha_{12} \approx \tilde{\alpha}_1 - \tilde{\alpha}_2 = X_1 - X_2$ with variance $\sigma_{\Delta\alpha_{12}}^2 \approx 8(c_1^2 + c_2^2)\sigma_w^2/(5\alpha_p^2 c_1^2 c_2^2)$. So the variance of system noise can be estimated by

$$\sigma_w^2 \approx \frac{5}{8} \alpha_p^2 \left(\frac{c_1^2 c_2^2}{c_1^2 + c_2^2} \right) \sigma_{\Delta\alpha_{12}}^2. \quad (3.99)$$

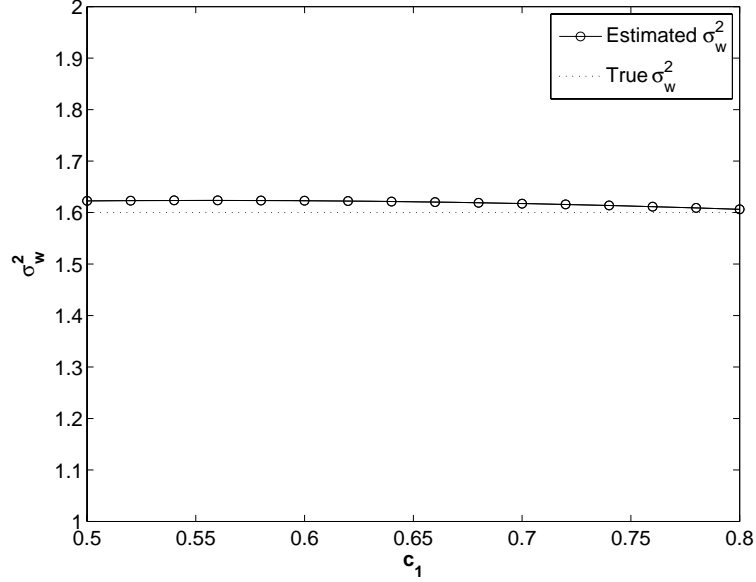


Figure 3.11: For $\sigma_w^2 = 1.6$, the estimated σ_w^2 with c_1 using 5-pattern PCMP.

The meaning of Eq. (3.99) is that, with 5-pattern PCMP, we do not need an additional measurement of system noise and we can roughly estimate the variance of the system noise directly. Figure 3.11 shows the estimated σ_w^2 with c_1 varying from 0.5 to 0.8 for $\sigma_w^2 = 1.6$ using Eq. (3.99).

Similar to Eq.(3.37), the absolute error of the phase of reference signal is

$$\Delta\phi_u \approx \frac{4}{5\alpha\alpha_p c_2} \sum_{n=0}^4 \left[w_n \sin\left(\phi - \frac{4\pi n}{5}\right) \right], \quad (3.100)$$

with variance

$$\sigma_{\Delta\phi_u}^2 \approx \frac{8}{5\alpha^2\alpha_p^2 c_2^2} \sigma_w^2, \quad (3.101)$$

which is increased with decreasing c_2 when α and α_p are fixed. In our simulation, supposing the additive noise w_n are zero mean Gaussian with $\sigma_w^2 = 1.55$ and setting the other parameters as $\alpha = 0.5$, $\beta = -7$, $\alpha_p = 200$, $c_2 = 1 - c_1$, $c_1 = 0.5, 0.6$, and 0.8 respectively, and $f_h = 6, 8$, and 12 respectively, the percentage of pixels successfully phase unwrapped is listed in Table 3.3.

Table 3.3: Percentage of pixels successfully phase unwrapped for $N = 5$ with different f_h and c_1 .

c_1	$f_h = 6$	8	12
0.5	99.61	99.61	99.61
0.6	99.50	99.50	99.49
0.8	98.99	98.95	98.83

3.3 Experiments

The first of two groups of experiments are on system parameter calibrations including ambient intensity calibration and a noise level measurement. The second group of experiments are on the 3-D reconstructions by means of our proposed three kinds of PCMPs. The scanned objects include a white foam board for performance discussion and a textured plastic angel, shown in Fig. 2.2, for effects demonstration.

System parameters calibrations

With Eq. (3.5), we employ classic PMP patterns to calibrate ambient light intensity. The parameters for Eq. (3.1) are $N = 240$, $f = 1$, $\alpha_p = 200$ and $\beta_p = 55$. The calibration target is a white foam board with much higher α at each measurable pixel. The large N and the high α allow us to reduce much measurement error according to Eq. (3.42).

Figure 3.12 shows the histogram of computed β over 133,644 pixels with $\alpha \geq 0.5$. The mean, median and mode values of β over those pixels are -7.17 , -7.22 and -7 respectively. The variance of β is 0.63, which means the ambient light intensity is almost uniformly distributed. We will employ the mode number, -7 , as the intensity of the ambient light in the future. According to Eq. (3.9), with $\beta_p = 55$ and $\beta = -7$,

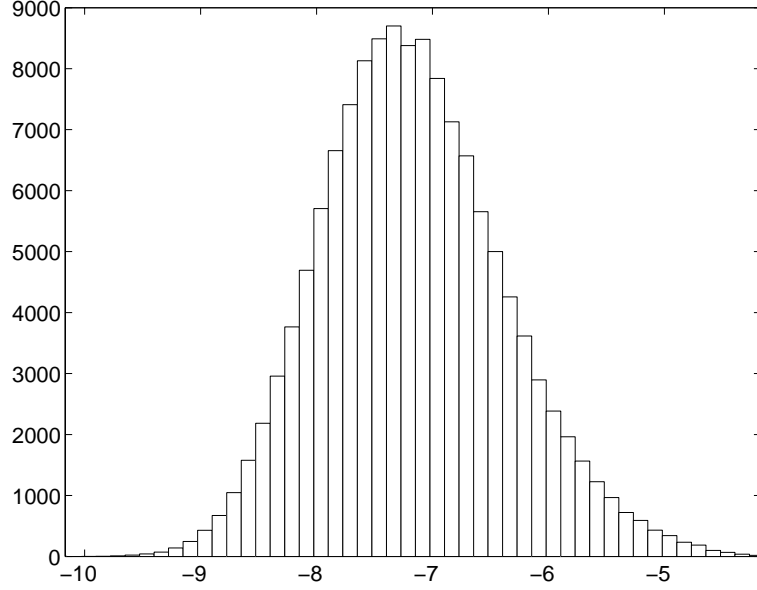


Figure 3.12: The histogram of computed β for the pixels with $\alpha \geq 0.5$

the reliable value of α should be larger than 0.1458. If we only scan an object with uniform texture and high reflectivity, for example, $\alpha > 0.5$, an optimized value of β_p can be 18 according to Eq. (3.7). But for an object with rich texture, such as our angel model, a lot of phase data will be removed for those pixels with $\alpha \leq 0.5$. So we still involved $\beta_p = 55$ and use $\alpha = 0.15$ as the quality indicator for phase in the following experiments.

Taking advantage of Eq. (3.20), we employ 10 groups 3-pattern PMP to measure the variance, σ_w^2 , of our SLI system. The parameters for the projected 3-pattern PMP patterns in Eq. (3.1) are $N = 3$, $f = 1$, $\alpha_p = 200$ and $\beta_p = 55$. A histogram of a measured ΔA^c is shown in Fig. 3.13 (left). Figure 3.13 (right) shows the measured σ_w^2 using any 2 groups of 3-pattern PMP among those 10 groups and there are $\binom{10}{2} = 45$ combinations. The averaged σ_w^2 over 45 measurements is 1.55.

When we employ Eq. (3.79) to measure the level of system noise, the measured

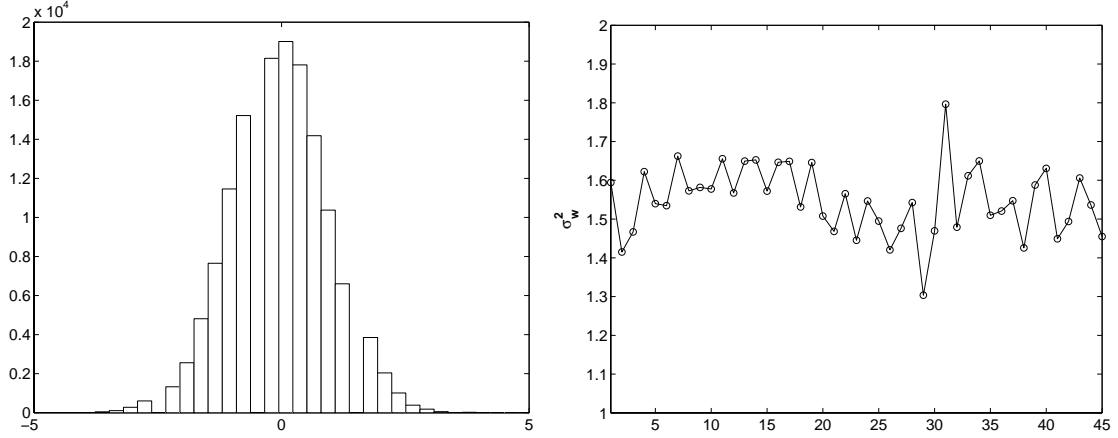


Figure 3.13: Histogram of a measured ΔA^c (left) and all measured σ_w^2 using any 2 groups of 3-pattern PMP among 10 groups (right).

value is around 3.2, which is shown in Fig. 3.14 (left). This result is nearly 2 times as large as the result measured by Eq. (3.20). It is the gamma distortion who makes the measuring error. The cross-section of the B_{cos}^c is shown in Fig. 3.14 (right). Although the gamma distortion is very small, it is still seen the sinusoidal shape in the cross-section curve.

Once Eq. (3.82) is involved to measure the system noise, the measured variance

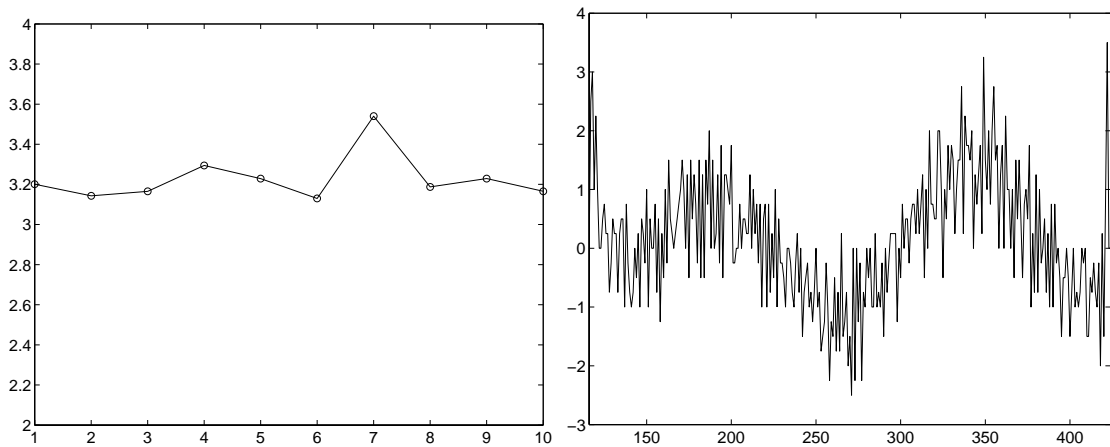


Figure 3.14: Measured σ_w^2 using B_{cos}^c over 10 group of 4-pattern PMP (left) and a cross-section of B_{cos}^c .

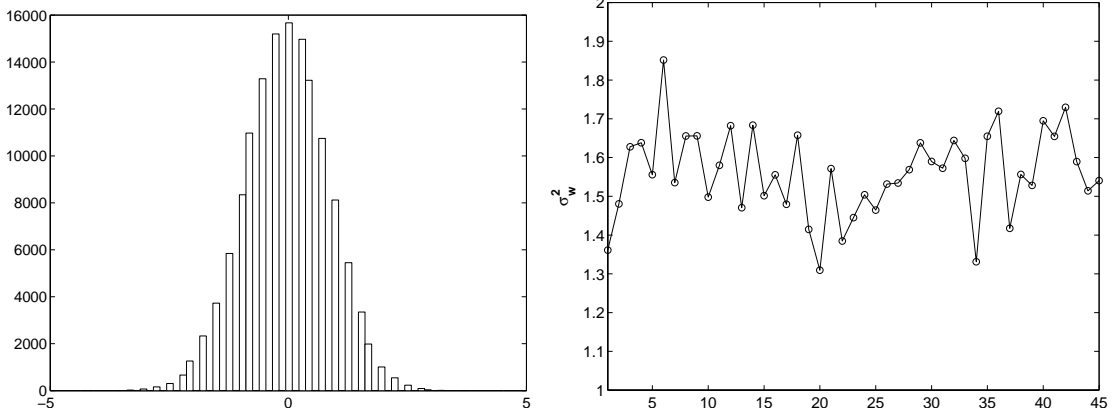


Figure 3.15: Histogram of a measured ΔB_{cos}^c (left) and all measured σ_w^2 using any 2 groups of 4-pattern PMP among 10 groups (right).

of the system is around 1.56 which is almost the same as the result measured by Eq. (3.20). A histogram of a measured ΔB_{cos}^c is shown in Fig. 3.15 (left). Figure 3.15 (right) shows the measured σ_w^2 using any 2 groups of 4-pattern PMP among those 10 groups and there are $\binom{10}{2} = 45$ combinations. When we use Eq. (3.99), the estimated σ_w^2 is 1.95 with $c_1 = 0.5$, 1.85 with $c_1 = 0.6$ and 1.80 with $c_1 = 0.8$.

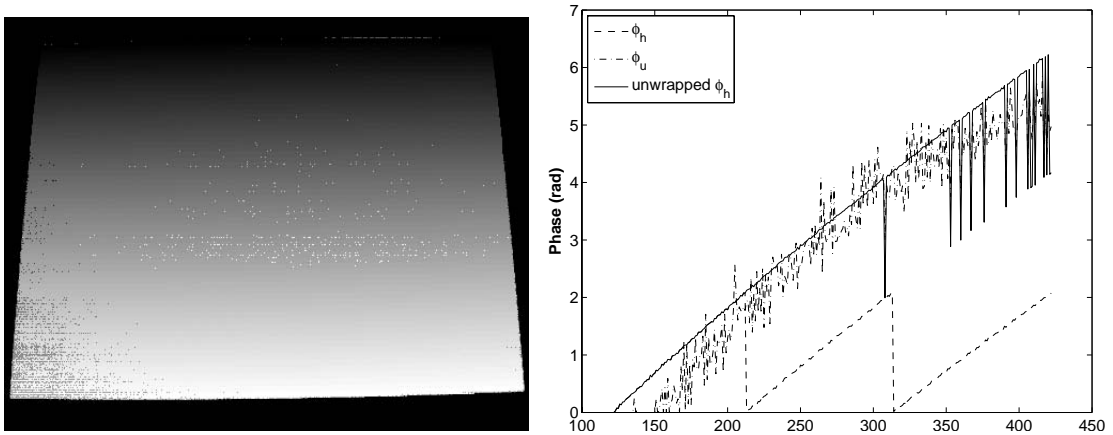


Figure 3.16: Scanned with 3-pattern PCMP, the visualization of unwrapped ϕ_h (left) and the cross-section at 120th column of ϕ_h , ϕ_u , and unwrapped ϕ_h (right) of the board.

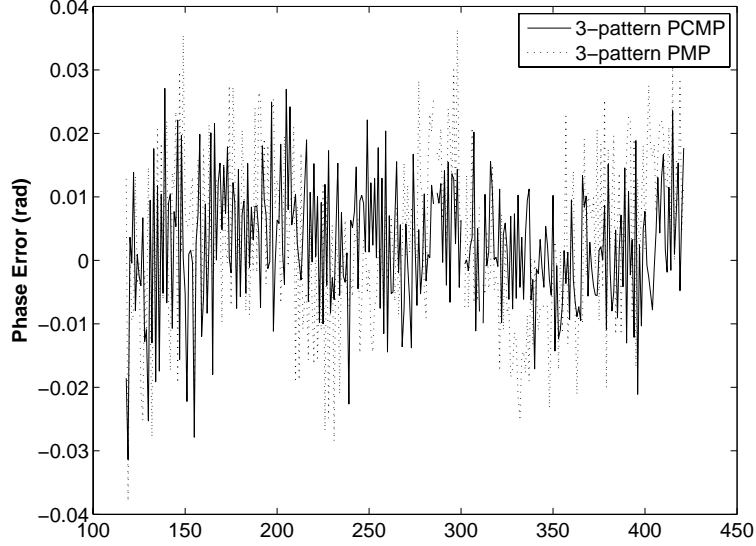


Figure 3.17: Scanned with 3-pattern PCMP and 3-pattern unit-frequency PMP, the cross-section at 320th column of phase error of the board.

PCMP scanning

For 3-pattern PCMP described by Eq. (3.53), the parameters are set as $f_h = 3$, $c_1 = c_2 = 0.5$, $\alpha_p = 200$, $\beta_p = 55$ and $R(y^p) = 2y^p - 1$. When we compute $R(\phi_u)$ with Eq. (3.58), the term $\beta = -7$ obtained from the previous subsection is applied. First we scan the white foam board, and Fig. 3.16 shows the visualization of unwrapped ϕ_h (left) and the cross-section at 120th column of ϕ_h , ϕ_u , and unwrapped ϕ_h (right) of the board. The percentage of pixels successfully unwrapped in this case was 97.61%, which is less than the prediction listed in Table. 3.1, because besides effected by noise, the error of unwrapping is also caused by the non-uniform distributed ambient light intensity which is supposed to be uniform, and such error typically occurs at the edge of the phase image.

For the successfully unwrapped pixels, the variance of absolute error of 3-pattern PCMP is 1.13×10^{-4} , while the variance of the absolute error of 3-pattern PMP

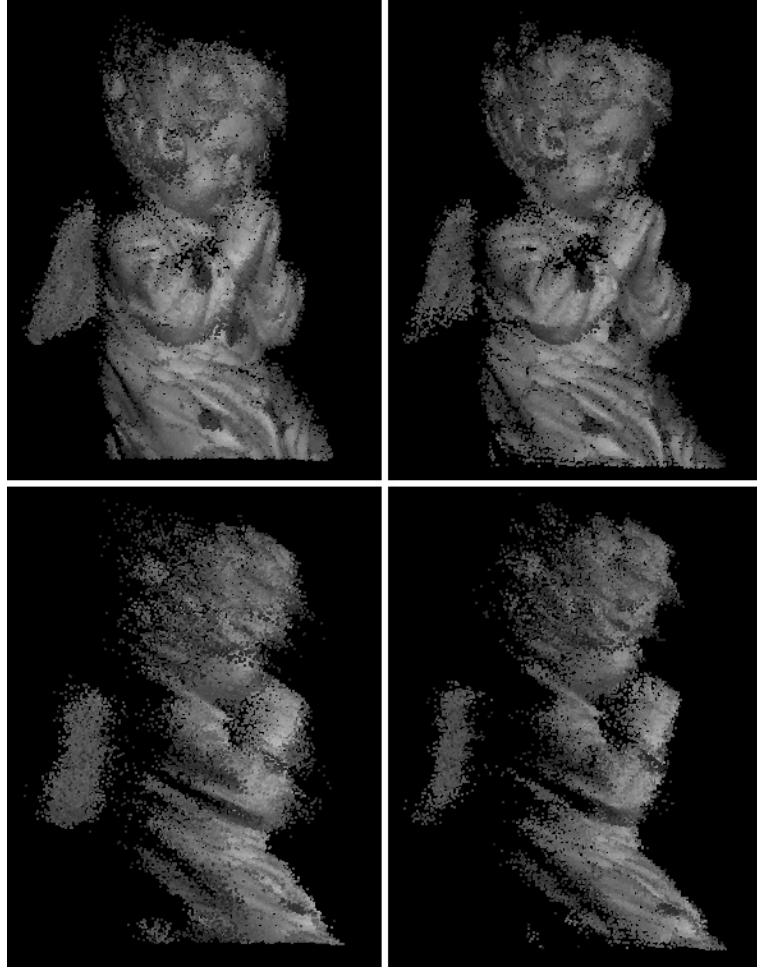


Figure 3.18: Scanned with 3-pattern PMP (left) and PCMP (right), the front view (top) and side view (bottom) of 3-D reconstructed angel.

is 2.43×10^{-4} . The ratio of 2.43×10^{-4} over 1.13×10^{-4} is 2.15, while the ratio of Eq. (3.63) over Eq. (3.40) should be $c_1^2 f_h^2 = 0.5^2 \times 3^2 = 2.25$ in theory. So with the percentage of pixels successfully unwrapped $> 97\%$, the phase quality of 3-pattern PCMP is twice better than 3-pattern unit-frequency PMP. Figure 3.17 shows, scanned with 3-pattern PCMP and 3-pattern unit-frequency PMP, the cross-section at 320th column of phase error of the board. Figure 3.18 shows 3-D point clouds of angel scanned with 3-pattern unit-frequency PMP (left) and 3-pattern PCMP (right) respectively.

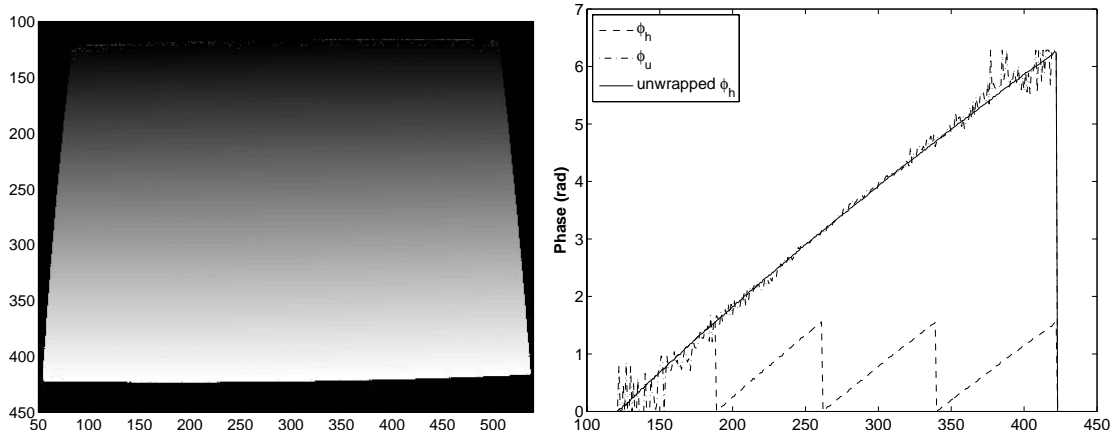


Figure 3.19: Scanned with 4-pattern PCMP, the visualization of unwrapped ϕ_h (left) and the cross-section at 120th column of ϕ_h , ϕ_u , and unwrapped ϕ_h (right) of the board.

For 4-pattern PCMP described by Eq. (3.68), the parameters are set as $c_2 = 1 - c_1$, $\alpha_p = 200$, $\beta_p = 55$, $R(y^p) = \cos(\pi y^p)$, $c_1 = 0.5, 0.6$, and 0.7 respectively, and $f_h = 4, 6$, and 8 respectively. There are 9 groups of scans totally. The term $R(\phi_u)$ is computed with Eq. (3.74), which has nothing to do with the ambient light intensity. First we scan the white foam board, and Fig. 3.19 shows the visualization of unwrapped ϕ_h

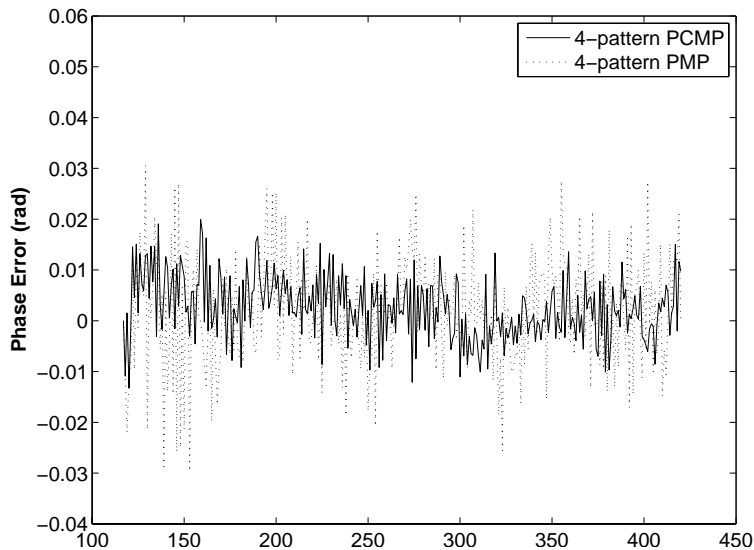


Figure 3.20: Scanned with 4-pattern PCMP and 4-pattern unit-frequency PMP, the cross-section at 320th column of phase error of the board.

Table 3.4: Percentage of pixels successfully unwrapped for 4-pattern PCMP with different f_h and c_1 .

c_1	$f_h = 4$	6	8
0.5	99.86	99.52	96.46
0.6	99.82	99.49	96.35
0.7	99.76	99.38	95.32

(left) and the cross-section at 120th column of ϕ_h , ϕ_u , and unwrapped ϕ_h (right) of the board with $f_h = 4$ and $c_1 = 0.5$, and Fig. 3.20 shows, scanned with 4-pattern PCMP and 4-pattern unit-frequency PMP, the cross-section at 320th column of phase error of the board.

The percentage of pixels successfully phased unwrapped in this case are listed in Table 3.4, which are a little higher than the predictions listed in Table. 3.2 because the averaged α of the board was higher than the 0.5 employed in the simulation. For the successfully unwrapped pixels, the ratios of the variance of absolute error of 4-pattern PCMP over 4-pattern unit-frequency PMP, which is 1.80×10^{-4} , are listed in Table 3.5. Figure 3.21 shows the side views of the 3-D reconstructed point clouds of the angel using 4-pattern unit-frequency PMP (top-1) and 4-pattern PCMP with $c_1 = 0.5$ and $f_h = 4$ (top-2), $c_1 = 0.5$ and $f_h = 6$ (top-3), $c_1 = 0.5$ and $f_h = 8$ (top-4), $c_1 = 0.6$ and $f_h = 4$ (top-5), $c_1 = 0.6$ and $f_h = 6$ (bottom-1), $c_1 = 0.6$ and $f_h = 8$ (bottom-2), $c_1 = 0.7$ and $f_h = 4$ (bottom-3), $c_1 = 0.7$ and $f_h = 6$ (bottom-4), and

Table 3.5: For successfully unwrapped pixels, the ratio of the variance of 4-pattern PCMP over the variance of 4-pattern unit-frequency PMP (experimental measurement/theoretical prediction).

c_1	$f_h = 4$	6	8
0.5	3.47/4.00	7.04/9.00	12.88/16.00
0.6	4.89/5.76	9.77/12.96	20.41/23.04
0.7	7.39/7.84	12.98/17.64	25.93/31.36

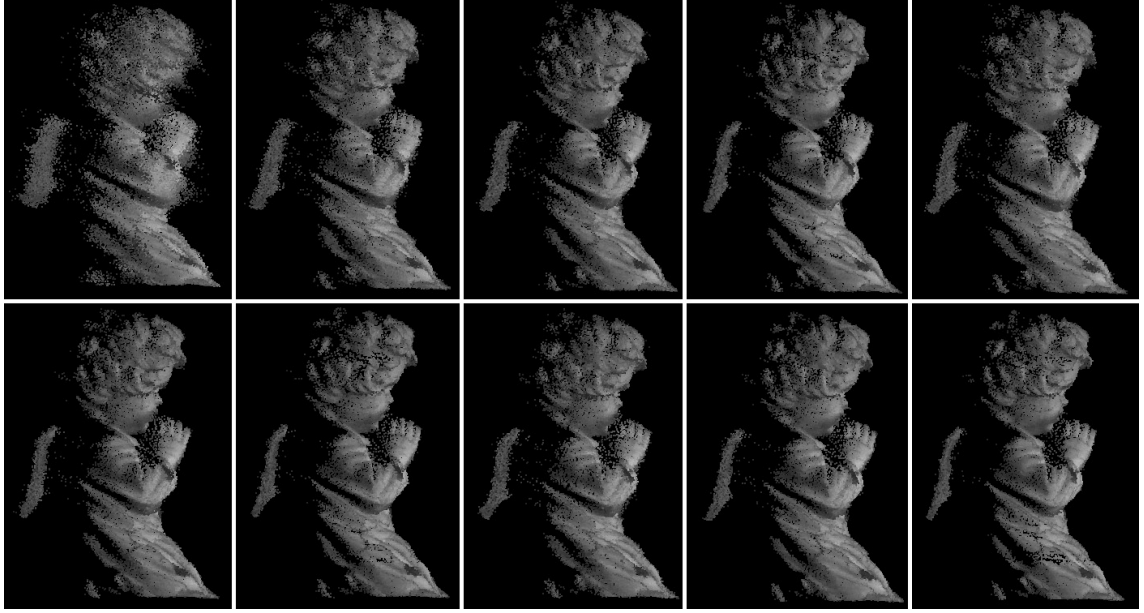


Figure 3.21: Side views of the 3-D reconstructed angel using 4-pattern unit-frequency PMP (top-1) and 4-pattern PCMP with $c_1 = 0.5$ and $f_h = 4$ (top-2), $c_1 = 0.5$ and $f_h = 6$ (top-3), $c_1 = 0.5$ and $f_h = 8$ (top-4), $c_1 = 0.6$ and $f_h = 4$ (top-5), $c_1 = 0.6$ and $f_h = 6$ (bottom-1), $c_1 = 0.6$ and $f_h = 8$ (bottom-2), $c_1 = 0.7$ and $f_h = 4$ (bottom-3), $c_1 = 0.7$ and $f_h = 6$ (bottom-4), and $c_1 = 0.7$ and $f_h = 8$ (bottom-5).

$c_1 = 0.7$ and $f_h = 8$ (bottom-5).

For 5-pattern PCMP described by Eq. (3.83), the parameters are set as $c_2 = 1 - c_1$,

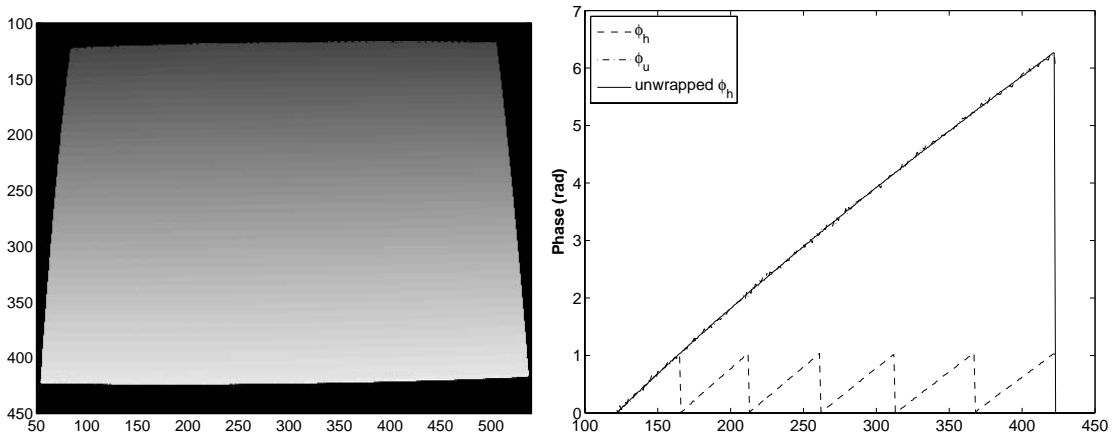


Figure 3.22: Scanned with 5-pattern PCMP, the visualization of unwrapped ϕ_h (left) and the cross-section at 120th column of ϕ_h , ϕ_u , and unwrapped ϕ_h (right) of the board.

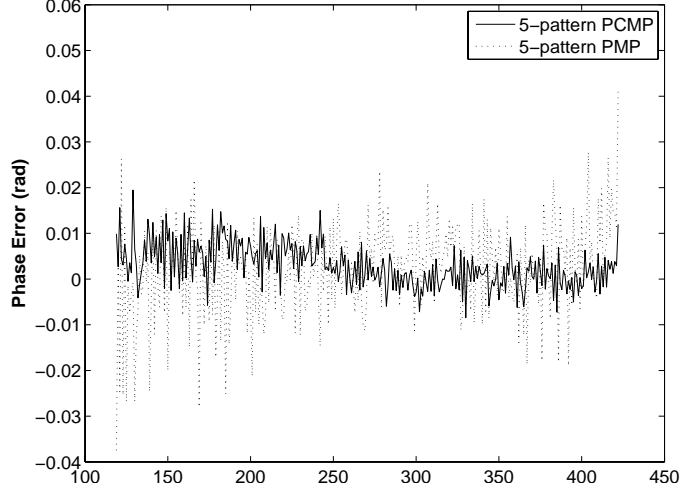


Figure 3.23: Scanned with 5-pattern PCMP and 5-pattern unit-frequency PMP, the cross-section at 320th column of phase error of the board.

$\alpha_p = 200$, $\beta_p = 55$, $c_1 = 0.5, 0.6$, and 0.8 respectively, and $f_h = 6, 8$, and 12 respectively. There are 9 groups of scans totally. First we scan the white foam board, and Fig. 3.22 shows the visualization of unwrapped ϕ_h (left) and the cross-section at 120th column of ϕ_h , ϕ_u , and unwrapped ϕ_h (right) of the board with $f_h = 6$ and $c_1 = 0.5$, and Fig. 3.23 shows, scanned with 5-pattern PCMP and 5-pattern unit-frequency PMP, the cross-section at 320th column of phase error of the board.

The percentage of pixels successfully phase unwrapped, in this case, are listed in Table 3.6, which are nearly the same as the predictions listed in Table. 3.3. For the successfully unwrapped pixels, the ratios of the variance of absolute error of 5-pattern PCMP over 5-pattern unit-frequency PMP, which is 1.53×10^{-4} , are listed

Table 3.6: Percentage of pixels successfully phase unwrapped for 5-pattern PCMP with different f_h and c_1 .

c_1	$f_h = 6$	8	12
0.5	99.77	99.64	99.47
0.6	99.45	99.18	98.93
0.8	99.12	98.99	98.77

Table 3.7: For the successfully unwrapped pixels, the ratio of the variance of 5-pattern PCMP over the variance of 5-pattern unit-frequency PMP (experimental measurement/theoretical prediction).

c_1	$f_h = 6$	8	12
0.5	8.35/9.00	15.27/16.00	32.87/36.00
0.6	12.01/12.96	20.61/23.04	41.94/51.84
0.8	21.33/23.04	36.86/40.96	73.70/92.16

in Table 3.7. Figure 3.24 shows the side views of the 3-D reconstructed point clouds of the angel using 5-pattern unit-frequency PMP (top-1) and 5-pattern PCMP with $c_1 = 0.5$ and $f_h = 6$ (top-2), $c_1 = 0.5$ and $f_h = 8$ (top-3), $c_1 = 0.5$ and $f_h = 12$ (top-4), $c_1 = 0.6$ and $f_h = 6$ (top-5), $c_1 = 0.6$ and $f_h = 8$ (bottom-1), $c_1 = 0.6$ and $f_h = 12$ (bottom-2), $c_1 = 0.8$ and $f_h = 6$ (bottom-3), $c_1 = 0.8$ and $f_h = 8$ (bottom-4), and $c_1 = 0.8$ and $f_h = 12$ (bottom-5).

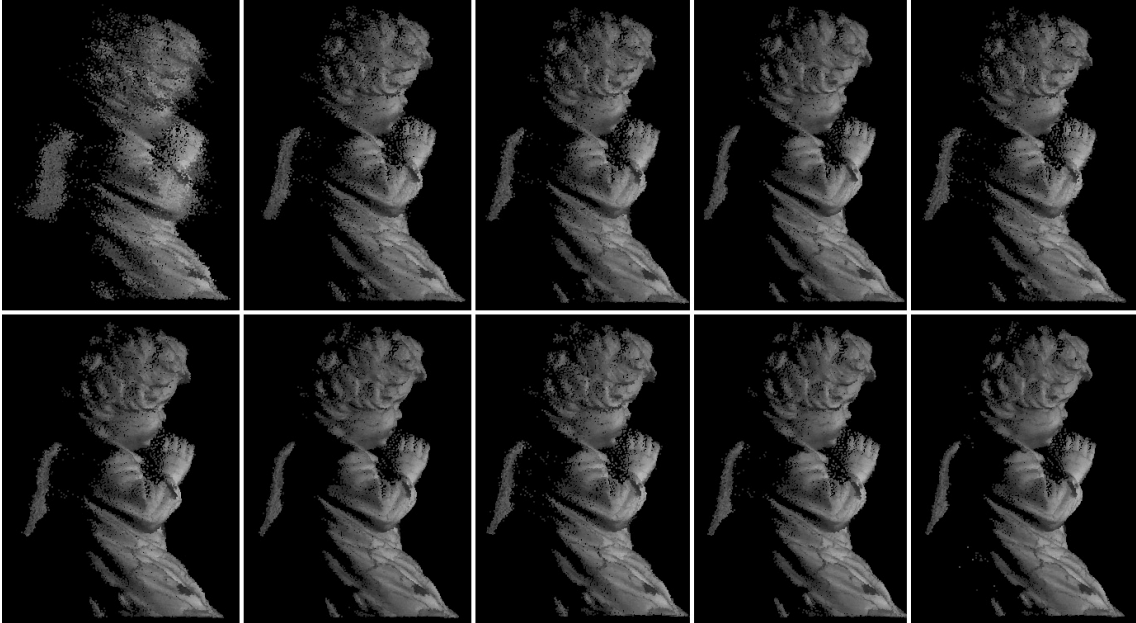


Figure 3.24: Side views of the 3-D reconstructed angel using 5-pattern unit-frequency PMP (top-1) and 5-pattern PCMP with $c_1 = 0.5$ and $f_h = 6$ (top-2), $c_1 = 0.5$ and $f_h = 8$ (top-3), $c_1 = 0.5$ and $f_h = 12$ (top-4), $c_1 = 0.6$ and $f_h = 6$ (top-5), $c_1 = 0.6$ and $f_h = 8$ (bottom-1), $c_1 = 0.6$ and $f_h = 12$ (bottom-2), $c_1 = 0.8$ and $f_h = 6$ (bottom-3), $c_1 = 0.8$ and $f_h = 8$ (bottom-4), and $c_1 = 0.8$ and $f_h = 12$ (bottom-5).

Chapter 4 Gamma Model and Its Analysis for Phase Measuring

Profilometry

Gamma distortion is the non-linear response of optical devices and follows power law. Although the basic gamma model for SLI had been developed and has been studied, the detailed equations describing the gamma issue have not been presented yet. In this chapter, we will present a detailed gamma model which is employed to analyze and address issues caused by gamma distortion, and finally that gamma model will be applied to correct phase error raised from gamma distortion. The correcting can be performed with and without gamma calibration. The RMS of phase error will be reduced by more than $60\times$ with gamma calibration and by more than $30\times$ without gamma calibration.

4.1 Gamma model for PMP

The projected PMP patterns are expressed as Eq. (1.1) and the ideal captured PMP-patterned images are described by Eq. (1.2). If there exists gamma distortion in the SLI system, the computation for A , B , and ϕ using Eqs. (1.3), (1.4), and (1.7) will not be accurate. And in order to analyze the problem conveniently, we rewrite Eq. (1.1) as

$$I_n^p = \alpha_p \left[\frac{1}{2} + \frac{1}{2} \cos\left(2\pi f y^p - \frac{2\pi n}{N}\right) \right] + \beta_p, \quad (4.1)$$

where α_p is a modulation constant controlling the intensity range of a sine wave, and β_p is a balance constant preventing underflow. Typically, α_p equals to 255 for an

8-bits per pixel and monochrome projector, and β_p is set to zero.

In the camera, in order to simplify the gamma issue, the ambient light intensity is not taken into account in this dissertation and the captured images distorted by gamma are now described as

$$I_n^c = \alpha\alpha_p \left[\frac{1}{2} + \frac{1}{2} \cos\left(\phi - \frac{2\pi n}{N}\right) \right]^\gamma, \quad (4.2)$$

where I_n^c is the intensity of a pixel, $\alpha \in [0, 1]$ is the reflectivity of a scanned object, $\phi \in [0, 2\pi)$ is the phase distortion of the sine wave, and γ is the combined gamma value for the projector-camera pair and we consider $\gamma \geq 1$. Note I_n^c , ϕ , α and γ are functions of the coordinates of a pixel, (x^c, y^c) , in the camera.

We note that, if the value of γ is unit, then there is no gamma distortion, and Eq. (1.2) will be a normal PMP equation. But in practice, typically γ is larger than one, and Eq. (1.2) is our original gamma model for PMP. We further note that, regardless of whether γ is an integer or not, the binomial series

$$(1 + x)^\alpha = \sum_{m=0}^{\infty} \left[\binom{\alpha}{m} x^m \right] \quad (4.3)$$

can be applied to Eq. (4.2) such that

$$I_n^c = \alpha_p \alpha_c \left(\frac{1}{2} \right)^\gamma \sum_{m=0}^{\infty} \left[\binom{\gamma}{m} \cos^m\left(\phi - \frac{2\pi n}{N}\right) \right]. \quad (4.4)$$

If we process the power of the cosine function in the Eq. (4.4) with

$$\cos^{2n} \theta = \frac{1}{2^{2n-1}} \sum_{k=0}^{n-1} \left\{ \binom{2n}{k} \cos[(2n - 2k)\theta] \right\} + \frac{1}{2^{2n}} \binom{2n}{n} \quad (4.5)$$

for even m and

$$\cos^{2n+1} \theta = \frac{1}{2^{2n}} \sum_{k=0}^n \left\{ \binom{2n+1}{k} \cos[(2n - 2k + 1)\theta] \right\} \quad (4.6)$$

for odd m , then a final form of our gamma model can be expressed as

$$I_n^c = A + \sum_{k=1}^{\infty} \left\{ B_k \cos \left[k \left(\phi - \frac{2\pi n}{N} \right) \right] \right\}, \quad (4.7)$$

where

$$A = \frac{1}{2} B_0 \quad (4.8)$$

and

$$B_k = \alpha \alpha_p \left(\frac{1}{2} \right)^{\gamma-1} \sum_{m=0}^{\infty} [b_{k,m}] \quad (4.9)$$

with

$$b_{k,m} = \frac{1}{2^{2m+k}} \binom{\gamma}{2m+k} \binom{2m+k}{m} \quad (4.10)$$

for k a non-negative integer. So at last, there are three forms of our gamma model expressed as Eqs. (4.2), (4.4), and (4.7) where Eq. (4.7) is consistent with the equation derived from Fourier Series in [48] and [20]. While their analysis did not present details of the coefficients A and B_k , we will analyze them next.

If γ is an integer ≥ 1 , $B_k = 0$ for all $k > \gamma$. In Fig. 4.1, it is shown that $B_1 > 0$ for all γ , $B_2 = 0$ at $\gamma = 1$, $B_3 = 0$ at $\gamma = 1$ and 2, and $B_4 = 0$ at $\gamma = 1, 2$, and 3. If γ is not an integer, B_k is a summation of infinite series but is absolutely convergent, which can be proven by the Raabe's test. For

$$\left| \frac{b_{k,m+1}}{b_{k,m}} \right| = \left| \frac{4m^2 + (4k - 4\gamma + 2)m + (k - \gamma + 1)(k - \gamma)}{4m^2 + (4k + 8)m + 4(k + 1)} \right|, \quad (4.11)$$

we find

$$\lim_{m \rightarrow \infty} \left| \frac{b_{k,m+1}}{b_{k,m}} \right| = 1 \quad (4.12)$$

and

$$\lim_{m \rightarrow \infty} \left[m \left(1 - \left| \frac{b_{k,m+1}}{b_{k,m}} \right| \right) \right] = 1.5 + \gamma > 1, \quad (4.13)$$

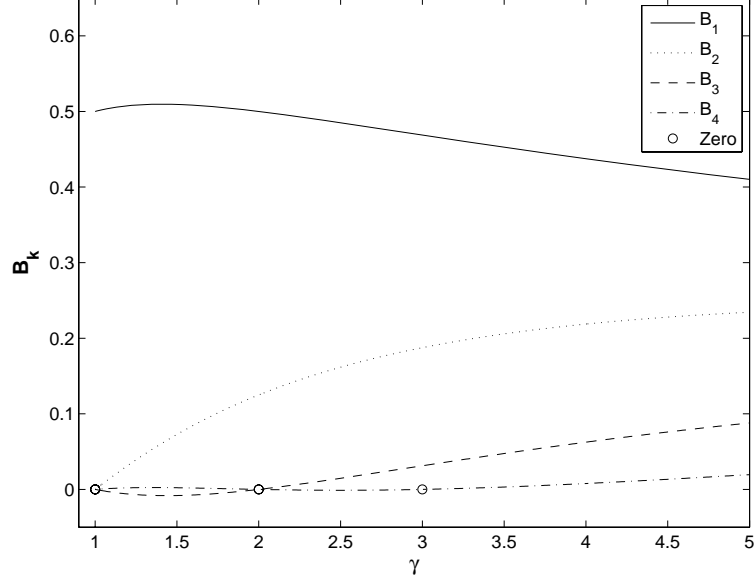


Figure 4.1: Coefficients B_k .

which indicate that B_k converges absolutely.

Figure 4.1 shows computed B_1 , B_2 , B_3 , and B_4 with $\alpha_p = 1$, $\alpha = 1$ and $\gamma \in [1, 5]$. The values of B_k ($k = 1, 2, 3, 4$) are not divergent for non-integer γ value. Now although B_k is a function of (α, γ) , α only acts as a scale according to Eq. (4.9). When we compute the ratio of B_k and B_{k+1} , not only can α be canceled, but the relationship between B_k and B_{k+1} can be derived as

$$\frac{B_{k+1}}{B_k} = \frac{\gamma - k}{\gamma + (k + 1)} \quad (4.14)$$

for $B_k \neq 0$. The procedure of derivation is as following. For Eq. (4.9), we only consider the part inside the summation and have

$$\hat{B}_k = \sum_{m=0}^{\infty} [b_{k,m}], \quad (4.15)$$

with

$$b_{k,m} = \frac{1}{2^{2m+k}} \binom{\gamma}{2m+k} \binom{2m+k}{m}. \quad (4.16)$$

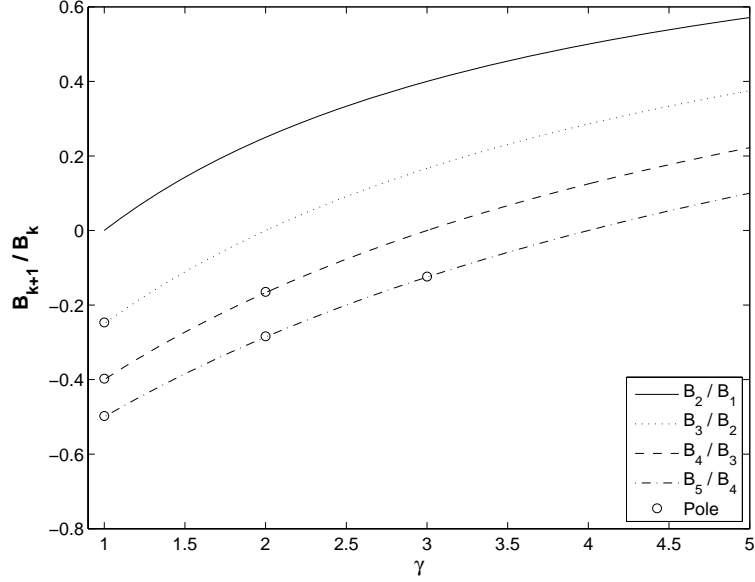


Figure 4.2: Ratios of $\frac{B_{k+1}}{B_k}$.

Then for

$$\hat{B}_{k+1} = \sum_{m=0}^{\infty} [b_{k+1,m}] \quad (4.17)$$

with

$$b_{k+1,m} = \frac{1}{2^{2m+k+1}} \binom{\gamma}{2m+k+1} \binom{2m+k+1}{m} = \left(\frac{\gamma-k-2m}{2m+2k+2} \right) b_{k,m}. \quad (4.18)$$

So we obtain

$$(\gamma-k)b_{k,m} - 2(k+1)b_{k+1,m} = 2mb_{k,m} + 2mb_{k+1,m}. \quad (4.19)$$

Sum the left and right part of the equal symbol above and we obtain

$$(\gamma-k) \sum_{m=0}^{\infty} [b_{k,m}] - 2(k+1) \sum_{m=0}^{\infty} [b_{k+1,m}] = (\gamma-k)\hat{B}_{k,m} - 2(k+1)\hat{B}_{k+1}. \quad (4.20)$$

and

$$\begin{aligned} 2 \sum_{m=0}^{\infty} [mb_{k,m}] + 2 \sum_{m=0}^{\infty} [mb_{k+1,m}] &= (\gamma-k-1)\hat{B}_{k+1} - 2 \sum_{m=0}^{\infty} [mb_{k+1,m}] + 2 \sum_{m=0}^{\infty} [mb_{k+1,m}] \\ &= (\gamma-k-1)\hat{B}_{k+1}. \end{aligned} \quad (4.21)$$

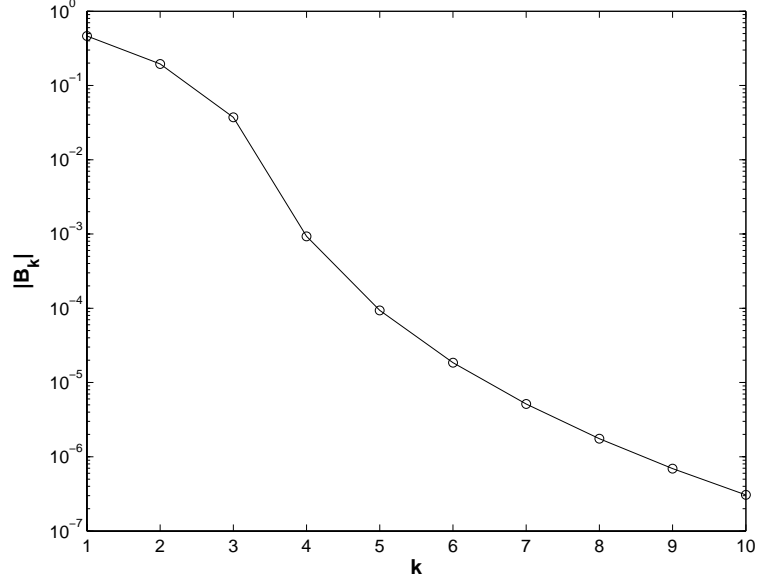


Figure 4.3: $|B_k|$ in log scale.

Finally from Eq. (4.20) and (4.21), we have

$$(\gamma - k)\hat{B}_k - 2(k + 1)\hat{B}_{k+1} = (\gamma - k - 1)\hat{B}_{k+1}, \quad (4.22)$$

and then the ratio of $\frac{B_{k+1}}{B_k}$ is derived as Eq. (4.14). It is this relationship that is the basis for this paper to calibrate the gamma model and even perform phase correction with or without gamma calibration.

Ratios of $\frac{B_2}{B_1}$, $\frac{B_3}{B_2}$, $\frac{B_4}{B_3}$ and $\frac{B_5}{B_4}$ are shown in Fig. 4.2 where there are poles in the figure at $B_k = 0$. From Eq. (4.14), we know

$$|B_k| > |B_{k+1}| \quad (4.23)$$

by

$$\left| \frac{B_{k+1}}{B_k} \right| = \left| \frac{\gamma - k}{\gamma + (k + 1)} \right| < \frac{\gamma + k}{\gamma + (k + 1)} < 1 \quad (4.24)$$

and

$$B_k = \left(\frac{\gamma - k + 1}{\gamma + k} \right) B_{k-1} = \left[\prod_{n=2}^k \left(\frac{\gamma - n + 1}{\gamma + n} \right) \right] B_1. \quad (4.25)$$

Because $\left| \frac{\gamma-k+1}{\gamma+k} \right| < 1$, B_k decreases dramatically with the increase of k . Figure 4.3 shows that, with $\gamma = 3.18$ and $k = 1, 2, \dots, 10$, B_k decreases very quickly. Additionally, there are some relationship as following

$$\alpha\alpha_p = A + \sum_{k=1}^{\infty} B_k \quad (4.26)$$

and

$$\alpha\alpha_p = 2 \sum_{k=1}^{\infty} B_{2k-1}. \quad (4.27)$$

between (A, B_k) and (α_p, α) .

When PMP algorithms including Eq. (1.3), (1.4), and (1.7) are performed to Eq. (4.7) and if γ equals to 1, then the computed A^c , B^c , and ϕ are treated as their true values without distortion according to

$$A^c = \frac{1}{2}\alpha\alpha_p, \quad (4.28)$$

$$B^c = \frac{1}{2}\alpha\alpha_p, \quad (4.29)$$

and

$$\phi = \arctan \left[\frac{\sin(\phi)}{\cos(\phi)} \right]. \quad (4.30)$$

But if $\gamma > 1$, then the computed A^c , B^c , and ϕ are distorted by gamma where the distorted A^c , notated by \tilde{A}^c , is computed as

$$\tilde{A}^c = A + \sum_{m=1}^{\infty} [B_{mN} \cos(mN\phi)] \quad (4.31)$$

$$= \frac{1}{2}B_0 + \sum_{m=1}^{\infty} [B_{mN} \cos(mN\phi)], \quad (4.32)$$

which converges to $A = \frac{1}{2}B_0$ with increasing N . Its absolute error, ΔA^c , is defined as

$$\begin{aligned}\Delta A^c &= A^c - \tilde{A}^c \\ &= \frac{1}{2}\alpha\alpha_p \left[1 - \left(\frac{1}{2}\right)^{\gamma-1} \sum_{m=0}^{\infty} (b_{0,m}) \right] - \sum_{m=1}^{\infty} [B_{mN} \cos(mN\phi)].\end{aligned}\quad (4.33)$$

If there is gamma distortion, *i.e.*, $\gamma > 1$, even with a very large N , then ΔA^c can not be reduced to zero and is related to B^c with a constant scale $1 - \left(\frac{1}{2}\right)^{\gamma-1} \sum_{m=0}^{\infty} (b_{0,m})$, which is a function of γ .

If we let

$$\begin{aligned}S_N &= \frac{2}{N} \sum_{n=0}^{N-1} \left[I_n^c \sin\left(\frac{2\pi n}{N}\right) \right] \\ &= B_1 \sin(\phi) + \sum_{k=1}^{\infty} \{B_{kN+1} \sin[(kN+1)\phi]\} \\ &\quad - \sum_{k=1}^{\infty} \{B_{kN-1} \sin[(kN-1)\phi]\}\end{aligned}\quad (4.34)$$

and

$$\begin{aligned}C_N &= \frac{2}{N} \sum_{n=0}^{N-1} \left[I_n^c \cos\left(\frac{2\pi n}{N}\right) \right] \\ &= B_1 \cos(\phi) + \sum_{k=1}^{\infty} \{B_{kN+1} \cos[(kN+1)\phi]\} \\ &\quad + \sum_{k=1}^{\infty} \{B_{kN-1} \cos[(kN-1)\phi]\},\end{aligned}\quad (4.35)$$

then the gamma distorted B^c , notated as \tilde{B}^c , is computed as

$$\begin{aligned}\tilde{B}^c &= \left[(S_N)^2 + (C_N)^2 \right]^{\frac{1}{2}} \\ &= B_1 D^{\frac{1}{2}}\end{aligned}\quad (4.36)$$

where

$$D = \left\{ \sum_{k=1}^{\infty} [b_{kN}^- \sin(kN\phi)] \right\}^2 + \left\{ 1 + \sum_{k=1}^{\infty} [b_{kN}^+ \cos(kN\phi)] \right\}^2, \quad (4.37)$$

$$b_{kN}^- = G_{kN-1}(\gamma) - G_{kN+1}(\gamma), \quad (4.38)$$

$$b_{kN}^+ = G_{kN-1}(\gamma) + G_{kN+1}(\gamma), \quad (4.39)$$

and

$$G_m(\gamma) = \frac{B_m}{B_1} = \prod_{n=2}^m \left(\frac{\gamma - n + 1}{\gamma + n} \right). \quad (4.40)$$

The term, \tilde{B}^c , converges to B_1 with increasing N . Its absolute error, ΔB^c , is defined according to

$$\begin{aligned} \Delta B^c &= B^c - \tilde{B}^c \\ &= \frac{1}{2} \alpha \alpha_p \left(1 - \left(\frac{1}{2} \right)^{\gamma-2} \sum_{m=0}^{\infty} (b_{1,m}) D^{\frac{1}{2}} \right), \end{aligned} \quad (4.41)$$

which can not converge to zero with increasing N .

Finally, the distorted phase $\tilde{\phi}$ is computed as

$$\begin{aligned} \tilde{\phi} &= \arctan \left(\frac{S_N}{C_N} \right) \\ &= \arctan \left\{ \frac{\sin(\phi) + H_s(\gamma, \phi)}{\cos(\phi) + H_c(\gamma, \phi)} \right\}, \end{aligned} \quad (4.42)$$

where

$$H_s(\gamma, \phi) = \sum_{k=1}^{\infty} G_{kN+1}(\gamma) \sin[(kN+1)\phi] - \sum_{k=1}^{\infty} G_{kN-1}(\gamma) \sin[(kN-1)\phi] \quad (4.43)$$

and

$$H_c(\gamma, \phi) = \sum_{k=1}^{\infty} G_{kN+1}(\gamma) \cos[(kN+1)\phi] + \sum_{k=1}^{\infty} G_{kN-1}(\gamma) \cos[(kN-1)\phi]. \quad (4.44)$$

The absolute phase error $\Delta\phi$ is defined as

$$\Delta\phi = \phi - \tilde{\phi}$$

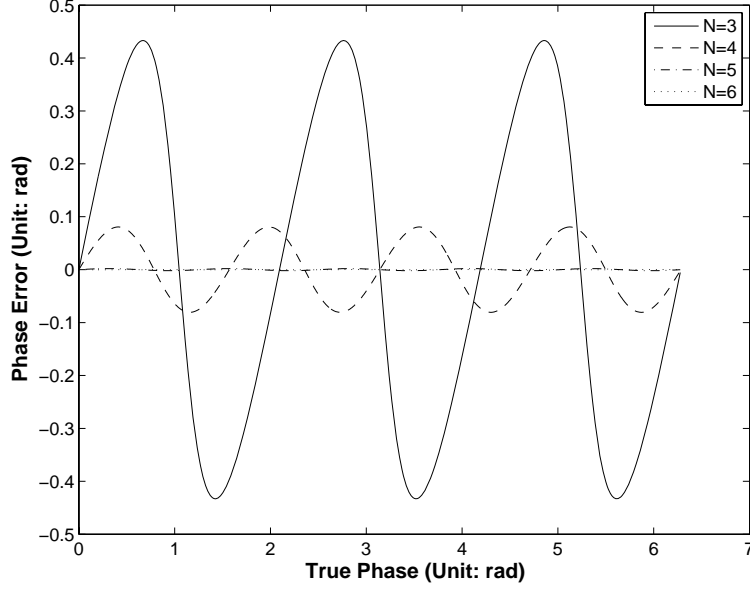


Figure 4.4: The absolute phase Error for different N .

$$\begin{aligned}
&= \arctan \left[\frac{\sin(\phi)}{\cos(\phi)} \right] - \arctan \left(\frac{S_N}{C_N} \right) \\
&= \arctan \left\{ \frac{\sum_{k=1}^{\infty} [b_{kN}^- \sin(kN\phi)]}{1 + \sum_{k=1}^{\infty} [b_{kN}^+ \cos(kN\phi)]} \right\}. \tag{4.45}
\end{aligned}$$

Obviously, the phase error $\Delta\phi$ is related to γ , the true phase ϕ , and the number of patterns N . It independent of α and α_p in Eq. (4.2). Phase error $\Delta\phi$ will converge to zero with increasing N because b_{kN}^- decreases dramatically with the increase of N . The larger the N , the smaller the $\Delta\phi$ and the less effect the γ .

At $\sin(N\phi) = 0$ or $\phi = \frac{\pi n}{N}$ ($n = 0, 1, \dots, N - 1$), $\Delta\phi$ is zero, which means that there is no phase error and $\tilde{\phi} = \phi = \frac{\pi n}{N}$. Phase errors for $N = 3, 4, 5$ and 6 with $\gamma = 3.18$ are shown in Fig. 4.4 and the RMS of phase error for $N = 3, 4, \dots, 40$ are shown in Fig. 4.5. It is seen that phase error decreases very quickly when pattern number N increases. The RMS errors for $N = 3, 4, 5$ and 6 are shown in Fig. 4.6 with γ changed from 1 to 5. The RMS errors are zero at $\gamma = 1$ for all N , at $\gamma = 2$

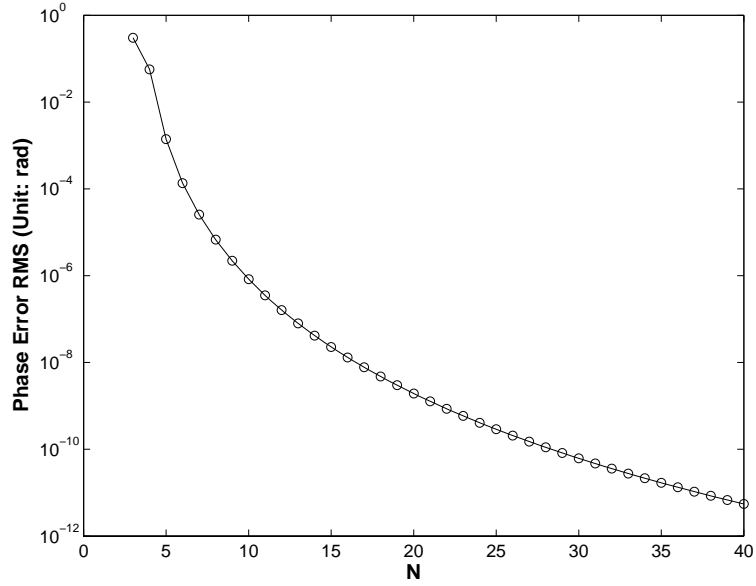


Figure 4.5: The RMS of phase error for different N in log scale.

for $N = 4, 5$ and 6 , at $\gamma = 3$ for $N = 5$ and 6 , and at $\gamma = 4$ for $N = 6$. The RMS of phase error is not always increased when the gamma is increased. Actually that is true when $\gamma + 2 \geq N$, while the RMS is bounded between any two zero points

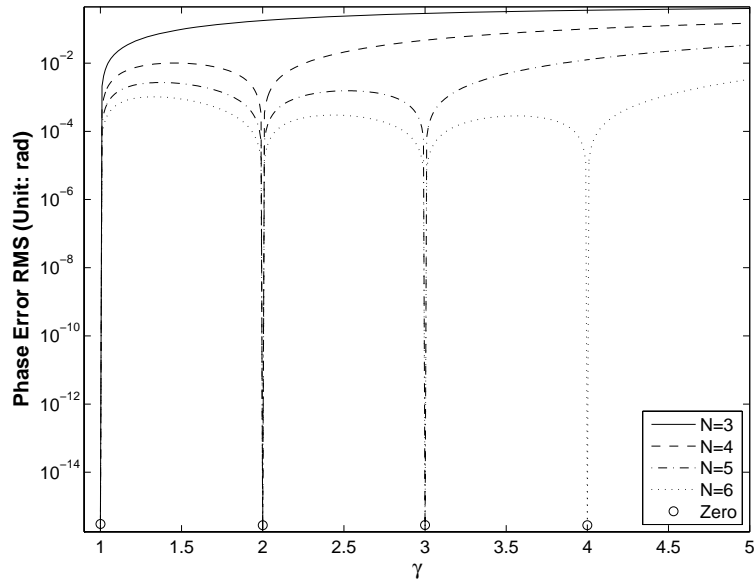


Figure 4.6: RMS of Phase Error for different N in log scale.

according to the Rolle's Theorem, if $\gamma + 2 \leq N$. Figure 4.6 shows that situation where it is found that, with some gamma value, the optimized number of patterns is at least $\lceil \gamma \rceil + 3$.

In Eq. (4.34) and (4.35) when $\sin\left(\frac{2\pi n}{N}\right)$ and $\cos\left(\frac{2\pi n}{N}\right)$ are multiplied to I_n^c and summation operations are performed, the first order harmonic mixed with the $(kN \pm 1)$ -th order harmonic can be extracted. More commonly when $\sin\left(m\frac{2\pi n}{N}\right)$ and $\cos\left(m\frac{2\pi n}{N}\right)$ are applied, the m -th order harmonic mixed with $(kN \pm m)$ -th order harmonic will be obtained according to

$$\begin{aligned}
S_{m,N} &= \frac{2}{N} \sum_{n=0}^{N-1} \left[I_n^c \sin\left(m\frac{2\pi n}{N}\right) \right] \\
&= B_m \sin(m\phi) + \sum_{k=1}^{\infty} \{B_{kN+m} \sin[(kN+m)\phi]\} \\
&\quad - \sum_{k=1}^{\infty} \{B_{kN-m} \sin[(kN-m)\phi]\}, \tag{4.46}
\end{aligned}$$

and

$$\begin{aligned}
C_{m,N} &= \frac{2}{N} \sum_{n=0}^{N-1} \left[I_n^c \cos\left(m\frac{2\pi n}{N}\right) \right] \\
&= B_m \cos(m\phi) + \sum_{k=1}^{\infty} \{B_{kN+m} \cos[(kN+m)\phi]\} \\
&\quad + \sum_{k=1}^{\infty} \{B_{kN-m} \cos[(kN-m)\phi]\}, \tag{4.47}
\end{aligned}$$

where $m \in [1, \frac{N-1}{2}]$ for odd N and $m \in [1, \frac{N}{2} - 1]$ for even N . We call the m -th order harmonic the main harmonic and the mixed $kN \pm m$ -th order harmonic as same-phase harmonic. The effect of the same-phase harmonic to the main harmonic depends on the number of patterns N . The larger the N , the smaller the effects of the same-phase harmonics. If $m \ll \frac{N}{2}$ with the truth $B_{kN \pm m} \ll B_m$, Eq. (4.46) and (4.47) can

be treated as

$$\frac{2}{N} \sum_{n=0}^{N-1} \left[I_n^c \sin\left(m \frac{2\pi n}{N}\right) \right] \approx B_m \sin(m\phi) \quad (4.48)$$

and

$$\frac{2}{N} \sum_{n=0}^{N-1} \left[I_n^c \cos\left(m \frac{2\pi n}{N}\right) \right] \approx B_m \cos(m\phi). \quad (4.49)$$

So B_m will be computed by

$$B_m \approx \frac{2}{N} \left\{ \left[\sum_{n=0}^{N-1} I_n^c \sin\left(m \frac{2\pi n}{N}\right) \right]^2 + \left[\sum_{n=0}^{N-1} I_n^c \cos\left(m \frac{2\pi n}{N}\right) \right]^2 \right\}^{\frac{1}{2}} \quad (4.50)$$

employing a large N . We will use this property to calculate the γ value later.

When N is even and $m = \frac{N}{2}$, $\sin\left(m \frac{2\pi n}{N}\right) = \sin(n\pi)$ is zero, and Eq. (4.46) is zero in this case. But Eq. (4.47) is not zero for $\cos\left(m \frac{2\pi n}{N}\right) = \cos(n\pi) = \pm 1$ and is rewritten as

$$\begin{aligned} B_{cos} &= \frac{2}{N} \sum_{n=0}^{N-1} \left[I_n^c \cos\left(m \frac{2\pi n}{N}\right) \right] \\ &= 2 \sum_{m=0}^{\infty} B_{\frac{N}{2}+mN} \cos\left[\left(\frac{N}{2} + mN\right)\phi\right], \end{aligned} \quad (4.51)$$

which is useful for phase correction later. Using Eq. (4.46) and (4.47), the phase of m -th frequency can be derived as

$$\phi_m = \arctan\left(\frac{S_{m,N}}{C_{m,N}}\right), \quad (4.52)$$

which is also helpful for phase correction later.

4.2 Phase correction with gamma calibration

The relationship between the true phase, ϕ , and the measured and gamma distorted phase, $\tilde{\phi}$, is described in Eq. (4.42). It is certain that phase correction can be realized

by solving the following function at $f_1(\gamma, \phi) = 0$

$$f_1(\gamma, \phi) = \arctan \left[\frac{\sin(\phi) + H_s(\gamma, \phi)}{\cos(\phi) + H_c(\gamma, \phi)} \right] - \tilde{\phi}, \quad (4.53)$$

where $H_s(\gamma, \phi)$ and $H_c(\gamma, \phi)$ are defined in Eq. (4.43) and (4.44), and $\tilde{\phi}$ is the distorted phase measured by Eq. (1.7). There are two unknown parameters, γ and ϕ , in the Eq. (4.53), so once an appropriate γ value is available, ϕ can be computed easily, and phase correction is achieved.

Traditionally to measure the gamma of a particular SLI system [25], a series of uniform patterns with different grayscale values are projected onto a white board, and a camera records the intensities, corresponding to the patterns, of one pixel or small set of pixels in a particular area of the screen. Then the gamma value can be computed with those recorded intensity values by fitting a curve, and that gamma value is applied for every pixel globally. In contrast by taking advantage of the Eq. (4.14), γ can be computed by

$$\gamma = \frac{kB_k + (k+1)B_{k+1}}{B_k - B_{k+1}} \quad (4.54)$$

with $B_k \neq B_{k+1}$. So if we know B_k and B_{k+1} , especially B_1 and B_2 , then γ can be calculated according to

$$\gamma = \frac{B_1 + 2B_2}{B_1 - B_2}, \quad (4.55)$$

where B_1 and B_2 are computed by Eq. (4.50). Then the gamma values for each pixel in the image can be obtained directly and locally without fitting any curves. To get B_2 , at least 5 PMP patterns should be involved with more patterns leading to a more accurate computation of B_1 , B_2 , and γ .

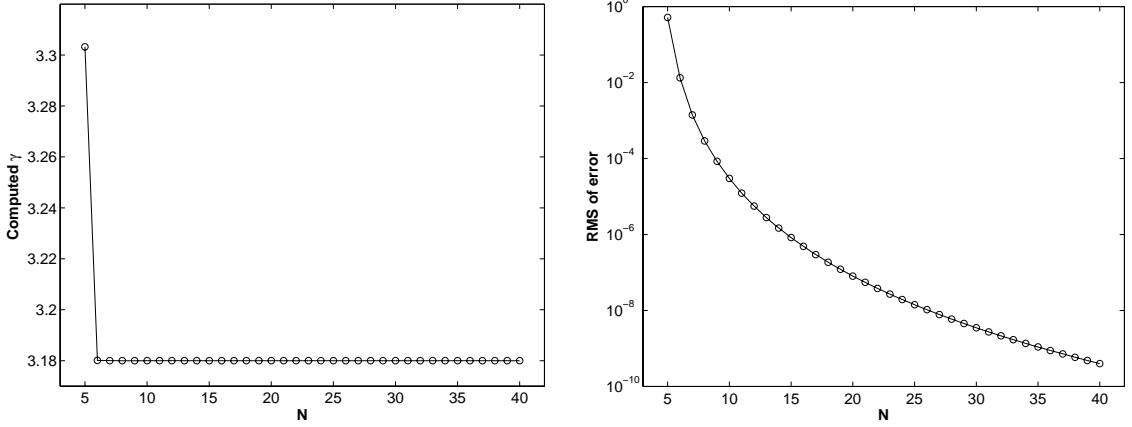


Figure 4.7: Gamma computation versus the number of patterns, N , showing (left) the computed gamma and (right) the RMS of error in log scale.

With $\gamma = 3.18$ and $N = 5, 6, \dots, 40$ respectively, B_1 and B_2 are computed with $m = 1$ and $m = 2$ by Eq. (4.50), then γ is obtained easily through Eq. (4.55). Figure 4.7 (left) shows the computed γ with different N and Fig. 4.7 (right) shows the corresponding RMS of the computation error. With the increasing of the N , the error decreases quickly, and the computed γ converges to the true γ .

Once an accurate gamma value for a pixel is obtained, then in Eq. (4.53), there is only the one unknown parameter, ϕ , left to solve. The distorted phase at that pixel can be accurately corrected according to

$$f_2(\phi) = \arctan \left[\frac{\sin(\phi) + H_s(\gamma, \phi)}{\cos(\phi) + H_c(\gamma, \phi)} \right] - \tilde{\phi} \quad (4.56)$$

at $f_2(\phi) = 0$. The upper limit of summations in Eq. (4.43) and (4.44) does not need to be infinity and can be any number satisfying some accuracy requirement. The accuracy depends on how many harmonics are involved with more harmonics leading to higher accuracy. Suppose $\gamma = 3.18$ is known and $N = 3$, we employ Eq. (4.56) to correct phase with the 2nd, 4th, 5th, 7th, and 8th harmonics, respectively. The

Table 4.1: RMS of phase error (the RMS of phase error is 0.3033 before correction)

2nd	4th	5th	7th	8th
0.004	3.7×10^{-4}	2.9×10^{-5}	6.2×10^{-6}	1.8×10^{-6}

RMS of the phase errors are listed in Table.4.1. The RMS of phase error decreases dramatically with more harmonics.

In practice, the gamma value at each pixel is not always exactly the same, which is shown experimentally later. So a trade-off solution is to apply an averaged gamma value, $\bar{\gamma}$, globally to Eq. (4.56) to become

$$f_3(\phi) = \arctan \left[\frac{\sin(\phi) + H_s(\bar{\gamma}, \phi)}{\cos(\phi) + H_c(\bar{\gamma}, \phi)} \right] - \tilde{\phi}. \quad (4.57)$$

This solution is more useful in practice because gamma calibration needs to be performed only once.

4.3 Phase correction without gamma calibration

In the Eq. (4.53), there are two unknown parameters, γ and ϕ , such that not having an accurate estimation of γ , the true ϕ can not be solved directly at $f_1(\gamma, \phi) = 0$. Obviously, one or more additional constraints/conditions are needed to help solve the equation. In the previous section, we employed gamma calibration to obtain the gamma value and reduce Eq. (4.53), a two-parameter function, to Eq. (4.56) or (4.57), both one-parameter functions. In this section, we solve the problem without directly performing gamma calibration but by solving Eq. (4.53) in terms of a series of potential constraints, derived from our gamma model, for different pattern numbers.

We note that as an optimization procedure, it may be beneficial to constrain the determination of γ and ϕ . So by applying determinant constraints, there are three

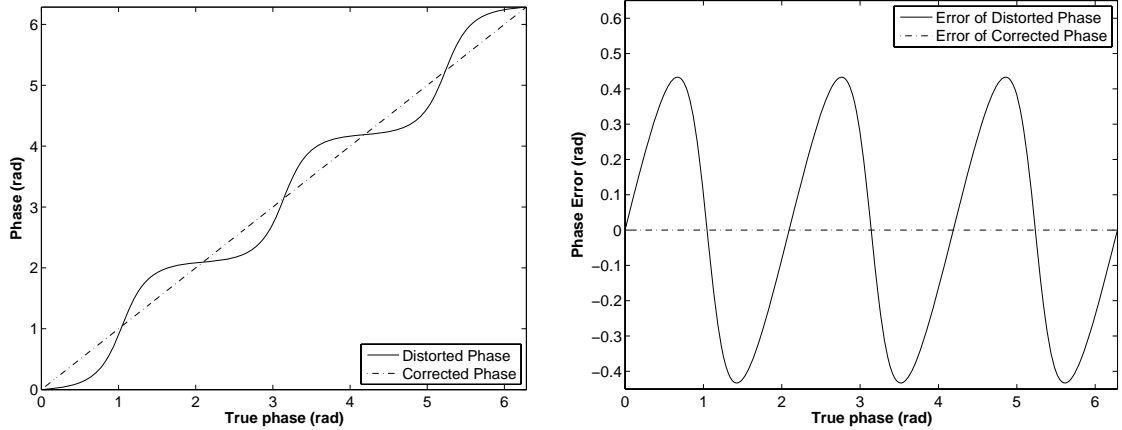


Figure 4.8: The (left) distorted and corrected phase for $\gamma = 3.18$ and the (right) corresponding distorted and corrected phase error using $N = 3$ constrained phase optimization without gamma calibration.

cases one should consider depending on the number of projected PMP patterns.

For instance when $N = 3$ and when there is no ambient light or the intensity of ambient light is much smaller than the minimum intensity of projected patterns, A^c and B^c can be used to form the second condition function for Eq. (4.53) as

$$f_{c1}(\gamma, \phi) = \frac{\frac{1}{2}G_0(\gamma) + \sum_{k=1}^{\infty}[G_{3k}(\gamma) \cos(3k\phi)]}{\{[\sin(\phi) + H_s(\gamma, \phi)]^2 + [\cos(\phi) + H_c(\gamma, \phi)]^2\}^{\frac{1}{2}}} - \frac{\tilde{A}^c}{\tilde{B}^c}, \quad (4.58)$$

with

$$G_0(\gamma) = \frac{B_0}{B_1} = \frac{\gamma + 1}{\gamma}, \quad (4.59)$$

where H_s , H_c , and $G_m(\gamma)$ are defined in Eq. (4.43), (4.44), and (4.40) and \tilde{A}^c and \tilde{B}^c are computed with Eq. (1.3) and (1.4). Figure 4.8 (left) shows the corrected phase using the constraint above with $\gamma = 3.18$ and the error is shown in Fig. 4.8 (right).

With the added constraint, γ converged to 3.18 for all pixels.

For $N = 4$, by means of Eq. (4.51), we can obtain the second condition for

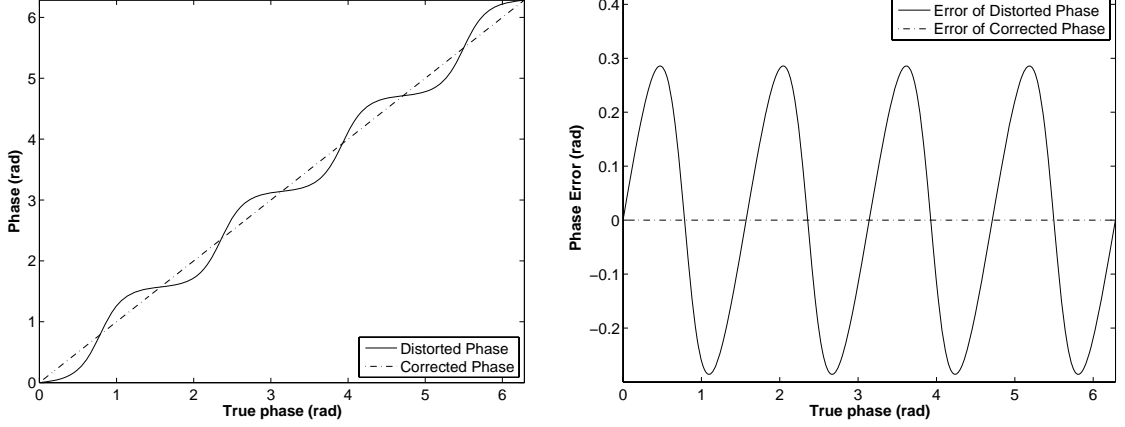


Figure 4.9: The (left) distorted and corrected phase for $\gamma = 6.36$ and the (right) corresponding distorted and corrected phase error using $N = 4$ constrained phase optimization without gamma calibration.

Eq. (4.53) as

$$f_{c2}(\gamma, \phi) = \frac{2 \sum_{m=0}^{\infty} \{G_{2+4m}(\gamma) \cos[(2+4m)\phi]\}}{\{[\sin(\phi) + H_s(\gamma, \phi)]^2 + [\cos(\phi) + H_c(\gamma, \phi)]^2\}^{\frac{1}{2}}} - \frac{\tilde{B}_{cos}}{\tilde{B}^c}, \quad (4.60)$$

where \tilde{B}_{cos} is measured by Eq. (4.51). Figure 4.9 (left) shows the corrected phase using the constraint above with $\gamma = 6.36$ and the error is shown in Fig. 4.9 (right). The RMS of error is nearly zero and as before with the added constraint, γ converged to simulated value (6.36) for all pixels.

For $N \geq 5$, the second frequency can be obtained through Eq. (4.52) with $m = 2$, and the second condition function for Eq. (4.53) becomes

$$f_{c3}(\gamma, \phi) = \arctan \left[\frac{\sin(2\phi) + H_{s2}(\gamma, \phi)}{\cos(2\phi) + H_{c2}(\gamma, \phi)} \right] - \tilde{\phi}_2, \quad (4.61)$$

with

$$H_{s2}(\gamma, \phi) = \sum_{k=1}^{\infty} G_{kN+2}(\gamma) \sin[(kN+2)\phi] - \sum_{k=1}^{\infty} G_{kN-2}(\gamma) \sin[(kN-2)\phi], \quad (4.62)$$

and

$$H_{c2}(\gamma, \phi) = \sum_{k=1}^{\infty} G_{kN+2}(\gamma) \cos[(kN+2)\phi] + \sum_{k=1}^{\infty} G_{kN-2}(\gamma) \cos[(kN-2)\phi], \quad (4.63)$$

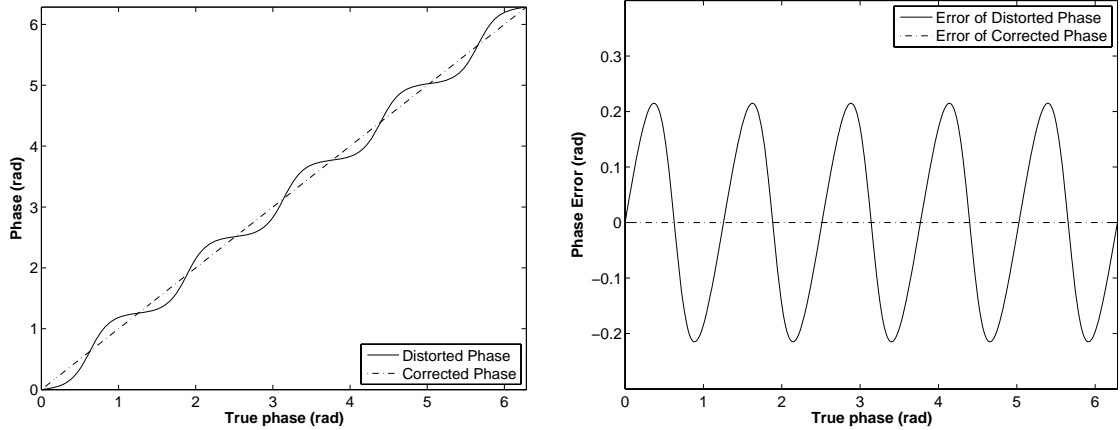


Figure 4.10: The (left) distorted and corrected phase for $\gamma = 10.36$ and the (right) corresponding distorted and corrected phase error using $N = 5$ constrained phase optimization without gamma calibration.

where $\tilde{\phi}_2$ is measured by Eq. (4.52). Figure 4.10 (left) shows the corrected phase using the constraint above with $\gamma = 10.36$ and the error is shown in Fig. 4.10 (right). The RMS of error is nearly zero and as before with the added constraint, γ converged to simulated value (10.36) for all pixels.

4.4 Phase correction with phase matching

Phase matching was studied in [33] and [119] where it was shown that matching phase, across two cameras, can be an effective means of reconstructing depth by means of triangulating phase as opposed to matching between a single camera and single projector. Although not explicitly stated, this mechanism is an effective way to minimize the effects of gamma, assuming that both cameras are equally affected, such that both cameras see the same distorted phase image. This section proves that, if a SLI system, as shown in Fig. 4.11, is composed of a projector and two cameras, then intensities of the same point, on the target surface, are typically viewed different in

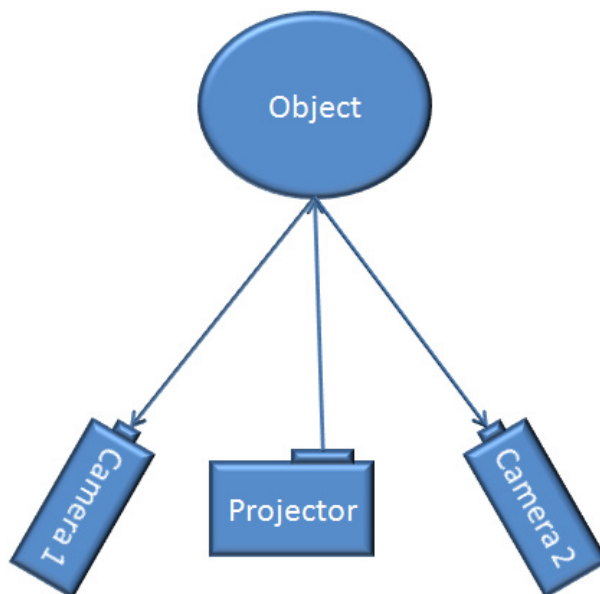


Figure 4.11: Gamma correction with phase matching.

the two cameras. But according to Eq. (4.42), the phases discovered by the cameras are exactly the same, if the gamma values observed by the two cameras are the same. The same distorted phase is then the basis for performing phase matching, and thus, the phase can be corrected without knowing the value of gamma.

4.5 Experiment

In this section, several experiments are performed to verify the proposed phase correction algorithms for the proposed gamma model. The first experiment performs phase calibration with gamma calibration while the second group of experiments perform phase correction without gamma calibration. For this purpose, our employed SLI system is composed of an ordinary PC, an Infocus LP70+ DLP projector with 1280×1024 pixel resolution and 1000 ANSI lumens output, and an 8-bits per pixel, monochrome, Prosilica EC1280 camera with a maximum resolution of 1280×1024

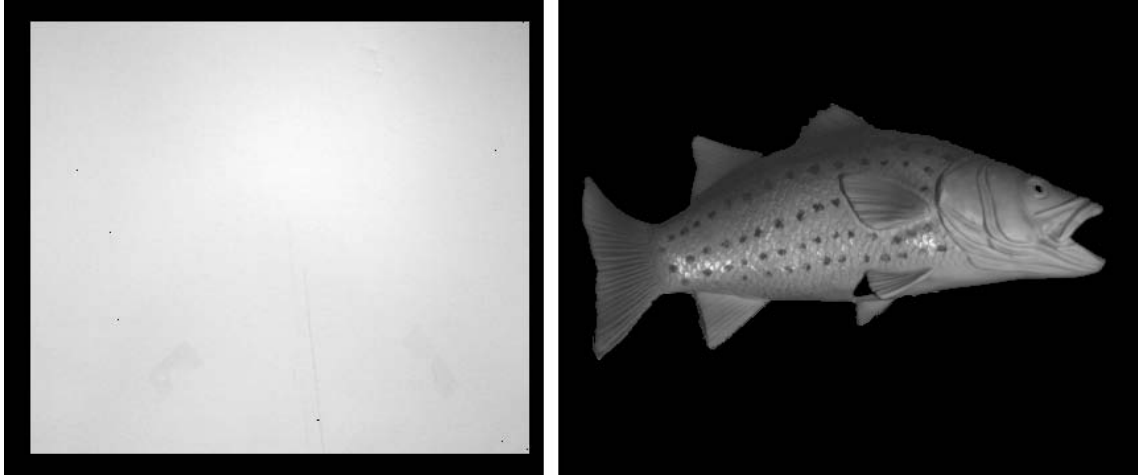


Figure 4.12: Photos of the scanned objects used in our experiment showing (left) a white board with uniform texture and (right) a plastic fish with varying texture.

pixels. The scanned objects in our experiments, whose photos are shown in Fig. 4.12, are a flat, white, sheet of foam board with uniform texture and a plastic toy fish with varying texture. The ground truth phases of the scanned objects were both

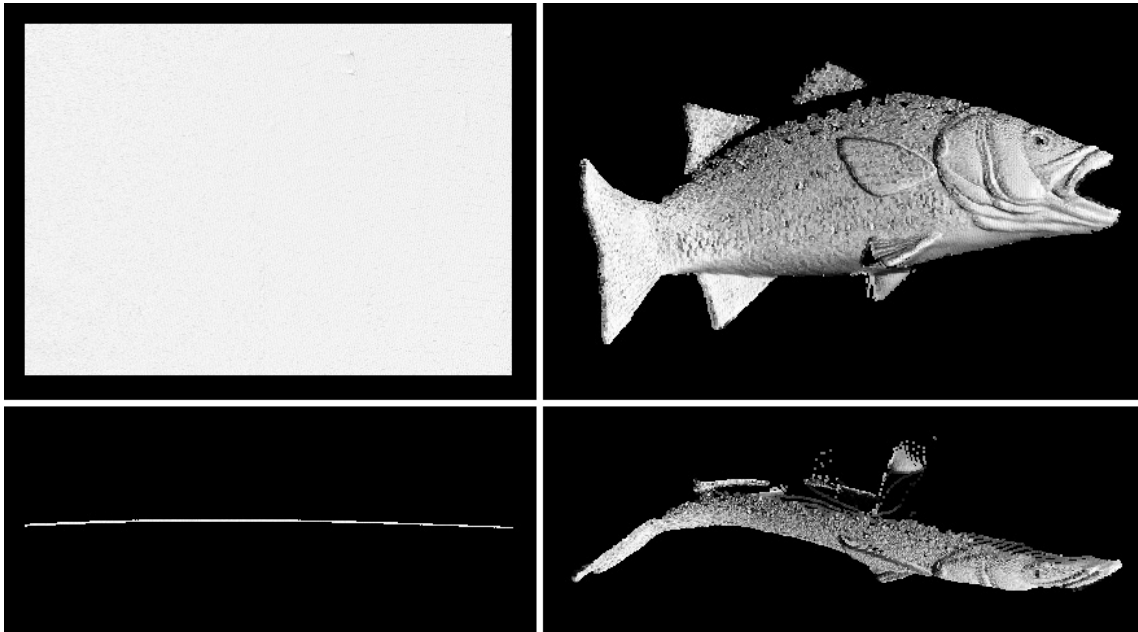


Figure 4.13: The ground truth of 3-D reconstructions of the textureless foam board (left) and the textured plastic fish (right) viewed from the front (top) and from above (bottom).

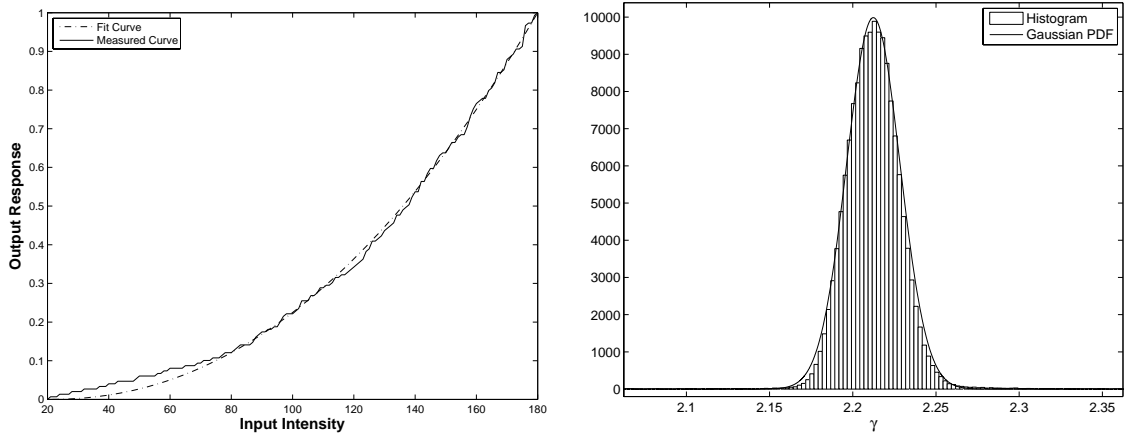


Figure 4.14: The (left) best-fit curve for a pixel with a measured gamma value of 2.153 and (right) the histogram of the calibrated gamma in the entire image where the mean is 2.2123 with variance 2.67×10^{-4} .

generated using PMP with $N = 48$ and a frequency of $f = 16$, or 16 sinusoidal periods spanning the projector’s field of view. Figure 4.13 shows the ground truth of 3-D reconstructions of the textureless foam board (left) and the textured plastic fish (right) viewed from the front (top) and from above (bottom). Because we are only focusing on gamma distortion, the effects of measurement uncertainty (white-noise) were reduced by averaging multiple PMP scans as suggested by Huang [21].

Phase correction with gamma calibration

As stated previously, traditional curve fitting involves measuring the gamma for a small, central region of the projected pattern as demonstrated in Fig. 4.14 (left) where we show the best-fit curve for a set of intensity measurements made over 160 images. The best-fit curve, in this case, corresponds to a gamma value of 2.153. But as we know, this approach is not robust since we do not know if this particular gamma value represents a minimum, maximum, or mean value the entire range of gamma

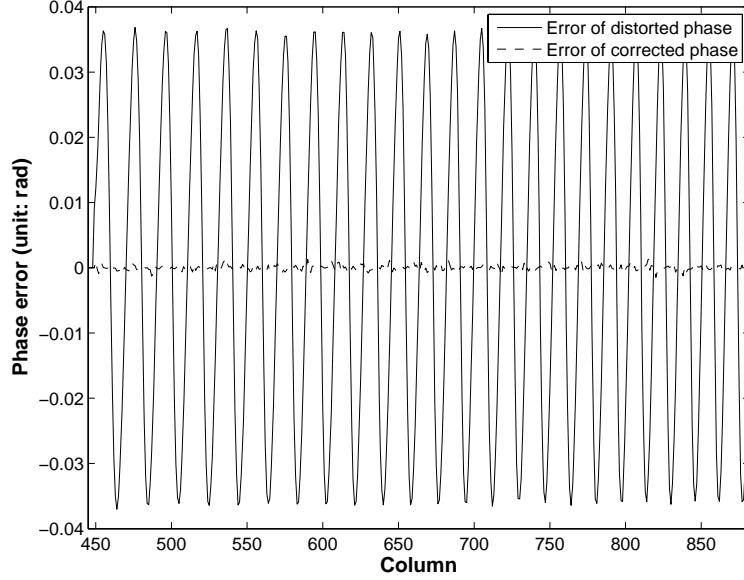


Figure 4.15: The error of distorted phase and corrected phase (with gamma calibration) for $\gamma = 2.21$ of the 512th row of the board.

across the projected field of view.

As an alternative approach to measuring gamma, we note that, by taking advantage of the relationship between B_1 and B_2 , we can compute gamma directly by means of Eq. (4.55) for each pixel, across the entire image, such that B_1 and B_2 are obtained by the Eq. (4.50) with $m = 1$ and $m = 2$. We can then calculate a gamma matrix with a reliably estimated mean gamma value. To get even more accurate B_1 and B_2 , we can average multiple estimates together. Figure 4.14 (right) shows the histogram of the computed gamma for each valid pixel, averaged over 48 estimates, in the image with a mean value of 2.2123 and variance 2.67×10^{-4} . From observation, the measured histogram follows a Gaussian distribution.

Now having a calibrated gamma estimate, we can now evaluate the effects of phase correction when scanning our white board using $N = 3$ pattern PMP with pattern frequency $f = 8$. Using Eq. (4.57) with the calibrated mean gamma value of 2.2123

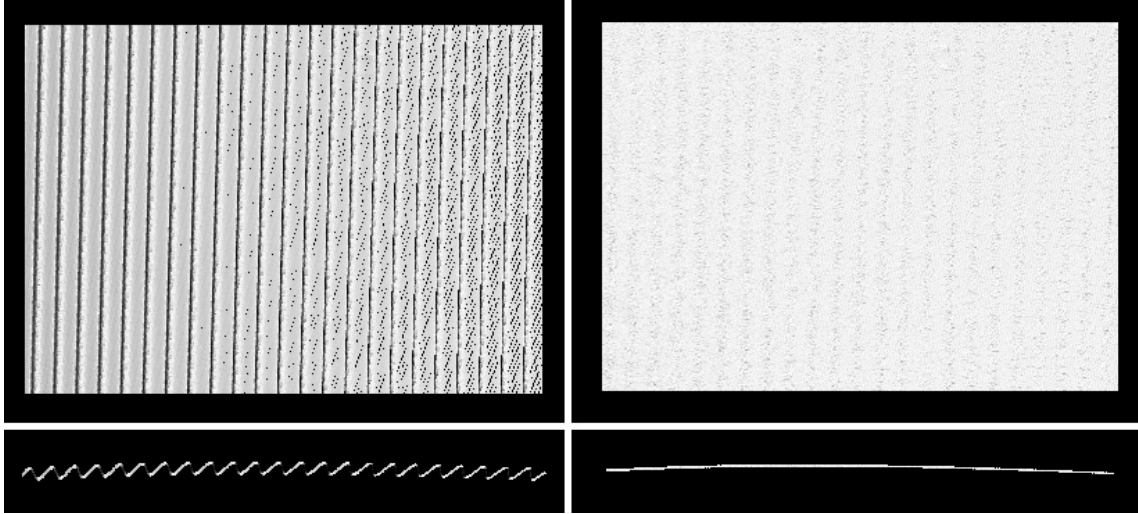


Figure 4.16: The 3-D reconstructions of the textureless foam board viewed from the front and from above for the (left) uncorrected phase and (right) corrected phase with gamma calibration.

for all phase pixels, the RMS of the error of the 512th row, in the corrected phase image, is reduced from 0.0256 to 4.2×10^{-4} as shown in Fig. 4.15 versus 1.1×10^{-3} had we employed the traditionally calibrated gamma value of 2.153. The corresponding,

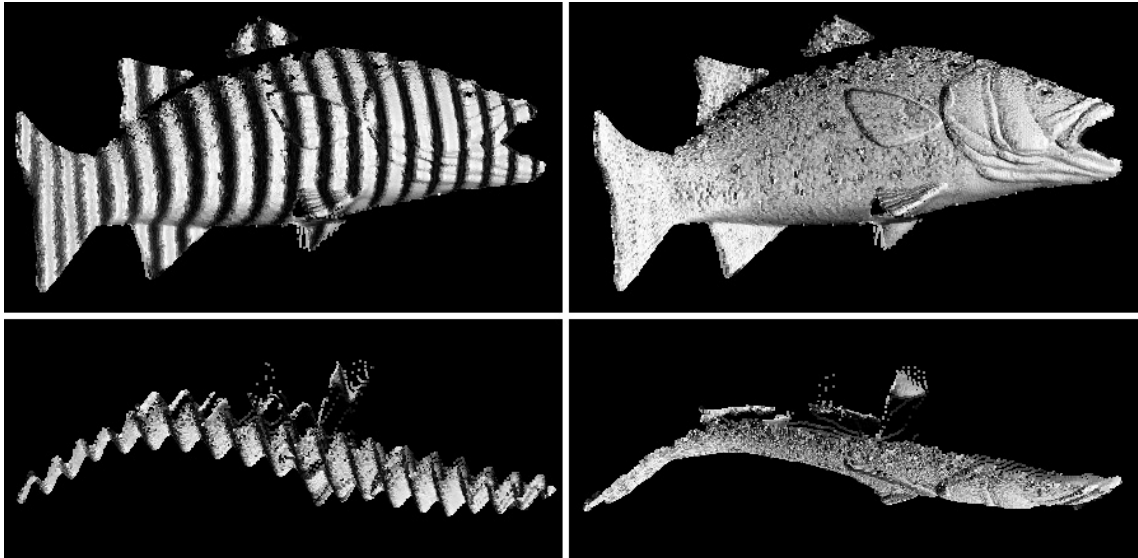


Figure 4.17: The 3-D reconstructions of the textured plastic fish viewed from the front and from above for the (left) uncorrected phase and (right) corrected phase with gamma calibration.

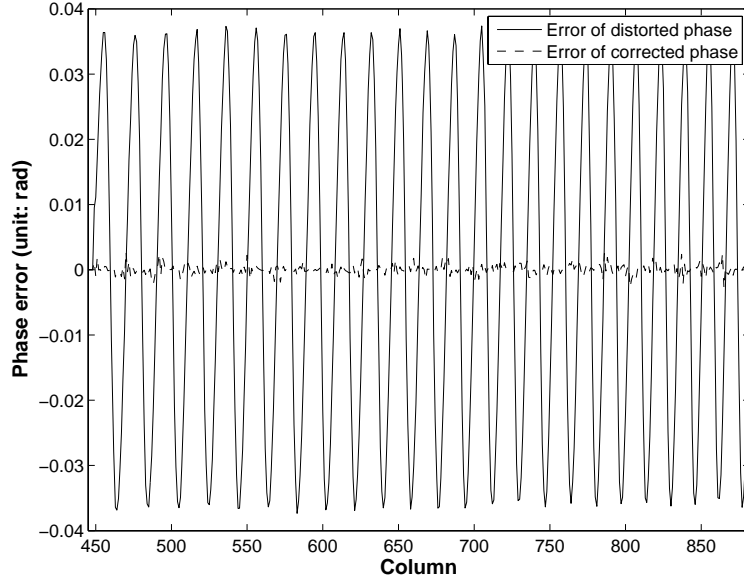


Figure 4.18: Employing a second constraint for $N=3$, the error of gamma distorted phase and corrected phase for $\gamma = 2.21$ of the 512th row of the board.

reconstructed, 3-D point clouds for the foam board using the ground truth phase, the gamma distorted phase, and the corrected phase are illustrated in Fig. 4.16.

Now when the same algorithm is applied to a an arbitrary surface (toy fish) with varying texture, a similar improvement (4.9×10^{-4} versus 1.5×10^{-3}) in phase can be seen as illustrated in Fig. 4.17 where the calculated gamma, derived from the relationship between B_1 and B_2 , was 2.2079. This second result is especially important because gamma calibration was performed using this arbitrary, textured, toy fish surface. We did not carry over the calibration result from the textureless foam board, as one might expect to have performed calibration.

Phase correction without gamma calibration

In the previous subsection, we demonstrated that, with gamma calibration, phase can be greatly improved by means of gamma correction, but as we will show, a stand-

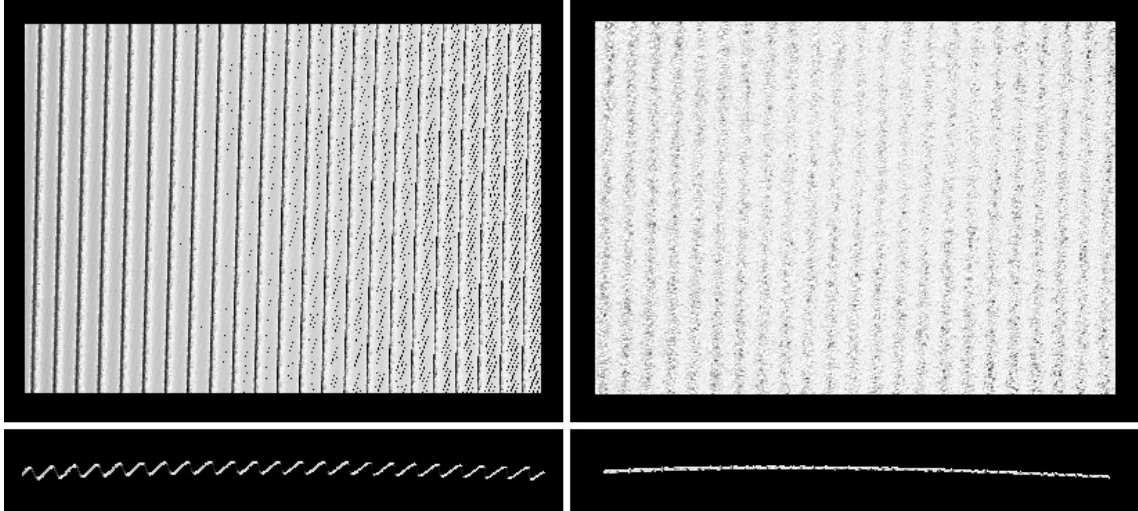


Figure 4.19: The 3-D reconstructions of the textureless foam board viewed from the front and from above for the (left) uncorrected phase and (right) corrected phase with $N = 3$ constrained gamma and phase optimization.

alone calibration procedure is not necessary in order to perform this phase correction.

If the gamma value is not available or not easily measured, the distorted phase can be corrected by minimizing the energy in the harmonic components by solving Eq. (4.53)

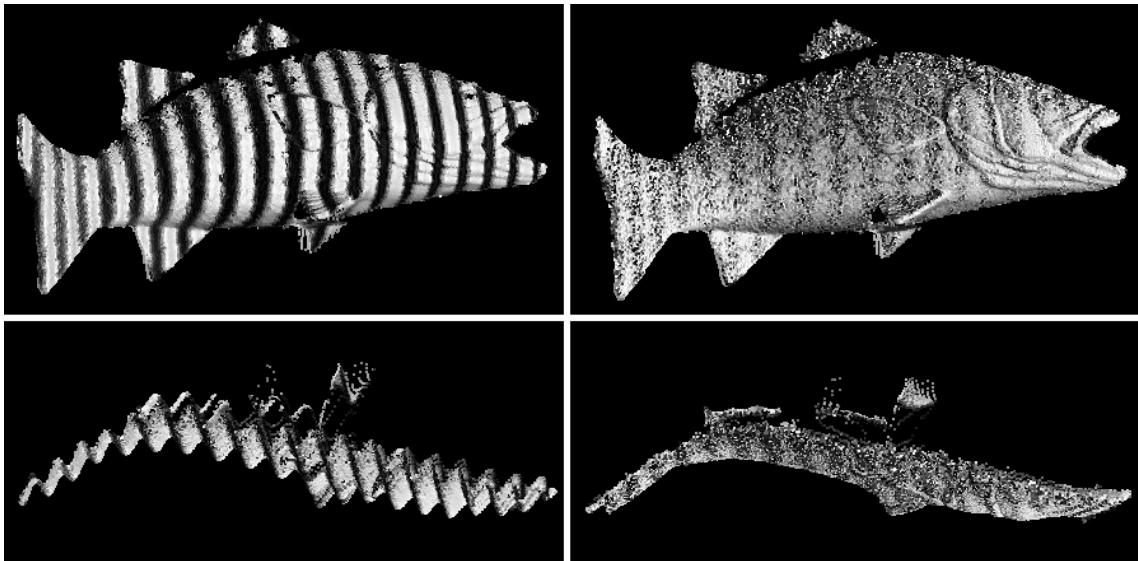


Figure 4.20: The 3-D reconstructions of the textured plastic fish viewed from the front and from above for the (left) uncorrected phase and (right) corrected phase with $N = 3$ constrained gamma and phase optimization.

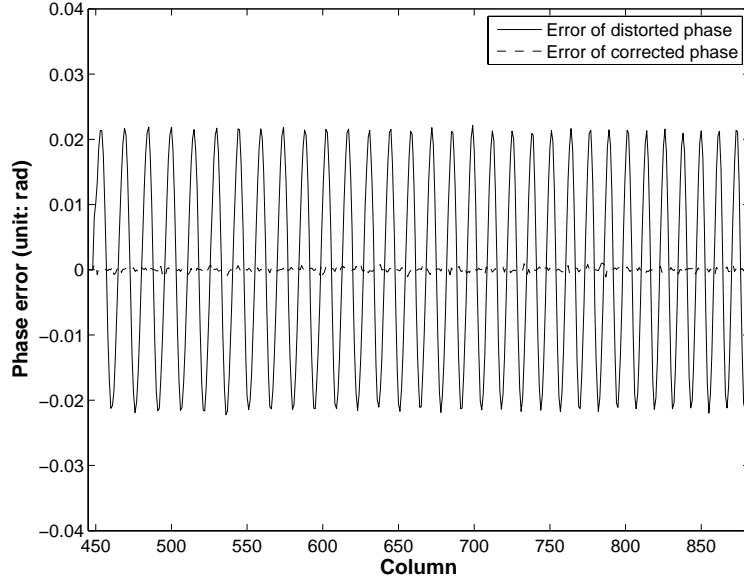


Figure 4.21: Employing a second constraint for $N=4$, the error of gamma distorted phase and corrected phase for $\gamma = 4.42$ of the 512th row of the board.

versus both the phase angle, ϕ , and the gamma parameter, γ . As an optimization problem though, the quality of the final solution depends upon any constraints that might be applied.

In order to demonstrate constrained optimization, we perform $N = 3$ pattern PMP with nearly zero ambient light such that Eq. (4.58) becomes a constraint for Eq. (4.53). Figure 4.18 shows that RMS of the error of the 512th row of the board, of the corrected phase image, is reduced to 7.5957×10^{-4} for a $33\times$ improvement compared to the 0.0256 RMS of the error of distorted phase. For completeness, Fig. 4.19 shows the reconstructed 3-D point clouds for the textureless foam board from the ground truth phase, gamma distorted phase, and corrected phase. Applying the same constrained optimization to our plastic fish with varying texture (Fig. 4.20) produces a similar improvement over uncorrected reconstruction.

Using $N = 4$ pattern PMP with frequency $f = 8$ and $\gamma = 2.21$, the phase

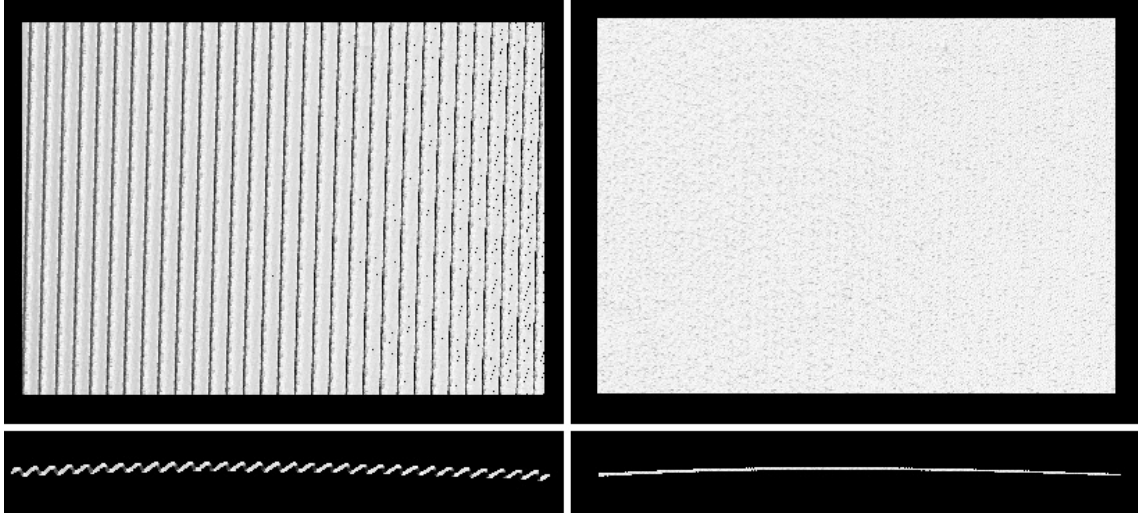


Figure 4.22: The 3-D reconstructions of the textureless foam board viewed from the front and from above for the (left) uncorrected phase and (right) corrected phase with $N = 4$ constrained gamma and phase optimization.

error is very small. So in order to show our phase correction algorithm for $N = 4$, we artificially adjusted our projector's gamma to 4.42 in software, just as Baker *et al.* [20] did. By doing so, Eq. (4.60) can act as the constraint on Eq. (4.53). Figure 4.21 shows

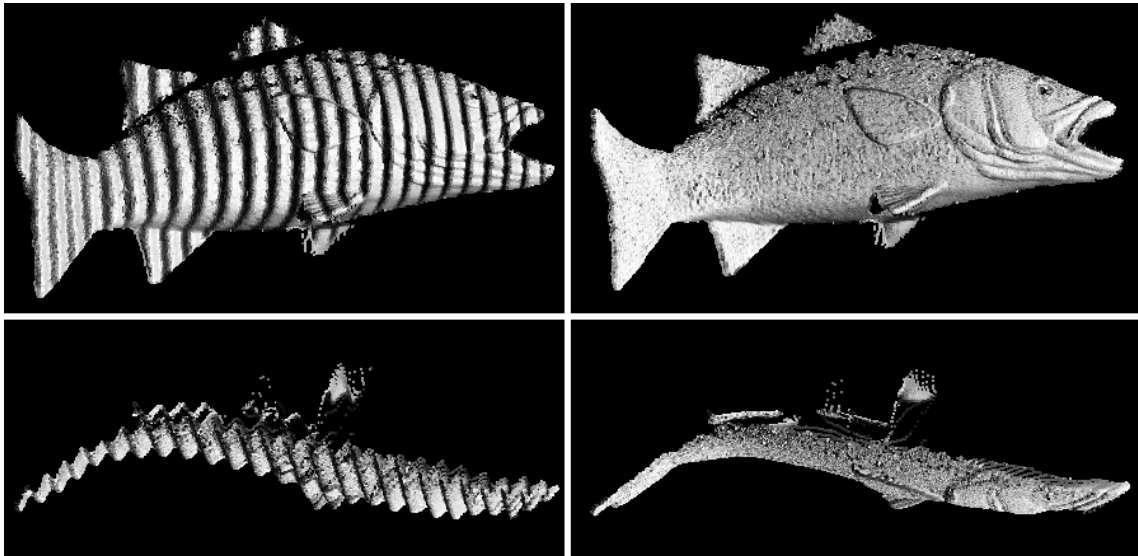


Figure 4.23: The 3-D reconstructions of the textured plastic fish viewed from the front and from above for the (left) uncorrected phase and (right) corrected phase with $N = 4$ constrained gamma and phase optimization.

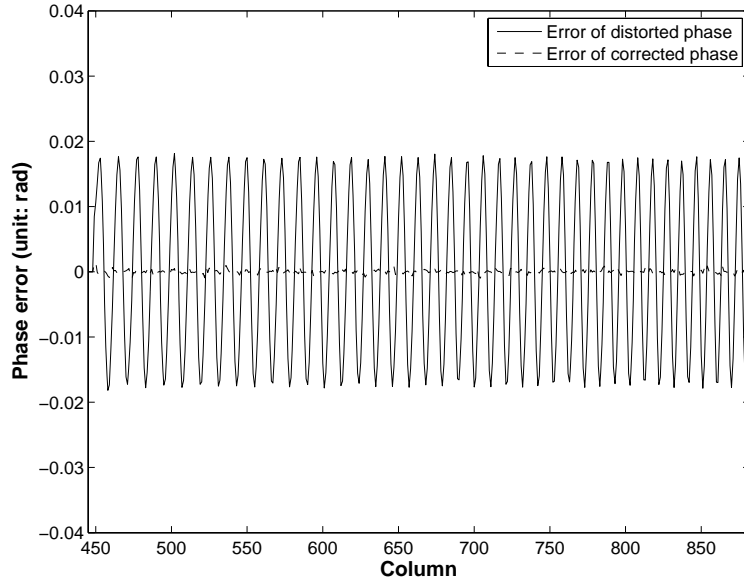


Figure 4.24: Employing a second constraint for $N=5$, the error of gamma distorted phase and corrected phase for $\gamma = 7.73$ of the 512th row of the board.

that RMS of the error of the 512th row of the board, of the corrected phase image, is reduced to 3.4803×10^{-4} for a $43\times$ improvement over the 0.0152 RMS of the error of the uncorrected phase image. The corresponding 3-D points clouds for the foam

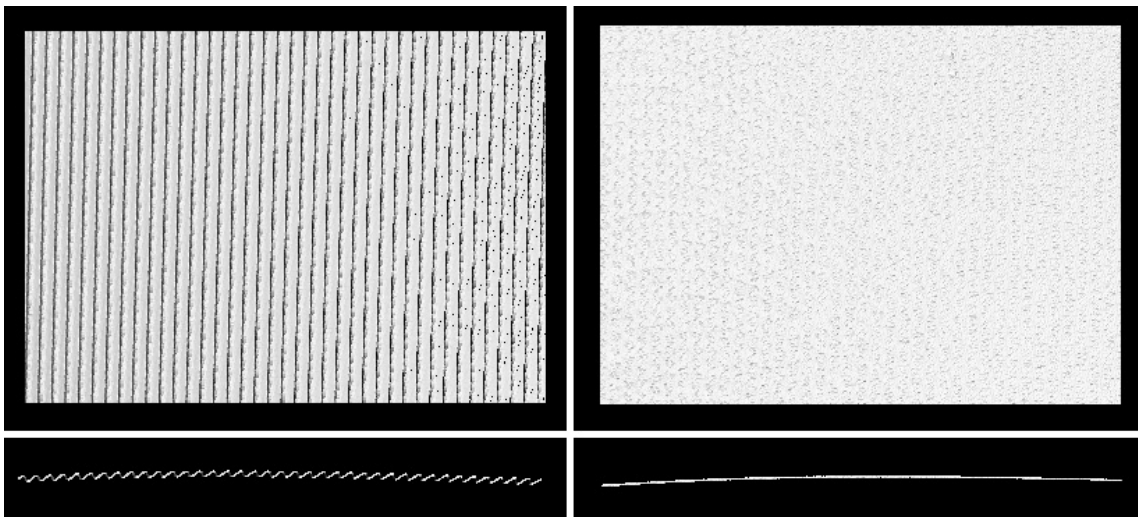


Figure 4.25: The 3-D reconstructions of the textureless foam board viewed from the front and from above for the (left) uncorrected phase and (right) corrected phase with $N = 5$ constrained gamma and phase optimization.

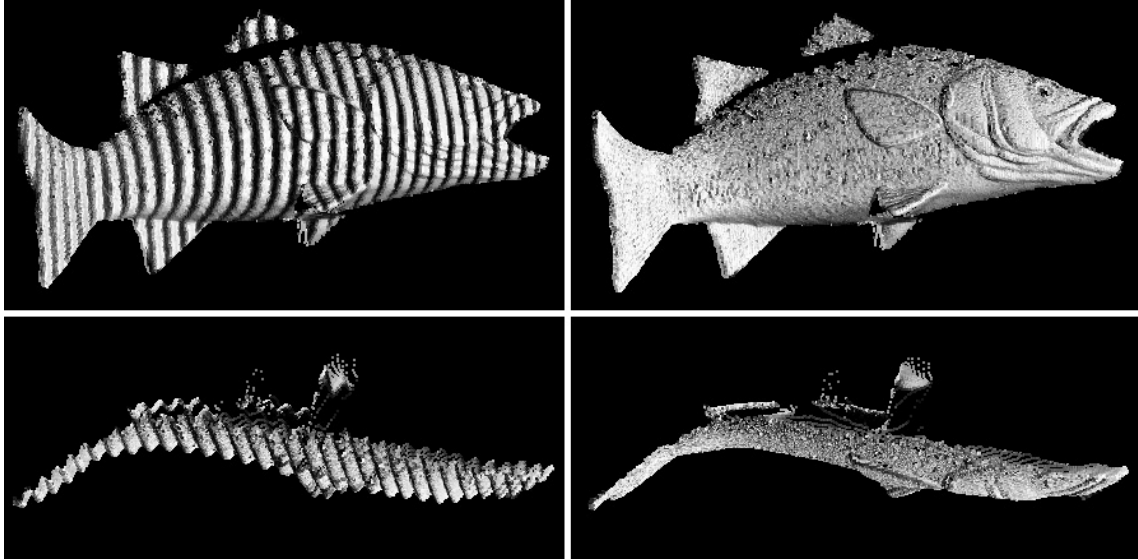


Figure 4.26: The 3-D reconstructions of the textured plastic fish viewed from the front and from above for the (left) uncorrected phase and (right) corrected phase with $N = 5$ constrained gamma and phase optimization.

board are demonstrated in the Fig. 4.22. Figure 4.23 shows similar improvements for the textured fish.

Using $N = 5$ pattern PMP with frequency $f = 8$ and $\gamma = 2.21$, phase error will almost entirely be erased. So for the same reason mentioned above, the gamma is set to 7.73 in software while Eq. (4.61) becomes the constraint on Eq. (4.53). Figure 4.24 shows that RMS of the error of the 512th row of the board, in the corrected phase image, is reduced to 3.1519×10^{-4} for a $39\times$ improvement over the 0.0123 RMS of the error for uncorrected phase. The reconstructed 3-D points clouds for the foam board are illustrated in Fig. 4.25. Figure 4.26 shows the 3-D reconstruction results of the fish.

Chapter 5 Conclusion

As a non-contact, active, triangulation-based 3-D reconstruction technique, SLI is well-known for ease of use and high-accuracy. Numerous SLI pattern coding and decoding strategies are readily available since there is no optimal encoding scheme for all applications. These various pattern strategies can be divided into the two categories of multi-shot and one-shot pattern schemes where, if the scanned object is not moving, then time-multiplexed and stripe-shifted pattern schemes are always the first choice. But in order to scan a moving object, the best methods typically employ one-shot SLI pattern.

As shown in Fig. 1.12, researchers have proposed lots of one-shot SLI pattern strategies in order to achieve real-time 3-D reconstruction. One-shot SLI scheme is insensitive to the motion of object and it is not necessary to make synchronization between the camera and the projector as multi-shot SLI pattern schemes. Except Koninckx et al.'s adaptive pattern scheme [1], the other one-shot patterns are statically coded and never changed in scanning. Some researchers applied the multiplexing techniques of electrical communication theory to SLI pattern design and proposed one-shot schemes such as FTP [53] and CP [32]. Taking advantages of the color features of the camera and projector, i. e., three RGB color channels, some researchers developed color channel multiplexing SLI pattern schemes [58, 59, 60, 61, 62]. Chen et al. [64] proposed sawtooth pattern which was a kind of direct coding method, and scanned object was required with uniform texture. Then there are a large group

of researchers who study one-shot pattern based on spatial neighborhood coding such as non-formal codification [65, 66, 2], De Bruijn Sequences [67, 3, 52], and M-arrays [68, 69, 4].

Because one-shot SLI pattern strategies suffer from low spatial resolution, poor depth accuracy, and high computation cost, various researchers have attempted to scan moving objects with high resolution and accuracy by using multi-shot SLI and driving the camera/projector pair at such high frame rates as to minimize object motion. Zhang and Huang [5] developed a real-time 3-D SLI system which employed fast three-step phase-shifting pattern scheme. That system could capture image at 120 fps and with resolution of 532×500 , generate phase map at 163.93 fps, and reconstruct 3-D point clouds with the phase-to-height representation at 80 fps. Zhang and Yau realized a real-time 3-D SLI scanner with 2+1 pattern strategy [6]. That scanner could capture image at 180 fps and with resolution of 640×480 , and acquired data had to be post-processed mainly for slow phase generation and slow 3-D reconstruction of the absolute 3-D coordinates representation of point clouds. Later Zhang and Yau sped up 3-D reconstruction to 25.56 fps by taking advantage of GPU computation [74].

5.1 Real-Time SLI

In this dissertation, a novel real-time SLI 3-D system has been proposed and implemented with much higher performance both in resolution and speed compared to the system of Zhang and Huang [5]. The key to achieving real-time performance was introducing LUT-based computation in order to eliminate the bottleneck presented

by the arctangent function as well as the matrix inversion operations needed to map phase to 3-D. For the arctangent function, Huang and Zhang [71] implemented a fast three-step phase-shifting algorithm but required phase compensation. Separately, Guo et al. [116] proposed an approximate arctangent algorithm at the cost of accuracy. So in an effort to calculate the arctangent function without sacrificing accuracy, this dissertation analyzed the PMP equations carefully and found that LUTs could be implemented for three special cases of having the number of PMP patterns equal to 3, 4, and 6. Tested by a stand-alone program, the speed of the proposed LUT-based algorithm achieved 1063.83 fps for $N = 3$, 800 fps for $N = 4$, and 456.62 fps for $N = 6$ respectively, while, employing arctangent function directly, the speed of phase generation was 55.65 fps for $N = 3$, 52.91 fps for $N = 4$ and 53.33 for $N = 6$.

With regards to the matrix operations for converting phase to 3-D coordinates, Zhang and Huang [5] employed a phase-to-height method instead generating absolute 3-D coordinates in order to avoid the time-consuming matrix operations, but phase-to-height mapping will not work if the scanned object is out of the range of the reference plane. So Zhang et al. [74] attempted to compute the absolute 3-D coordinates with matrix operations by means of GPU processing, but the improvement was limited. So by expanding the matrix operations including matrix inverse and matrix multiplication carefully, this dissertation rewrote the equations for 3-D reconstruction with some corresponding LUTs built to replace the redundant processing. Tested by a stand-alone program, the LUT-based absolute 3-D coordinates can achieve 228.83 fps, while that speed is only 22.22 fps with matrix operations. As a comparison, the new approach speeds up the computation by 10 times, while the improvement

of Zhang et al. was 6 times even with the assistance of GPU processing. This kind of LUT for 3-D reconstruction is suited for all triangulation-based 3-D measurement techniques including stereo vision.

5.2 Pattern Robustness

Given our approach to real-time SLI to use multiple patterns multiplexed in time, the sensitivity of our system to object motion is reduced by minimizing the number of component patterns, but by doing so, we also increase the sensitivity of our system to noise and distortion. For the issue of additive noise, the proposed solution is to employ high-frequency PMP patterns, but this typically requires phase unwrapping, which increases the processing load for pattern demodulation and, thereby, precludes real-time processing. So in order to preserve our real-time processing, we introduced a low-frequency period cue into the projected pattern set such that pattern demodulation involved extracting two phase terms with one serving as the phase unwrapping parameter and the second serving as a noise-resilient phase term for building our 3-D point cloud. While traditional two-frequency PMP scanning involves at least 6 patterns (3 patterns low and 3 patterns high), this new pattern strategy, called Phase Channel Multiplexing Pattern (PCMP), can involve as few as 3 patterns.

To introduce PCMP, the traditional PMP equations were rewritten with new parameters in order to analyze issues easily. The modulation and DC components of the conventional PMP equation were expressed by object reflectivity, pattern modulation, and intensity of ambient light. Then an additive noise model was made, and the absolute errors of the phase, reflectivity, and intensity of ambient light were derived. The

original equations describing these errors were very complicated and were simplified later. With the simplified equations and the measured values of DC components, a simple noise measurement for the SLI system was also proposed. Harmonic analysis was then utilized to embed a unit-frequency signal into a high-frequency signal where the high-frequency signal suppressed the additive noise efficiently and was used for final 3-D reconstruction. The unit-frequency signal acted as reference information to unwrap the high-frequency signal temporally.

Using only 3 patterns, the DC channel was employed to contain a reference signal where the intensity of the ambient light had to be calibrated. In our experiments, the intensity of the ambient light was a negative value related to the features of the camera. Compared to 3-pattern unit-frequency PMP, the variance of phase error could be reduced by 2.25 times when the high frequency is 3 in the 3-pattern PCMP. Using 4 patterns, the half phase channel was used for embedding a reference signal without ambient light calibration, because the intensity of ambient light canceled out automatically for more than 3 patterns. With the percentage of phase unwrapping successfully larger than 99% and the high frequency set to 6 periods across the projector field of view, the variance of phase error was reduced by more than 7 times compared to 4-pattern unit-frequency PMP. Finally when the number of patterns was 5, the second full-phase channel was stored as a reference signal. The intensity of ambient light was then removed. With the percentage of phase unwrapping successfully larger than 99% and the high frequency set to 6, the variance of phase error was reduced by more than 21 times in the experiments compared to the 5-pattern unit-frequency PMP.

Separate from additive noise, another issue that had to be addressed in this dissertation because of the low pattern number that we employed relates to projector/camera distortion caused by a non-linear response of the optical devices. This gamma distortion issue was addressed previously by modeling the distortion by the power law and expanding by Fourier series to extract a set of higher-order harmonics. So the key to solve this non-linearity was removing the high-order harmonics from the captured gamma-distorted images. However without a detailed expression for the gamma model, it has been difficult to achieve gamma correction. So in this dissertation, a mathematical and detailed gamma model for PMP was proposed such that gamma correction was performed with or without calibration.

With the proposed gamma model, the ratio relationship between any two magnitudes of harmonics was derived such that a novel gamma calibration method was presented according to the ratio relationship. Where traditional gamma calibration typically employed a white board as the target and lots of intensity-varied uniform pattern are projected onto the board, the gamma calibration method proposed in this dissertation computes all the gamma value for valid pixels in the image, and the mean of all the computed gamma values was then chosen as the global gamma. According to our experiments, the histogram of the gamma set was a Gaussian distribution with very small variance. So it was a reliable estimate of the true gamma.

Two categories solutions to correct gamma distortion were also presented in this dissertation. The first involved performing phase correction with gamma calibration so that, once a global gamma value was determined, the distorted phase could be corrected by some kind of numerical method such as by bisection. In our experiments,

the RMS of phase error was reduced 66 times. A second category of phase correction was performed without gamma calibration. This approach involved three separate cases according to number of patterns employed, i. e., $N = 3, 4,$ and 5 . For $N = 3$, the intensity of ambient light had to be calibrated or kept as small as possible, then the information in the DC channel could be employed to correct phase error. For $N = 4$, there was no constraint on the intensity of ambient light. For $N \geq 5$, the second phase was useful for gamma correction, and in our experiments, the RMS of phase error was reduced more than 33 times without gamma calibration.

5.3 Broader Impact

Real-time SLI 3-D reconstruction has studied for numerous applications including fast, non-contact, human-computer interfacing (HCI) for entertainment/control, fast 3-D modeling for compute-aided design, fast 3-D biometrics for security, and so on. While many techniques exist, most can only acquire data in real-time but require non-real-time post-processing. So in practice, the applications for these many techniques limited. Even with the assistance of GPU, the improvement of processing speed is still limited. The proposed LUT-based algorithms, in this dissertation, can achieve the processes of (1) data acquisition, (2) phase generation, (3) 3-D reconstruction, and (4) 3-D display all in real time.

The proposed framework is also not limited to specific pattern strategies and could, for example, be used to implement the real-time pattern strategies of Zhang et al to greatly increase the rate of phase generation over the rates so far reported. Similarly, the 3-D reconstruction LUT-process is well suited to all triangulation-based

3-D measurement techniques including stereo vision and, hence, could play a vital role in those alternate systems. In fact, Yongchang Wang’s proposed period coded phase shifting (PCPS) strategy [120] was demonstrated experimentally in real-time using the LUT-based framework of this dissertation.

Now while introducing our LUT-based framework, we initially only considered unit-frequency PMP patterns where the obtained phase was particular sensitive to noisy, but that does not mean the reconstructed 3-D data was useless. In fact, if a model of the scanned object, such as a moving sphere with some radius, were known, the center of the sphere in the 3-D world coordinates could be measured by a fitting method with statistical theory, and a perfect 3-D reconstructed moving sphere could be shown according to the measured center location and the known radius. This is an application for virtual reality (VR), and if the scanned object were a moving hand with different gestures, the coarse 3-D data could still be helpful for recognition by means of statistical methods or artificial intelligence (AI)/machine learning theory. This is an application for fast HCI. A related research project led by Dr. Hassebrook had been taken involving one-shot CP scheme. That project had been supported by the National Aeronautics and Space Administration (NASA).

Moving beyond unit-frequency PMP, the PCMP scheme was developed in order to achieve more accurate 3-D in real time. In this scheme, a unit-frequency signal, acting as a reference for temporal phase unwrapping, was embedded with a high-frequency signal by taking advantage of different phase channels according to the particular number of patterns, i. e., $N = 3, 4,$ and $5,$ respectively. The proposed PCMP scheme inherited the advantages of temporal phase unwrapping without in-

roducing additional intermediate patterns. And although PCMP's time-multiplexed high-frequency stripe patterns are sensitive to motion, PCMP is still useful in some applications. For instance in human face or fingerprint scanning, scanned subjects may not be able to hold still for very long, so it is necessary to acquire data as accurately and as fast as possible during the time people can hold still.

For the issue of non-linear response in the optical devices, a complete and detailed gamma model was built such that the phenomena of gamma distortion on SLI can be explained theoretically; gamma in an SLI system can be calibrated robustly and easily; and especially phase error caused by gamma can be corrected not only with gamma calibration, but also without gamma calibration according to different number of patterns. The goal of phase correction is to remove the harmonics caused by gamma, while in my PCMP, harmonics are introduced in purpose to embed a reference signal for phase unwrapping. This means a factor can play roles both in disadvantage and advantage according to different applications. I believe the issue of one-parameter gamma distortion in PMP is done with my gamma model and its corresponding analysis. Gamma models for other pattern strategies can be built and analyzed by a similar way.

So in summary, it is the goal of this dissertation to inspire a new generation of SLI algorithms tailored to LUT-based processing such that those algorithms achieve real-time processing using the system framework proposed here. And by introducing a novel pattern scheme that includes a period cue, those new algorithms should follow the lead set here to similarly offer a means of temporal phase unwrapping. And so it is hoped that this dissertation represents a framework for all future, real-time,

multi-pattern SLI methods.

Copyright© Kai Liu, 2010.

Bibliography

- [1] T. P. Koninckx and L. V. Gool, “Real-time range acquisition by adaptive structured light,” *IEEE Transactions on Pattern Analysis and Machine Intelligence* **28**, 432–445 (2006).
- [2] S. Y. Chen, Y. F. Li, and J. Zhang, “Vision processing for realtime 3-d data acquisition based on coded structured light,” *IEEE Transaction on Image Processing* **17**, 167–176 (2008).
- [3] L. Zhang, B. Curless, and S. M. Seitz, “Rapid shape acquisition using color structured light and multi-pass dynamic programming,” in “3D Data Processing Visualization and Transmission, 2002. Proceedings. First International Symposium on,” (2002), pp. 24–36.
- [4] C. Albitar, P. Graebling, and C. Doignon, “Robust structured light coding for 3d reconstruction,” (IEEE Computer Society, Los Alamitos, CA, USA, 2007), vol. 0, pp. 1–6.
- [5] S. Zhang and P. S. Huang, “High-resolution, real-time three-dimensional shape measurement,” *Optical Engineering* **45**, 123601 (2006).
- [6] S. Zhang and S.-T. Yau, “High-speed three-dimensional shape measurement system using a modified two-plus-one phase-shifting algorithm,” *Optical Engineering* **46**, 113603 (2007).

- [7] C. Rathjen, “Statistical properties of phase-shift algorithms,” *Journal of the Optical Society of America A* **12**, 1997–2008 (1995).
- [8] H. Gudbjartsson and S. Patz, “The rician distribution of noisy mri data,” *Magnetic Resonance in Medicine* **34**, 910–914 (1995).
- [9] J. Li, L. G. Hassebrook, and C. Guan, “Optimized two-frequency phase-measuring-profilometry light-sensor temporal-noise sensitivity,” *Journal of the Optical Society of America A* **20**, 106–115 (2003).
- [10] S. Nakadate and H. Saito, “Fringe scanning speckle-pattern interferometry,” *Applied Optics* **24**, 2172–2180.
- [11] D. C. Ghiglia, G. A. Mastin, and L. A. Romero, “Cellular-automata method for phase unwrapping,” *Journal of the Optical Society of America A* **4**, 267–280.
- [12] J. M. Huntley, “Noise-immune phase unwrapping algorithm,” *Applied Optics* **28**, 3268–3270.
- [13] C. W. Chen and H. A. Zebker, “Network approaches to two-dimensional phase unwrapping: intractability and two new algorithms,” *Journal of the Optical Society of America A* **17**, 401–414 (2000).
- [14] J. M. N. Leitao and M. A. T. Figueiredo, “Absolute phase image reconstruction: a stochastic nonlinear filtering approach,” *IEEE Transactions on Image Processing* **7**, 868–882 (1998).

- [15] B. Friedlander and J. M. Francos, “Model based phase unwrapping of 2-d signals,” *IEEE Transactions on Signal Processing* **44**, 2999–3007 (1996).
- [16] Y. Sirel, *Fringe Analysis* (Springer Berlin / Heidelberg, 1998), vol. 77/2000 of *Topics in Applied Physics*, pp. 55–102.
- [17] M. Takeda, Q. Gu, M. Kinoshita, H. Takai, and Y. Takahashi, “Frequency-multiplex fourier-transform profilometry: a single-shot three-dimensional shape measurement of objects with large height discontinuities and/or surface isolations,” *Applied Optics* **36**, 5347–5354 (1997).
- [18] E.-H. Kim, J. Hahn, H. Kim, and B. Lee, “Profilometry without phase unwrapping using multi-frequency and four-step phase-shift sinusoidal fringe projection,” *Optics Express* **17**, 7818–7830 (2009).
- [19] P. S. Huang, C. Zhang, and F. Chiang, “High-speed 3-d shape measurement based on digital fringe projection,” *Optical Engineering* **42**, 163–168 (2003).
- [20] M. J. Baker, J. Xi, and J. F. Chicharo, “Elimination of γ non-linear luminance effects for digital video projection phase measuring profilometers,” in “4th IEEE International Symposium on Electronic Design, Test and Applications,” , vol. 0 (IEEE Computer Society, Los Alamitos, CA, USA, 2008), vol. 0, pp. 496–501.
- [21] P. S. Huang, Q. J. Hu, and F. Chiang, “Double three-step phase-shifting algorithm,” *Applied Optics* **41**, 4503–4509 (2002).
- [22] Y. Hu, J. Xi, J. F. Chicharo, and Z. Yang, “Improved three-step phase shifting profilometry using digital fringe pattern projection,” in “International Con-

- ference on Computer Graphics, Imaging and Visualization,” , vol. 0 (IEEE Computer Society, Los Alamitos, CA, USA, 2006), vol. 0, pp. 161–167.
- [23] Y. Hu, J. Xi, E. Li, J. Chicharo, and Z. Yang, “Three-dimensional profilometry based on shift estimation of projected fringe patterns,” *Applied Optics* **45**, 678–687 (2006).
- [24] M. J. Baker, J. Xi, and J. F. Chicharo, “Neural network digital fringe calibration technique for structured light profilometers,” *Applied Optics* **46**, 1233–1243 (2007).
- [25] S. Zhang and P. S. Huang, “Phase error compensation for a 3-d shape measurement system based on the phase-shifting method,” *Optical Engineering* **46**, 063601:1–9 (2007).
- [26] S. Zhang and S. Yau, “Generic nonsinusoidal phase error correction for three-dimensional shape measurement using a digital video projector,” *Applied Optics* **46**, 36–43 (2007).
- [27] H. Guo, H. He, and M. Chen, “Gamma correction for digital fringe projection profilometry,” *Applied Optics* **43**, 2906–2914 (2004).
- [28] B. Pan, L. H. Q. Kema, and A. Asundi, “Phase error analysis and compensation for nonsinusoidal waveforms in phase-shifting digital fringe projection profilometry,” *Optics Letters* **34**, 416–418 (2009).

- [29] K. Liu, Y. Wang, D. L. Lau, Q. Hao, and L. G. Hassebrook, “Dual-frequency pattern scheme for high-speed 3-d shape measurement,” *Optics Express* **18**, 5229–5244 (2010).
- [30] B. Curless and S. Seitz, “3d photography,” *ACM Siggraph '00 Course Notes*, Course No. 19 (2000).
- [31] S. Zhang, D. Royer, and S.-T. Yau, “High-resolution, real-time-geometry video acquisition system,” in “SIGGRAPH '06: ACM SIGGRAPH 2006 Emerging technologies,” (ACM, New York, NY, USA, 2006), p. 14.
- [32] C. Guan, L. G. Hassebrook, and D. L. Lau, “Composite structured light pattern for three-dimensional video,” *Optics Express* **11**, 406–417 (2003).
- [33] Y. Wang, K. Liu, Q. Hao, D. Lau, and L. G. Hassebrook, “Multicamera phase measuring profilometry for accurate depth measurement,” in “Sensors and Systems for Space Applications,” , vol. 6555 of *Society of Photo-Optical Instrumentation Engineers (SPIE) Conference Series*, R. T. Howard and R. D. Richards, eds. (International Society for Optical Engineering; 1999, 2007), vol. 6555 of *Society of Photo-Optical Instrumentation Engineers (SPIE) Conference Series*, pp. 1–12.
- [34] Y. Wang, Q. Hao, A. Fatehpuria, D. L. Lau, and L. G. Hassebrook, “Data acquisition and quality analysis of 3-dimensional fingerprints,” in “IEEE conference on Biometrics, Identity and Security, Tampa, Florida,” (2009).

- [35] J. Salvi, J. Pages, and J. Batlle, "Pattern codification strategies in structured light systems," *Pattern Recognition* **37**, 827–849 (2004).
- [36] F. Blais, "A review of 20 years of range sensor development," *Videometrics VII, Proceedings of SPIE-IS&T Electronic Imaging* **5013**, 62–76 (2003).
- [37] F. Chen, G. M. Brown, and M. Song, "Overview of three-dimensional shape measurement using optical methods," *Optical Engineering* **39**, 10–22 (2000).
- [38] P. J. Besl, "Active, optical range imaging sensors," *Machine Vision and Applications* **1**, 127–152 (1988).
- [39] R. A. Jarvis, "A perspective on range finding techniques for computer vision," *IEEE Transactions on Pattern Analysis and Machine Intelligence* **5**, 122–139 (1983).
- [40] J. Batlle, E. Mouaddib, and J. Salvi, "Recent progress in coded structured light as a technique to solve the correspondence problem: a survey," *Pattern Recognition* **31**, 963–982 (1998).
- [41] G. S. of Schmaltz Brothers Laboratories, "A method for presenting the profile curves of rough surfaces," *Naturwiss* **18**, 315–316 (1932).
- [42] C. Guan, L. G. Hassebrook, D. L. Lau, V. G. Yalla, and C. J. Casey, "Improved composite-pattern structured-light profilometry by means of postprocessing," *Optical Engineering* **47**, 097203 (2008).

- [43] P. Axelsson, "Processing of laser scanner data—algorithms and applications," *ISPRS Journal of Photogrammetry and Remote Sensing* **54**, 138–147 (1999).
- [44] M. J. Milroy, D. J. Weir, C. Bradley, and G. W. Vickers, "Reverse engineering employing a 3d laser scanner: A case study," *The International Journal of Advanced Manufacturing Technology* **12**, 111–121 (1996).
- [45] M. Halioua and H. Liu, "Optical three-dimensional sensing by phase measuring profilometry," *Optics and Lasers in Engineering* **11**, 185–215 (1989).
- [46] V. Srinivasan, H. C. Liu, and M. Halioua, "Automated phase-measuring profilometry: a phase mapping approach," *Applied Optics* **24**, 185–188 (1985).
- [47] V. Srinivasan, H. C. Liu, and M. Halioua, "Automated phase-measuring profilometry of 3-d diffuse objects," *Applied Optics* **23**, 3105–3108 (1984).
- [48] X. Su, W. Zhou, G. von Baly, and D. Vukicevic, "Automated phase-measuring profilometry using defocused projection of a ronchi grating," *Optics Communications* **94**, 561–573 (1992).
- [49] X. Su, G. von Bally, and D. Vukicevic, "Phase-stepping grating profilometry: utilization of intensity modulation analysis in complex objects evaluation," *Optics Communications* **98**, 141–150 (1993).
- [50] V. G. Yalla and L. G. Hassebrook, "Very high resolution 3d surface scanning using multi-frequency phase measuring profilometry," (SPIE, 2005), vol. 5798, pp. 44–53.

- [51] S. Zhang and P. S. Huang, “Novel method for structured light system calibration,” *Optical Engineering* **45**, 083601 (2006).
- [52] J. Pagès, J. Salvi, C. Collewet, and J. Forest, “Optimised De Bruijn patterns for one-shot shape acquisition,” *Optics & Laser Technology* **23**, 707–720 (2005).
- [53] M. Takeda and K. Mutoh, “Fourier transform profilometry for the automatic measurement of 3-d object shapes,” *Applied Optics* **22**, 3977–3982 (1983).
- [54] W. Chen, X. Su, Y. Cao, L. Xiang, and Q. Zhang, “Fourier transform profilometry based on a fringe pattern with two frequency components,” *Optik – International Journal for Light and Electron Optics* **119**, 57–62 (2006).
- [55] X. Su and W. Chen, “Fourier transform profilometry: a review,” *Optics and Lasers in Engineering* **35**, 263–284 (2001).
- [56] C. Guan, L. G. Hassebrook, D. L. Lau, and V. Yalla, “Near-infrared composite pattern projection for continuous motion hand-computer interaction,” *Journal of Visual Communication and Image Representation* **18**, 141–150 (2007).
- [57] H.-M. Yue, X.-Y. Su, and Y.-Z. Liu, “Fourier transform profilometry based on composite structured light pattern,” *Optics & Laser Technology* **39**, 1170–1175 (2007).
- [58] C. Wust and D. W. Capson, “Surface profile measurement using color fringe projection,” *Machine Vision and Applications* **4**, 193–203 (1991).

- [59] Z. J. Geng, “Rainbow 3–dimensional camera: new concept of high-speed 3–dimensional vision systems,” *Optical Engineering* **35**, 376–383 (1996).
- [60] P. S. Huang, Q. Hu, F. Jin, and F.-P. Chiang, “Color–encoded digital fringe projection technique for high–speed three–dimensional surface contouring,” *Optical Engineering* **38**, 1065–1071 (1999).
- [61] J. Pan, P. S. Huang, and F.-P. Chiang, “Color phase–shifting technique for three–dimensional shape measurement,” *Optical Engineering* **45**, 013602 (2006).
- [62] N. Mandava, “Color multiplexed single pattern SLI,” Master’s thesis, University of Kentucky, USA (2008).
- [63] W.-H. Su, “Color–encoded fringe projection for 3d shape measurements,” *Optics Express* **15**, 13167–13181 (2007).
- [64] L. Chen, C. Quan, C. J. Tay, and Y. Fu, “Shape measurement using one frame projected sawtooth fringe pattern,” *Optics Communications* **246**, 275–284 (2005).
- [65] K. L. Boyer and A. C. Kak, “Color-encoded structured light for rapid active ranging,” *IEEE Transactions on Pattern Analysis and Machine Intelligence* **9**, 14–28 (1987).
- [66] M. Maruyama and S. Abe, “Range sensing by projecting multiple slits with random cuts,” *IEEE Transactions on Pattern Analysis and Machine Intelligence* **15**, 1647–651 (1993).

- [67] P. Vuytsteke and A. Oosterlinck, “Range image acquisition with a single binary-encoded light pattern,” *IEEE Transactions on Pattern Analysis and Machine Intelligence* **12**, 148–163 (1990).
- [68] H. J. W. Spoelder, F. M. Vos, E. M. Petriu, and F. C. A. Groen, “Some aspects of pseudo random binary array-based surface characterization,” *IEEE Transactions on Instrumentation and Measurement* **49**, 1331–1336 (2000).
- [69] Y. C. Hsieh, “Decoding structured light patterns for three-dimensional imaging systems,” *Pattern Recognition* **34**, 343–349 (2001).
- [70] H. Fredricksen, “A survey of full length nonlinear shift register cycle algorithms,” *SIAM Review* **24**, 195–221 (1982).
- [71] P. S. Huang and S. Zhang, “Fast three-step phase-shifting algorithm,” *Applied Optics* **45**, 5086–5091 (2006).
- [72] C. Zhang, P. S. Huang, and F.-P. Chiang, “Microscopic phase-shifting profilometry based on digital micromirror device technology,” *Applied Optics* **41**, 5896–5904 (2002).
- [73] P. L. Wizinowich, “Phase shifting interferometry in the presence of vibration: A new algorithm and system,” *Applied Optics* **29**, 3271–3279 (1990).
- [74] S. Zhang, D. Royer, and S.-T. Yau, “GPU-assisted high-resolution, real-time 3-d shape measurement,” *Optics Express* **14**, 9120–9129 (2006).

- [75] S. Kogan, *Electronic Noise and Fluctuations in Solids* (Cambridge University Press, 1996).
- [76] A. Patil, R. Langoju, P. Rastogi, and S. Ramani, “Statistical study and experimental verification of high-resolution methods in phase-shifting interferometry,” *Journal of the Optical Society of America A* **24**, 794–813 (2007).
- [77] G. Nico, “Noise-residue filtering of interferometric phase images,” *Journal of the Optical Society of America A* **17**, 1962–1974 (2000).
- [78] M. Servin, J. C. Estrada, J. A. Quiroga, J. F. Mosino, and M. Cywiak, “Noise in phase shifting interferometry,” *Optics Express* **17**, 8789–8794 (2009).
- [79] Y. Surrel, “Additive noise effect in digital phase detection,” *Applied Optics* **36**, 271–276 (1997).
- [80] Y. Surrel, “Design of algorithms for phase measurements by the use of phase stepping,” *Applied Optics* **35**, 51–60 (1996).
- [81] T. R. Judge and P. J. Bryanston-Cross, “A review of phase unwrapping techniques in fringe analysis,” *Optics and Lasers in Engineering* **21**, 199–239 (1994).
- [82] O. Marklund, “An anisotropic evolution formulation applied in 2-d unwrapping of discontinuous phase surfaces,” *IEEE Transactions on Image Processing* **10**, 1700–1711.
- [83] L. Graham, “Synthetic interferometer radar for topographic mapping,” *Proceedings of the IEEE* **62**, 763–768.

- [84] L. Cutrona, “Comparison of sonar system performance achievable using synthetic aperture techniques with the performance achievable by more conventional means,” *Journal of the Acoustical Society of America* **58**, 336–348.
- [85] M. Hedley and D. Rosenfeld, “A new two-dimensional phase unwrapping algorithm for mri images,” *Magnetic Resonance in Medicine* **24**, 177–181.
- [86] S. M. Pandit, N. Jordache, and G. A. Joshi, “Data-dependent systems methodology for noise-insensitive phase unwrapping in laser interferometric surface characterization,” *Journal of the Optical Society of America A* **11**, 2584–2592.
- [87] J. M. Bioucas-Dias and G. Valadao, “Phase unwrapping via graph cuts,” *IEEE Transactions on Image Processing* **16**, 698–709.
- [88] J. M. Huntley and H. O. Saldner, “Error-reduction methods for shape measurement by temporal phase unwrapping,” *Journal of the Optical Society of America A* **14**, 3188–3196 (1997).
- [89] S. Li, W. Chen, and X. Su, “Reliability-guided phase unwrapping in wavelet-transform profilometry,” *Applied Optics* **47**, 3369–3377 (2008).
- [90] S. Zhang, X. Li, and S.-T. Yau, “Multilevel quality-guided phase unwrapping algorithm for real-time three-dimensional shape reconstruction,” *Applied Optics* **46**, 50–57 (2007).
- [91] Y. Shi, “Robust phase unwrapping by spinning iteration,” *Optics Express* **15**, 8059–8064 (2007).

- [92] M. Costantini, “A novel phase unwrapping method based on network programming,” *IEEE Transactions on Geoscience and Remote Sensing* **36**, 813–821 (1998).
- [93] D. S. Mehta, S. K. Dubey, M. M. Hossain, and C. Shakher, “Simple multifrequency and phase-shifting fringe-projection system based on two-wavelength lateral shearing interferometry for three-dimensional profilometry,” *Applied Optics* **44**, 7515–7521 (2005).
- [94] G. Pedrini, I. Alexeenko, W. Osten, and H. J. Tiziani, “Temporal phase unwrapping of digital hologram sequences,” *Applied Optics* **42**, 5846–5854 (2003).
- [95] D. J. Bone, “Fourier fringe analysis: the two-dimensional phase unwrapping problem,” *Applied Optics* **30**, 3627–3632.
- [96] J. J. Gierloff, “Phase unwrapping by regions,” in “Society of Photo-Optical Instrumentation Engineers (SPIE) Conference Series,” , vol. 818 of *Society of Photo-Optical Instrumentation Engineers (SPIE) Conference Series*, R. E. Fischer and W. J. Smith, eds. (1987), vol. 818 of *Society of Photo-Optical Instrumentation Engineers (SPIE) Conference Series*, pp. 2–9.
- [97] J. T. Judge, C. Quan, and P. J. Bryanston-Cross, “Holographic deformation measurements by fourier transform technique with automatic phase unwrapping,” *Optical Engineering* **31**, 533–543 (1992).

- [98] J. M. B. Dias and J. M. N. Leitaó, “The $Z\pi M$ algorithm: a method for interferometric image reconstruction in SAR/SAS,” *IEEE Transactions on Image Processing* **11**, 408–422 (2002).
- [99] D. L. Fried, “Least-square fitting a wave-front distortion estimate to an array of phase-difference measurements,” *Journal of the Optical Society of America* **67**, 370–375 (1977).
- [100] T. J. Flynn, “Two-dimensional phase unwrapping with minimum weighted discontinuity,” *Journal of the Optical Society of America A* **14**, 2692–2701 (1997).
- [101] C. W. Chen, “Statistical-cost network-flow approaches to two-dimensional phase unwrapping for radar interferometry,” Ph.D. thesis, Stanford University (2001).
- [102] R. J. Green and J. G. Walker, “Phase unwrapping using a priori knowledge about the band limits of a function,” in “Society of Photo-Optical Instrumentation Engineers (SPIE) Conference Series,” , vol. 1010 of *Society of Photo-Optical Instrumentation Engineers (SPIE) Conference Series*, D. W. Braggins, ed. (1989), vol. 1010 of *Society of Photo-Optical Instrumentation Engineers (SPIE) Conference Series*, pp. 36–43.
- [103] J. M. B. Dias and J. M. N. Leitaó, “Simultaneous phase unwrapping and speckle smoothing in SAR images - a stochastic nonlinear filtering approach,” in “EUSAR ’98 - European Conference on Synthetic Aperture Radar,”

- (Friedrichshafen, Germany, 1998), EUSAR '98 - European Conference on Synthetic Aperture Radar, pp. 373–377.
- [104] J. M. Huntley and H. O. Saldner, “Temporal phase-unwrapping algorithm for interferogram analysis,” *Applied Optics* **32**, 3047–3052 (1993).
- [105] J.-L. Li, H.-J. Su, and X.-Y. Su, “Two-frequency grating used in phase-measuring profilometry,” *Applied Optics* **36**, 277–280 (1997).
- [106] C. A. Poynton, ““gamma” and its disguises: The nonlinear mappings of intensity in perception, crts, film and video,” *SMPTE* pp. 1099–1108 (2001).
- [107] H. Farid, “Blind inverse gamma correction,” *IEEE Transactions on Image Processing* **10**, 1428–1433 (2001).
- [108] A. Siebert, “Retrieval of gamma corrected images,” *Pattern Recognition Letters* **22**, 249–256 (2001).
- [109] K. Hibino, B. F. Oreb, D. I. Farrant, and K. G. Larkin, “Phase shifting for nonsinusoidal waveforms with phase-shift errors,” *Optical Engineering* **12**, 761–768 (1995).
- [110] Y. Sirel, “Design of algorithms for phase measurements by the use of phase stepping,” *Applied Optics* **35**, 51–60 (1996).
- [111] P. Jia, J. Kofman, and C. English, “Intensity-ratio error compensation for triangular-pattern phase-shifting profilometry,” *Journal of the Optical Society of America A* **24**, 3150–3158 (2007).

- [112] S. F. Frisken, S. F. Frisken, R. N. Perry, R. N. Perry, A. P. Rockwood, A. P. Rockwood, T. R. Jones, and T. R. Jones, “Adaptively sampled distance fields: A general representation of shape for computer graphics,” (2000), pp. 249–254.
- [113] M. Lucente, “Interactive computation of holograms using a look-up table,” *Journal of Electronic Imaging* **2**, 28–34 (1993).
- [114] R. Ishiyama, S. Sakamoto, J. Tajima, T. Okatani, and K. Deguchi, “Absolute phase measurements using geometric constraints between multiple cameras and projectors,” *Applied Optics* **46**, 3528–3538.
- [115] K. Liu, Y. Wang, D. L. Lau, Q. Hao, and L. G. Hassebrook, “Gamma model and its analysis for phase measuring profilometry,” *Journal of the Optical Society of America A* **27**, 553–562 (2010).
- [116] H. Guo and G. Liu, “Approximations for the arctangent function in efficient fringe pattern analysis,” *Optics Express* **15**, 3053–3066 (2007).
- [117] J. Schwider, R. Burow, K.-E. Elssner, J. Grzanna, R. Spolaczyk, and K. Merkel, “Digital wave-front measuring interferometry: some systematic error sources,” *Applied Optics* **22**, 3421–3432 (1983).
- [118] K. A. Stetson and W. R. Brohinsky, “Electrooptic holography and its application to hologram interferometry,” *Applied Optics* **24**, 3631–3637 (1985).
- [119] D. Scharstein and R. Szeliski, “High-accuracy stereo depth maps using structured light,” in “CVPR 2003,” , vol. 1 (IEEE Computer Society, 2003), vol. 1, pp. 195–202.

- [120] Y. Wang, K. Liu, Q. Hao, D. L. Lau, and L. G. Hassebrook, "Period coded phase shifting strategy for 3-D real-time acquisition and data processing," (2009).

VITA

Kai Liu

- Birth Date: 8th May 1973
- Birth Place: China

Education

- **Master of Science**, “Design and Implement of Computer Network Management System Based on SNMP”, Department of Computer Science, Sichuan University, China.
- **Bachelor of Science**, “Design and Implementing Numerical Solution of Equivalent Difference Latitude Parallel Polyconic Projection for World Map in Computer”, Department of Computer Science, Sichuan University, China.

Professional activities

- Reviewer of the Optical Society of America (OSA), 2010
- Research Assistant, University of Kentucky, USA. 2005-2010.
- Lecturer, Sichuan University, China. 2001-2005.
- Research Assistant, Sichuan University, China. 1998-2001.
- Computer administrator, Jiangsu Commercial Bank, China. 1996-1998.

Invention disclosures

1. **Kai Liu**, Yongchang Wang, Daniel L. Lau and Laurence G. Hassebrook, “Dual-frequency Phase Multiplexing and Period Coded Phase Measuring pattern strategies in 3-D structured light systems, and Lookup Table based real-time data processing for phase measuring pattern strategies, ” submitted 10-9-2009. Approved for provisional patent application. (INV09/1686).
2. Yongchang Wang, **Kai Liu**, Daniel L. Lau and Laurence G. Hassebrook, “A Maximum SNR Pattern Strategy for Phase Shifting Methods in Structured Light Illumination and Gamma model and its analysis for Phase Measuring Profilometry,” submitted 12-26-2009. Approved for provisional patent application. (INV09/1710).
3. Yongchang Wang, Daniel L. Lau, Laurence G. Hassebrook and **Kai Liu**, “Multi-Camera Phase Measuring Profilometry for Accurate Registration and Distortion-Free Fingerprint Unraveling to Aimed Definition”. (INV09/1667)
4. Laurence G. Hassebrook, Charles J. Casey, Eli R. Crane, Walter F. Lundby, Yongchang Wang and **Kai Liu**, “Rotate and Hold and Scan Structured Light Illumination Pattern Encoding and Decoding,” Approved for provisional patent application by University of Kentucky (INV09/1706)

Publications

Journal papers

1. Daniel L. Lau, **Kai Liu** and Laurence G. Hassebrook, “Real-Time Three-Dimensional Shape Measurement of Moving Objects without Edge Errors by Time Synchronized Structured Illumination,” *Optics Letter* 35, 2487-2489 (2010)
2. Yongchang Wang, **Kai Liu**, Qi Hao, Daniel L. Lau and Laurence G. Hassebrook, “Maximum SNR Pattern Strategy in Phase Shifting Methods,” Accepted by *Journal of the Optical Society of America, A.*, 2010.
3. **Kai Liu**, Yongchang Wang, Daniel L. Lau, Qi Hao and Laurence G. Hassebrook, “Gamma Model and its Analysis for Phase Measuring Profilometry,” *Journal of the Optical Society of America, A* 27, 553–562 (2010).
4. **Kai Liu**, Yongchang Wang, Daniel L. Lau, Qi Hao and Laurence G. Hassebrook, “Dual-frequency pattern scheme for high-speed 3-D shape measurement,” *Optics Express* 18, 5229-5244 (2010).
5. **Kai Liu**, Yongchang Wang, Daniel L. Lau, Qi Hao and Laurence G. Hassebrook, “Phase channel multiplexing pattern strategy for structured light illumination,” In preparation for *IEEE Transactions on Image Processing*, 2010.
6. Yongchang Wang, **Kai Liu**, Qi Hao, Daniel L. Lau and Laurence G. Hassebrook, “Period Coded Phase Shifting Strategy for 3-D Real-time Acquisition and Data Processing” Submitted to *IEEE Transactions on Image Processing*, 2009.

7. Yongchang Wang, **Kai Liu**, Qi Hao, Daniel L. Lau and Laurence G. Hassebrook, “Hybrid Structured Light Illumination and Stereo Vision 3-D Reconstruction” Submitted to IEEE Transactions on Pattern Analysis and Machine Intelligence, 2009.
8. **Kai Liu**, Chunxu Liu and Hongwei Zhang, “Analysis and Design of the Interface System for Bank Payment System,” (in Chinese) Journal of Sichuan University (Engineering and Science Edition), 33(6), 101–104 (2001).
9. **Kai Liu** and Chunxu Liu “Programming for the Unix Network Server,” (in Chinese), Computer and Information Technology, 91(4), 26–30 (2001).

Conference papers

1. Yongchang Wang, **Kai Liu**, Qi Hao, Daniel L. Lau, and Laurence G. Hassebrook, “Multicamera Phase Measuring Profilometry For Accurate Depth Measurement,” Proceedings of SPIE, the International Society for Optical Engineering, Orlando, Florida, Vol. 6555, Apr. 9–15, 2007.
2. Chunxu Liu and **Kai Liu**, “Character User Interface Design for Unix,” (in Chinese), in The Development of the Libraries in 21 Century and the Applications of Modern Education Technology, edited by Fangjian Liu et al, Chengdu: The Press of Southwestern University of Finance and Economics, 383-389 (2001).

Others

1. **Kai Liu**, Yongchang Wang, Daniel L. Lau, Qi Hao and Laurence G. Hassebrook, “Towards gesture-controlled computers with real-time structured light,” SPIE Newsroom. DOI: 10.1117/2.1201005.002941, May. 2010.

Presentations

1. **Kai Liu**, “Real-time 3-D reconstruction by means of structured light illumination,” Department of Electrical and Computer Engineering, University of Delaware, USA, May 22, 2010.
2. Daniel L. Lau, **Kai Liu** and Laurence G. Hassebrook, “Active and passive range sensor fusion for automated surveillance and face recognition: video camera array for face surveillance involving stereo vision technology,” Department of Homeland Security, Washington DC, USA, Nov., 2007.
3. Daniel L. Lau, **Kai Liu** and Laurence G. Hassebrook, “Active and passive range sensor fusion for automated surveillance and face recognition: face detecting and scanning surveillance network using laser beam,” Department of Homeland Security, Washington DC, USA, Mar., 2007.
4. **Kai Liu**, “Design and Implement of Computer Network Management System Based on SNMP,” Defence of Master Degree, Sichuan University, China, June, 2001.

5. **Kai Liu**, “Design and Implementing Numerical Solution of Equivalent Difference Latitude Parallel Polyconic Projection for World Map in Computer,” Defence of Bachelor Degree, Sichuan University, China, June, 1996.

Media news

1. “Real-Time 3D Structured Light System”, YouTube video, Oct., 2009.
2. “Real-time 3-D SLI system”, Prosilica Camera News, Sept. 2009.